Conductivity and Electrochemistry of Hierarchically Structured Layered Oxides and Electrodes for Na-Ion Batteries

Zur Erlangung des akademischen Grades eines

Doktors der Ingenieurwissenschaften (Dr.-Ing.)

von der KIT-Fakultät für Maschinenbau
des Karlsruher Instituts für Technologie (KIT)

genehmigte
Dissertation

von

M. Sc. Marius Schmidt

Contents

I Acknowledgements

Many people contributed to the success of this work. Special thanks go to:

II Affirmation in lieu of oath

I declare that I completed this thesis independently and used only the materials that are listed. All used content, whether quoted directly or paraphrased, from both published and unpublished sources, is properly cited.

The statutes for safeguarding good research practice at Karlsruhe Institute of Technology (KIT) were respected.

Karlsruhe, February 15, 2024

Marius Schmidt

III List of figures

IV List of tables

V List of abbreviations

AV	Average voltage
BET	Brunauer-Emmett-Teller
CAM	Cathode active material
Chap.	Chapter
DFT	Density functional theory
DMC	Dimethylcarbonate
DRT	Distribution of relaxation times
DSC	Differential scanning calorimetry
E_{A_e}	Activation energy for the electronic transport process
E_{A_i}	Activation energy for the ionic transport process
ECW	Electrochemical window
EIS	Electrochemical impedance spectroscopy
F	Faraday constant
FEC	Fluoroethylene carbonate
Fig.	Figure
ICP-OES	Inductive coupled plasma optical emission spectroscopy
IS	isomeric shift
LFP	Lithium-iron-phosphate
LIB	Lithium-ion-battery
Na_1	sodium site 1, equivalent to Na_f
Na_2	sodium site 2, equivalent to Na_e
NAFMO	$Na_{0.6}Al_{0.11}Fe_{0.22}Mn_{0.66}O_2$
NANMFO	$Na_{0.6}Al_{0.11}Ni_{0.11}Fe_{0.11}Mn_{0.66}O_2$
NANMO	$Na_{0.6}Al_{0.11}Ni_{0.22}Mn_{0.66}O_2$
NCA	Nickel-Cobalt-Aluminium-Oxide
NMC	Nickel-Manganese-Cobalt-Oxide
NMFO	$Na_{0.6}Fe_{1/3}Mn_{2/3}O_2$
NMP	N-Methyl-2-pyrrolidon
OCV	Open circuit voltage
Φ	Porosity
PC	Propylene carbonate
PP	Primary particle
Q_{spec}	Specific capacity
QS	Quadrupole splitting
Q_{theo}	Theoretical capacity
SEM	Scanning electron microscopy
SIB	Sodium-ion-battery
SP	Secondary particle
Tab.	Table
TGA	Thermogravimetric analysis
T_s	Sinter temperature

UL	Upper limit
W	Energy density
XRD	X-ray diffraction

VI Zusammenfassung

Die vorliegende Arbeit befasst sich mit der Synthese und Charakterisierung von Kathodenmaterial für Natrium-Ionen-Batterien. Diese haben das Potential, in einigen Anwendungen eine Alternative zu kommerziellen Lithium-Ionen-Batterien zu werden, insbesondere da zu erwarten ist, dass der Bedarf an Energiespeichern in den kommenden Jahrzehnten steigen wird [1–3]. Als Materialklasse wurden die Schichtoxide $Na_{0.6}MO_2$ (M steht für ein bestimmtes Verhältnis der Metalle Al, Ni, Fe und Mn) gewählt und vier verschiedene chemische Zusammensetzungen getestet . Dazu wurde der Nickelanteil schrittweise reduziert und durch Eisen ersetzt (siehe Kapitel 3).

Für die Herstellung wurde das Sprühtrocknen gewählt, da sich damit eine sogenannte hierarchische Strukturierung erzeugen lässt und mit dieser Methode auch größere Mengen an Kathodenmaterial hergestellt werden können [4]. Die hierarchische Strukturierung entsteht, wenn feine Primärpartikel in der Größenordnung von wenigen hundert Nanometern sich zu größeren, porösen Sekundärpartikeln von einigen Mikrometern agglomerieren [5]. Auf diese Art und Weise erhält man eine Verbesserung der elektrochemischen Eigenschaften, z.B. durch Verkürzung der Transportwege in kleinen Primärpartikeln, sowie eine gute Penetration mit flüssigem Elektrolyt durch die Porosität und vermeidet dabei den Nachteil von Nanomaterialien wie hohe Reaktivität und geringe Schüttdichte [5].

Beim abschließenden Ofengang sintern die Partikel zusammen. Bei diesem Vorgang verlieren die Partikel ein wenig an Porosität, erhalten jedoch auch Stabilität und eine gewisse Leitfähigkeit. Darüber hinaus wird hier die Kristallstruktur deutlich ausgeprägt. Die hier präsentierten Materialien kristallisieren alle in der Struktur der Schichtoxide vom Typ P2. Zur weiteren Untersuchung wurden vier verschiedene Sintertemperaturen $T_s = 850, 900, 950$ und $1000\,°C$ getestet. Mit diesen Temperaturen kristallisierten alle Materialien in der gewünschten P2-Struktur, die Morphologie der Partikel hängt jedoch sowohl von der chemischen Zusammensetzung als auch von der Sintertemperatur ab. Dies wurde mit Elektronenmikroskopie, Quecksilber-Porosimeterie und der Brunauer-Emmet-Teller (BET) Methode (spezifische Oberfläche) untersucht. Es wurde eine höhere Sinteraktivität von Partikeln mit hohem Eisengehalt beobachtet als von Partikeln mit einem hohen Nickelgehalt (siehe dazu Kapitel 5.1).

Des Weiteren wurden die elektronische und ionische Leitfähigkeit der vier Materialien nach dem Sintern ($T_s = 950\,°C$) mit Impedanzspektroskopie untersucht (Kapitel 5.2). Die beiden Leitfähigkeitsmechanismen sind stark von der chemischen Zusammensetzung abhängig. Eine Proportionalität zum Eisengehalt konnte hier nicht beobachtet werden.

Für den Vergleich weiterer Materialeigenschaften der vier Kathodenmaterialien mit $T_s = 950\,°C$ wurden Halbzellen gebaut und in situ Röntgendiffraktometrie durchgeführt. Typisch für Kathoden mit P2-Schichtstrukturen sind Phasenübergänge beim Aufladen sowie das Ordnen von Natrium-Leerstellen im Kristallgitter [6]. Diese Effekte ändern sich in ihrem Auftreten oder ihrer Ausprägung mit der chemischen Zusammensetzung (siehe

Kapitel 5.3). Für ein Kathodenmaterial wurde kein Phasenübergang beobachtet. Der Mechanismus des Leerstellen-Ordnens hingegen war nur bei einem (anderen) Kathodenmaterial stark ausgeprägt. Dies hat Auswirkungen auf das elektrochemische Verhalten.

Kapazitätstests mit verschiedenen Strömen (C-Raten) wurden an Halbzellen mit Natrium-Anoden durchgeführt (Kapitel 5.4). Dabei wurden auch drei verschiedene Potentialfenster getestet. Der Verlust der spezifischen Kapazität beim Zyklieren der Zellen kann mit der Reduktion der oberen Spannungsgrenze von 4.6 V auf 4.3 V bereits stark reduziert werden. Mit Hilfe der untersuchten Materialeigenschaften wie Partikelmorphologie, Leitfähigkeit, Phasenübergänge und Natriumleerstellen-Ordnen lassen sich Unterschiede beim elektrochemischen Zyklieren der Zellen verstehen. Eine individuelle Optimierung des Batterieverhaltens kann für jedes Kathodenmaterial durch die Wahl der Sintertemperatur und Anpassen des elektrochemischen Spannungsfensters durchgeführt werden. Aus der vorgelegte Arbeit geht hervor, dass auch mit reduziertem Nickelanteil Kathoden mit hohe Kapazität und Stabilität hergestellt werden können.

VII Abstract

The presented work is an investigation about the synthesis and characterization of cathode active material for sodium-ion-batteries. For some applications, this type of battery could potentially become an alternative to commercial lithium-ion-batteries, especially since it is expected that the demand for energy storage will rise significantly in the next decades [1–3]. The chosen materials for this study are the layered oxides $Na_{0.6}MO_2$ (with M representing a certain ratio of the metals Al, Ni, Fe and Mn). In order to replace nickel with iron, different chemical compositions were tested (see Chapter 3).
Spray drying was used to create so called hierarchically structured material. With this method it is also possible to create bigger amounts of cathode material [4]. A hierarchical structure results, if fine primary particles with the size of a few hundred nanometres agglomerate to bigger, porous secondary particles of a few micrometers [5]. This structuring can improve the electrochemical performance with short transport pathways inside the small primary particles and allows a good penetration with liquid electrolyte, while it avoids some disadvantages of nanomaterials such as high reactivity and low tap density [5].

In the final heat treatment step the particles sinter together, lose some of their porosity but gain stability and a certain amount of conductivity. On top of that, the crystal structure is distinctively developed during this step. All presented materials crystallize in the P2-type layered oxide phase. The influence of the sintering temperature T_s on the material properties was investigated for $T_s = 850, 900, 950$ and $1000\,°C$. In this temperature range, all materials crystallized in the desired P2-type structure, however the particle morphology strongly depended on both T_s and chemical composition. For a qualitative and quantitative investigation with scanning electron microscopy, Hg-porosimetry and the Brunauer-Emmet-Teller (BET) method (specific surface area) were carried out. It was observed that particles with high iron content exhibit a higher sinter activity than particles with high nickel content (see Chapter 5.1).

Furthermore, electrochemical impedance spectroscopy was used to measure the electronic and ionic conductivity of the four layered oxides after sintering with $T_s = 950\,°C$ (Chap. 5.2). Both conductivity mechanisms strongly depended on the chemical composition. A proportionality to the iron content could not be observed.

Half cells were built for the performing of in situ X-ray diffraction to compare additional material properties of the four layered oxides with $T_s = 950\,°C$. Typical for P2-type cathodes are phase transitions during charge and ordering of sodium vacancies in the crystal lattice [6]. Both effects are different in their appearance and magnitude for the individual chemical composition (see Chap. 5.3). This leads to different electrochemical behaviour.

Capacity tests with different currents (C-rates) were carried out on half cells with sodium-anode (see Chap. 5.4). A variation of the upper voltage limit was also tested.

Knowledge about the material properties such as particle morphology, conductivity, phase transition and sodium vacancy ordering helps to understand the cell performance. Each cathode material can be individually optimized towards good performance via the sintering temperature and the choice of the voltage window. The presented work demonstrates how high capacity and stability can be achieved even with reduced nickel content.

1 Introduction

Batteries are a milestone in technological development and part of our daily lives. Since Alessandro Volta's first device [7] not just energy density has improved significantly but also our understanding of the storage mechanisms. Other milestones are marked by the work of Goodenough [8], Whittingham [9] and Yoshino [10] on the development of lithium-ion-batteries (LIB). Just recently this work has been dignified with the Nobel prize in chemistry. Although many materials and chemistries have been tested and developed, LIB dominate a significant part of the battery market [11].

Global challenges such as the reduction of greenhouse gases urge for further advancements in energy storage systems [12]. In addition to batteries for mobile devices large scale stationary storage is considered to be a key technology to buffer the fluctuations of renewable energies in the power grid [12]. Besides high energy density and safety measures the cost of battery cells is a critical aspect in battery development [1]. The demand for energy storage devices is increasing along with the transition towards sustainable energy. Vaalma et al. [3] predicted in their work from 2018 that in the next decades until 2050 the demand for lithium and cobalt caused by the world wide battery industry alone will rise to a level well beyond supply production. The calculated demand from their work is shown in figure 1.1 (a). The calculated amounts for large and small batteries are shown separately in bright and pale colours. The calculation for the left-hand side of (a) was done for present-day cathode compositions. The authors also took into account that research about cathode compositions will proceed and therefore calculated demands for future but still fictive cathode materials with less nickel and cobalt (on the right of (a)). Vaalma et al. estimated that even with an expected annual growth of 2% production will not meet the demands of the battery industry (see Fig. 1.1 (b)). For Lithium they expected a demand which is below but close to the known Li reserves (based on the year 2018). However, before the reserves will run dry a supply risk is projected even with the mentioned annual growth in Li production. According to Vaalma et al. [3] the demand for Cobalt will exceed the today known reserves by about a factor of two. Only fictive Cobalt-poor cathode materials that might be the result of future research would reduce the demand to a level below (but still close) to the known reserves. In this case there would only be the same threat of supply risk as is predicted for Li. A 2% growth of production per year might help to mitigate this as well, but demands of other industries have not been taken into account yet.

From this analysis it becomes clear that the price of either of the two elements and with that of any battery system based on them will increase significantly over the next decades. Besides, lithium-alternative elements for energy storage can be found in sodium, magnesium and aluminium. Na, Mg and Al are about three orders of magnitude more abundant in the earths crust [13] and have been tested as battery materials [2, 14].

More about these alternatives is described in following chapters of the *Theory* section (Chap. 2). This dissertation will describe fundamental aspects of batteries and intro-
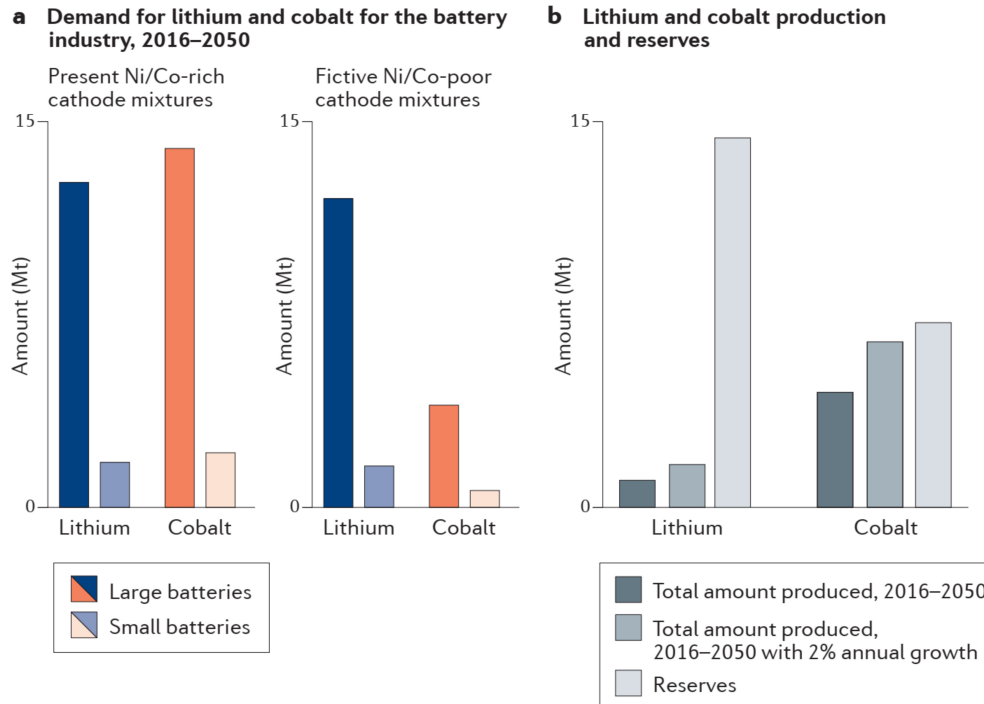
Figure 1.1: **Supply risk for Li and Co:** Taken from Vaalma et al. [3], reproduced with permission from Springer Nature. (a) Demand of the battery industry alone summed over several decades and split into large and small battery types. The left-hand side diagrams show calculated demands based on present battery compositions. On the right-hand side of (a) fictive cathode compositions with less Ni and Co are shown. (b) Produced amounts of Li and Co without and with 2% annual growth. These are compared to the known reserves as at 2018.

duce layered oxides as cathode materials for sodium-ion-batteries (SIB). On this basis the choice of the here investigated active material will be explained (Chap. 3). For the synthesis of precursor powders and the creation of structured, porous cathode material the spray drying method plays a key role (Chap. 4). Measured data of material properties such as specific surface are, porosity and crystal structure will be compared to the electrochemical performance in half-cells (Chap. 5).

2   Theory

2.1   Basics of electrochemistry

The fundamental principle of a rechargeable battery (secondary cell) is the same for all ion-based batteries, independent of the used ion and electrode materials. Three parts need to be present for a working cell: Cathode, electrolyte and anode. The positive electrode acts during discharge as the cathode (reduction), the negative electrode as anode (oxidation) and vice versa during charging. While the metal-ions travel between the two electrodes, the electrons take the path through an external circuit. The electrolyte connecting the two electrodes therefore needs a high ionic conductivity and a low electronic conductivity. A liquid electrolyte can be an organic solvent with dissolved salts. To keep the two electrodes from touching each other a porous separator soaked in liquid electrolyte is placed in between [15].

The energy storage mechanism is based on the introduction and removal of ions in the crystal structure of a host material (cathode and anode material). In electrochemistry this process can be described as intercalation or insertion. The term intercalation is used for storage of ions between layers of crystal structures (see next section), while insertion describes ion storage in a tunnel-like framework [15]. The electrode active material needs, besides its capability of a reversible storage mechanism, both high ionic and electronic conductivity. These conductivities depend on chemical composition, crystal structure and porosity of the active material [16]. Poor electronic conductivity can partly be compensated, when the active material is mixed with passive materials into the electrode slurry. Conductive carbon is typically used to enhance electronic conductivity in the electrode but does not participate actively on the storage mechanism. Another passive component is some sort of binder material for keeping a good contact between active material, conductive carbon and current collector. Different ratios of active material, conductive carbon and binder are possible. To increase the effective capacity per gram of the entire cell it is of interest to create cathode sheets with as much active material and as less carbon and binder as possible [15]. For experiments where new cathode materials (not yet optimized) are tested on their capacity and cycling stability usually a ratio of 80:10:10 (only 80 % active material mass) is chosen. With the big amounts of binder and conductive carbon it is ensured that the inactive components play a subordinated role and the measured performance is related mainly to the active material. Subsequent to the optimization of the active material the reduction of inactive components will lead to a higher capacity of the total electrode [15].

2.2   Post-lithium batteries

The before mentioned, alternative battery systems with chemistries beyond lithium can be summarized in the term *post-lithium* energy storage. Figure 2.1 shows a comparison of the gravimetric and volumetric energy density of several alkali metals, alkaline earth metals and aluminium. Shown as well is their abundance in the earth's crust and their reduction potential versus normal hydrogen electrode (NHE) (taken from Elia et

al. [17]). Since lithium is the lightest of these elements, it is plausible that it exhibits the highest gravimetric capacity. Its relatively high volumetric capacity is only exceeded by magnesium and aluminium. It needs to be noted, however, that for an application in general a pure alkali metal anode is problematic due to safety concerns. Alternative anode materials such as graphite and hard carbon put the anodic capacities into a new perspective. Cathodic capacity limits the total capacity on the other side of the cell. The choice of cathode and anode material determines the cell voltage, which is influenced by the used metal-ion. All post-lithium metals show a higher reduction potential. The resulting voltage of a full cell depends on the difference of the anodic and cathodic redox potentials, therefore influencing the energy density as well. In addition to the electro-chemical data it is visible that lithium is by three orders of magnitude less abundant than the other five metals [17].

Sodium-ion based batteries are closest to practical application among these post-lithium systems [17] and on the brink of commercialisation, with several companies putting efforts into them [18]. SIBs are considered to be a promising alternative battery system to LIBs not in terms of replacing them completely but rather in reducing costs especially for large scale stationary application. On top of that it needs to be noted that for SIB no cooper foil as current collector is necessary. Aluminium, which is the 3rd most abundant element in Earth's continental crust, can be used as a cheap current collector on both electrodes [2, 3].
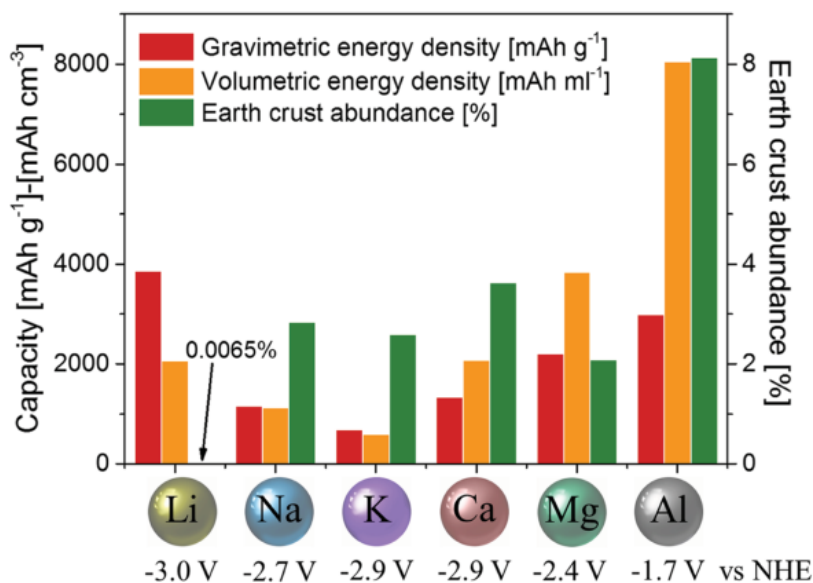
Figure 2.1: **Metal anodes:** Comparison of anodic capacities per mass and per volume. Additionally, their abundance in the Earth's crust and their standard reduction potentials are shown. Taken from Elia et al. [17], reproduced with permission from John Wiley and Sons.

Besides both capacities (gravimetric and volumetric) it is necessary to consider the average cell voltage for the resulting energy density. The reduction potential vs NHE in Figure 2.1 gives an impression about that, but the open circuit potential is a result of the used cathode and anode material. Cycling the materials in a certain electrochemical window (ECW) defines the average voltage (AV) of the cell [15, 19]. From AVs and the capacities the specific energy can be calculated. In case of half-cells, where an active material is cycled versus the a pure metal anode of the chosen ion the specific energy is calculated accordingly to

$$W = Q_{cathode} \cdot AV_{cathode} \tag{1}$$

For full cells, where the both anode and cathode act as ion storage the specific energy of a cell is

$$W = \frac{Q_{cathode} \cdot (AV_{cathode} - AV_{anode})}{1 + Q_{cathode}/Q_{anode}} \tag{2}$$

With Q_j being the specific capacities of anode/cathode and AV_i the corresponding average voltage [1]. Considering the volume or weight on cell level results in volumetric and gravimetric energy density as it is shown for several battery types in Figure 2.2. Each battery system covers an area in this plot due to the explained dependence on the actual chosen active materials. Electric vehicles manufactures usually choose cathode materials with high energy densities such as Lithium-Nickel-Cobalt-Aluminium-Oxide (NCA) and Lithium-Nickel-Manganese-Cobalt-Oxide (NMC) [21, 22]. Cells with Lithium-Iron-Phosphate (LFP) cathodes exhibit a lower energy density as NMC and NCA [1], which is why LFP was considered to be rather used as stationary application [23, 24]. However, in the recent years also vehicle manufacturers started to change their used battery chemistry towards the more safe and low-cost LFP [22]. The overlap in Figure 2.2 of SIB with LIB systems demonstrate that the sodium technology is competitive with some lithium technologies such LFP [24].

2.3 Layered Oxides

A promising candidate as cathode active material (CAM) for SIBs are layered oxides. They are known for their high average working potential and high specific capacity. Like their LIB counter parts, their crystal structure consists of layers of transition metals (TM). Li and Na ions can intercalate between those layers. Various TMs (e.g. Mn, Fe, Co, Ni) and combinations of different TM amounts have been investigated and influence the electrochemical performance [25].

2.3.1 Crystallographic properties

Two main groups of layered oxides can be identified: P2-type and O3-type, where the environment of the sodium ion has either a prismatic or an octahedral shape respectively.
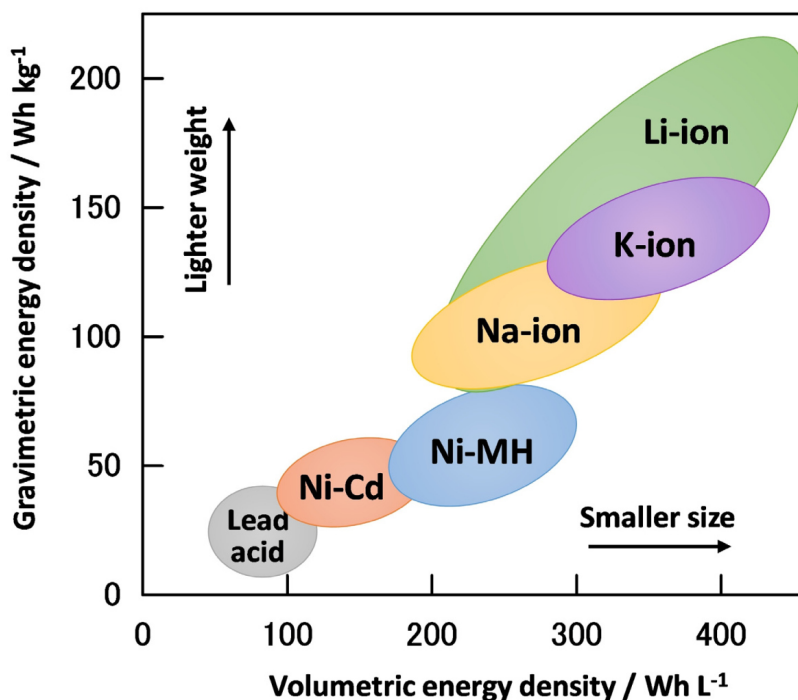
Figure 2.2: **Energy density:** Gravimetric and volumetric energy densities of several battery chemistries. Instead of one specific data point in the plot the systems cover an area, due to the range of different cathode and anode composition. Different types of battery casings may also influence the effective density. Taken from Kubota et al. [20], reproduced with permission from John Wiley and Sons.

A sketch of these structures is shown in Figure 2.3. The numerals 2 and 3 describe the numbers of non-equivalent TM layers (for P2: AB BA & for O3: AB CA BC). P3-type and O2-type materials represent also a possible class of materials but typically only occur during electrochemical cycling. In case of a P2-type layer, the diffusion of sodium ions follows a direct path. This lowers the diffusion energy barrier as compared to O3-type layer and makes P2-type a better cathode material candidate in terms of transport kinetics [26]. A disadvantage of P2-type materials is their sodium deficiency. In half cells, where the anode can provide additional sodium the deficiency is less problematic. However, in full-cells it results in less accessible capacity. Pre-sodiation of electrodes might solve this issue but poses another challenge to be addressed [27]. O3-type materials are advantageous in this matter since there is no sodium deficiency present [28]. A disadvantage is the poor air stability of the O3-phase, which results from insertion of air moisture into the layered structure [28]. In terms of industrial application this instability is problematic.
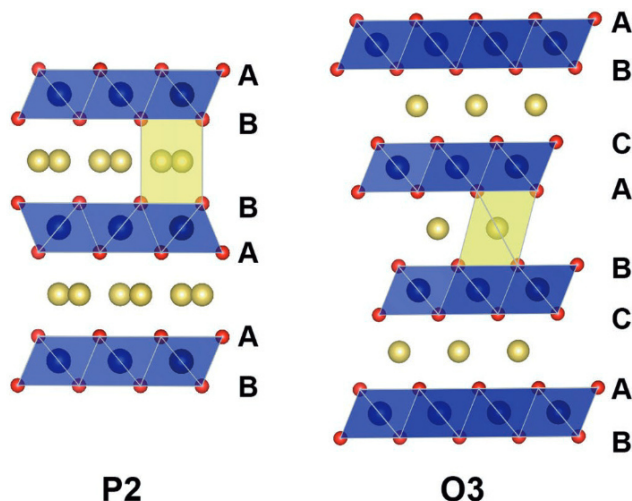
Figure 2.3: **Layered oxides:** Schematic description of the crystal structure of two layered oxides from the type P2 and O3. The sodium ions are represented as yellow spheres and their environment (prismatic or octahedral) is indicated in pale yellow. The layers of transition metals are blue with red oxygen at the corner. Taken from [29], reproduced with permission from Wiley and Sons.

In this work several P2-type materials are presented. In general P2-types are formed at higher temperatures (650 °C to 900 °C) and with a sodium content of $0.3 \leq x \leq 0.7$ in the formula $Na_x TMO_2$. A detailed phase diagram of $Na_x CoO_2$ was presented by Lei et al. [30]. Increasing the sodium content beyond 0.7 will result in a different crystal structure, in general a O3-type material. In the prismatic (P-type) environment there are two possible sites for Na ions: Na_1 (or Na_f) and Na_2 (or Na_e). Neighbouring Na_1 and Na_2 sites can not be occupied at the same time due to the big ionic radius of Na^+. The repulsion force between neighbouring ions results in an ordering of sodium vacancies, a so-called superstructure. This brings a certain disadvantage [25]: Vacancy ordering leads to an ordered intermediate phase. A rearrangement of this order results in multiple voltage plateaus and exhibits diffusion barriers for Na^+ ions. Absence of distinguishable plateaus indicates a solid-solution reaction without a superstructure and without the related Na-vacancy ordering diffusion obstacles. This smoothing of the plateaus can be achieved by incorporation of other transition metals into the layers and increase the battery performance at higher C-rates via faster ionic transport [31].

2.3.2 Examples from literature

An example for a stable high voltage material was shown by Wang et al. [31] who substituted half of Mn in $Na_{2/3}Ni_{1/3}Mn_{2/3}O_2$ with Titanium. The resulting material P2-$Na_{2/3}Ni_{1/3}Mn_{1/3}Ti_{1/3}O_2$ delivered 87 mAh/g with a high average potential of 3.5 V. 84% of the capacity was maintained after 500 cycles with 1C between 2.5-4.15 V, whereas the

Table 2.1: **Literature overview:** Different chemical compositions for P2-type layered oxide CAMs. Shown is their average voltage (AV), the electrochemical window (ECW) in which they were cycled, the current I or C-rate, specific capacity Q_{spec} and its retention over the investigated cycles.

Material	AV in V	ECW in V	I	Q_{spec} in mAh/g	Stability %, cycles	Source
$Na_{2/3}Ni_{1/3}Mn_{1/3}Ti_{1/3}O_2$	3.5	2.5-4.15	1C	87	85%, 100	[31]
$Na_{0.66}Ni_{0.26}Zn_{0.07}Mn_{0.67}O_2$	3.56	2.0-4.4	12mA/g	142	83%, 30	[32]
$Na_{0.67}Mn_{0.67}Ni_{0.28}Mg_{0.1}O_2$	3.7	2.5-4.35	0.1C	115	92%, 100	[33]
$Na_{0.6}Mn_{0.65}Fe_{0.2}Ni_{0.15}O_2$	3.1	1.5-4.3	0.05C	200	75%, 50	[34]
$Na_{0.5}Ni_{0.23}Fe_{0.13}Mn_{0.63}O_2$	3	1.5-4.6	15mA/g	200	70%, 70	[35]
$Na_{0.6}Al_{0.11}Ni_{0.22}Mn_{0.66}O_2$	3.1	1.5-4.6	20mA/g	240	80%, 50	[36]

decay without Ti substitution was already stronger after 100 cycles.

With the chemical composition P2-$Na_{0.66}Ni_{0.26}Zn_{0.07}Mn_{0.67}O_2$ Wu et al. [32] achieved a higher capacity as compared to Wang et al. With a similar average potential of 3.56 V a capacity of 142 mAh/g was achieved due to the broader window of 2.0 - 4.4 V. With electrochemical inactive Zn the performance was more stable than with a Zn-free composition. However, the 83% retention of the above mentioned 142 mAh/g where already reached after only 30 cylces with a current of 12 mA/g.

Wang et al. [33] used Mg as the substitutional element for P2-$Na_{0.67}Mn_{0.67}Ni_{0.28}Mg_{0.1}O_2$ with an average working potential of about 3.7 V in the window of 2.5-4.35 V delivered, 115 mAh/g and showed a good retention of 92% after 100 cycles though just with a small rate of 0,1C. Nevertheless it became clear that the method of TM doping/substituting is beneficial for the electrochemical behaviour in terms of influencing or suppressing the P2-O2 phase transition.

When looking for high-capacity cathode materials one often finds materials with high iron and manganese content but there is still a smooth transition between high-voltage (nickel-based) and high-capacity (manganese-based) [25]. With the redox couples Fe^{3+}/Fe^{4+} and Mn^{3+}/Mn^{4+} high specific capacities can be achieved. However, Mn^{3+} is problematic due to unstable Jahn Teller distortion, which can be one reason for poor capacity retention.

Yuan et al. [34] investigated the chemical composition $Na_{0.6}Mn_{0.65}Fe_{0.2}Ni_{0.15}O_2$. When cycled between 1.5-4.3 V and average potential of 3.1 V it delivered 200 mAh/g and maintained 75% of it after 50 cycles. It needs to be pointed out, that a small current of 14mA/g = 0.05C was used.

Hasa et al. synthesized two P2-type candidates with high specific capacity: $Na_{0.5}Ni_{0.23}Fe_{0.13}Mn_{0.63}O_2$ with average voltage of ca. 3 V. Cycling with 15 mA/g over 1.5-4.6 V resulted in 200 mAh/g and 70% retention after 70 cycles [35]. Further work on the second material $Na_{0.6}Al_{0.11}Ni_{0.22}Mn_{0.66}O_2$ delivered very high capacity of 240 mAh/g in the window of 1.5-4.6V, when cycled with a current of 20mA/g. Here, the

small amount of inactive Aluminium was one strategy to reach a retention of 80% after 50 cycles [36].

An overview of the mentioned literature is summarized in table 2.1. A possible comparison of these sodium based layered oxides can be found in the commonly used lithium based layered oxide NMC (Ni-Mn-Co). NMC is widely used in the battery market [37]. Different ratios of these three transition metals also influence the average voltage and specific capacities ot this cathode material just like for the sodium system. Li-NMC type cathodes deliver cathodic capacities in the range of $150\,mA\,h\,g^{-1}$ to $200\,mA\,h\,g^{-1}$ and an AV of approx. $4\,V$ [37]. The values obtained for SIB from table 2.1 are lower than those for LIB, but the SIB cathode materials are still able to deliver decent capacities and voltages in the same range without lithium and cobalt.

2.3.3 Degradation mechanisms

Some layered oxides exhibit high specific capacities as presented in Table 2.1. However, a challenge for the application of SIBs is the capacity fading. Different degradation mechanisms can lead to irreversible loss of capacity.

The Jahn-Teller effect is a geometrical distortion of molecules or ions with a certain electron configuration. Several electron configurations of a non-linear molecule can be possible and have the same energy eigenvalue (degeneracy). It is possible, that a distortion of the symmetry reduces the total energy and cancels the degeneracy [38]. This effect becomes relevant for layered oxides when manganese is present. High-spin Mn^{3+} can lead to structural distortions in the layered structure and hence reduce cycling stability and rate performance [39]. It is therefore known as Jahn-Teller-distortion [40]. In case of P2-type layered oxides the distortion can be expected when Mn^{4+} is reduced to Mn^{3+} at around $2.0\,V$ vs. Na/Na^+ [36].

During charging to high voltages (beyond ca. $4.1\,V$ vs. Na/Na^+ [6]) P2-type undergoes a phase transition to O2-type with the OP4 phase as an intermediate stage. These transitions are induced by gliding of the TMO_6 octahedra and result in contraction along the lattice parameter a, expansion along parameter c and volume change of the crystal structure [6, 25]. Volume change in the lattice is known to cause crack formation in the cathode active material, which might result in contact loss between active material and current collector [41]. Besides the crack formation a capacity fading can arise from the phase transition itself, which is not always reversible [6].
Another effect in the high voltage region (beyond $4.0\,V$), which can lead to the mentioned irreversible phase-transition is the formation of an oxygen anionic group $[O_2]^{x-}$ $(0 < x < 4)$ [42]. Oxygen of the lattice can participate in the redox reaction. This can happen as charge compensation when the transition metal oxides are charged to high voltages [43]. Since the oxygen of the lattice gets lost, this effect can cause irreversible capacity degradation.

2.3.4 Substitution of elements in the crystal framework

One possible strategy to overcome the poor cycling and rate stability is substituting Ni or Mn with a small amount of another transition metal or electrochemical inactive metal such as Mg, Al, Ti, Zn, Fe or Y [44]. Some of these were used in the mentioned literature in Table 2.1. These dopants can help to suppress the phase transition and volume change [45] or increase oxygen stability [44]. Using a dopant with similar ionic radii, such as aluminium, makes a substitution in the crystal lattice easier. The change of the local atomic arrangements can improve the electronic conductivity and stability [46].

Examples from literature with layered sodium oxides showed the beneficial effect of these dopants. Doping with Zn was found to prevent sodium-ion vacancy ordering and increased the average cell voltage and cycling stability [32]. Introducing magnesium improved capacity retention due to less Jahn-Teller active Mn^{3+} and by delaying or suppressing the high voltage phase transition [33, 47]]. Aluminium as a dopant was also found to mitigate the Jahn-Teller-effect and provides access to more sodium by increasing the lattice volume [48]. Being electrochemical inactive, Al can help to improve bulk and surface stability of the active material, which results in a better electrochemical performance and higher cycling stability [46].

2.4 Hierarchically structured materials

Another way to improve the electrochemical performance and reduce capacity fading is a smart electrode design on the micrometer scale. For LIB systems it has been shown that active materials with micro- and nanosized particles are a favourable approach to increase initial specific capacity and capacity retention upon cycling. One reason for that are reduced transport paths inside the active material. This also has a positive effect on the rate capability [5]. The same improvement can be achieved for SIBs where the transport of Na^+ ions inside the active material is even a bigger problem due to their more sluggish transport kinetics as compared to Li^+. Nanomaterials are however difficult to handle on an industrial scale. The big surface area leads to a high reactivity and low tap density [5, 25]. To overcome these problems Wagner et al. [5] proposed a hierarchical structure of spherical LIB particles (secondary) that are made up from nanosized (primary) particles.
Spray drying is a possible method to create micrometer sized powders with a hierarchical structure with a high tap density [4, 49]. A solution or a suspension with the material of interest can be sprayed with a nozzle or an atomizer wheel. The droplet size is determining the subsequent sizes of the powder particles. The atomization takes place in a stream of hot gas (e.g. air, nitrogen) at the top of the spray drying chamber. This leads to a rapid evaporation of the liquid and renders solid powder particles to travel in the stream of the gas until it the powder is gathered, usually in a cyclonic flow chamber. Increasing the atomizers speed or reducing the viscosity of the liquid results in smaller droplets and therefore smaller powder particles [50]. Due to an easy upscaling of the produced amounts, spray drying is also a promising method to produce battery
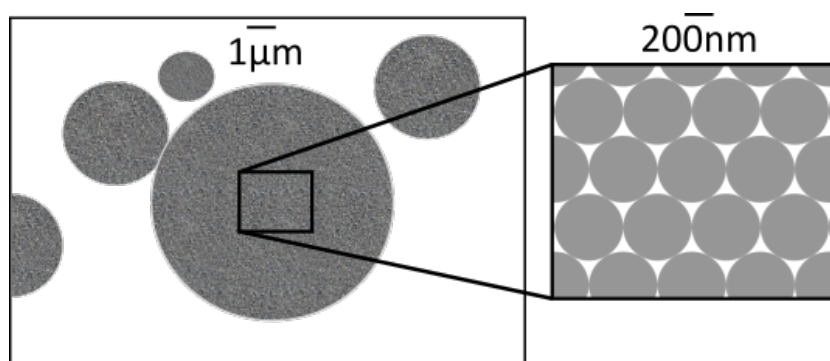
Figure 2.4: **Drawing of a hierarchical structure:**   A possible morphology of hierarchically structured material could look like microspheres made from smaller particles with pores in between.

materials on an industrial scale [51].

In the recent years the numbers of publications related to spray drying electrode materials for SIBs increased [51]. However, best to our knowledge, just little understanding of tuning the morphology properties with process parameters has been gained for SIB materials. In this work we present a similar approach based on spray drying to receive hierarchically structured cathode materials with layered oxides for SIBs. Figure 2.4 shows a drawing of how a hierarchical structure can look like: Some spherical secondary particles with different sizes and diameters of several micrometers represent the powder of an active battery material. On closer inspection one can see that these micrometer-sized spheres consist of many, small primary particles which are joined together. However, they are not completely densely packed so that a secondary particle is porous. Porosity plays a key role in the electrochemical behaviour. During charge and discharge most active materials undergo volume changes. Pores act as free space between the primary particles and can buffer the volume expansion. This mitigates crack formation and therefore prevents loss of electric contact. As compared to a completely dense particle a porous particle allows more penetration of liquid electrolyte. This brings the advantage of shortened transport paths with reduced solid state diffusion while more of the active material can be reached directly from the electrolyte. This brings higher specific capacity and also improves the rate-capability with higher C-rates (e.g. 5C or 10C) as compared to a dense cathode material [5, 52].

$$Na_{0.6}Al_{0.11}Ni_{0.22}Mn_{0.66}O_2 \quad (NANMO)$$

$$Na_{0.6}Al_{0.11}Ni_{0.11}Fe_{0.11}Mn_{0.66}O_2 \; (NANMFO)$$

$$Na_{0.6}Al_{0.11}Fe_{0.22}Mn_{0.66}O_2 \; (NAFMO)$$

$$Na_{0.6}\, Fe_{1/3}Mn_{2/3}O_2 \, (NMFO)$$
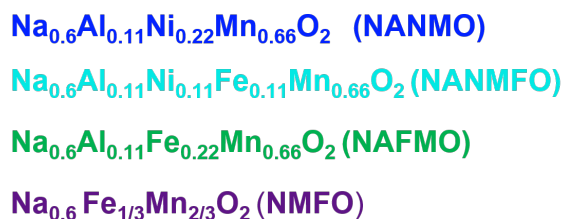
Figure 3.1: **Material overview:** Four different chemical compositions were synthesized. The colour changes from highest Ni-content to highest Fe-content: Blue, cyan, green, purple

3 Choice of cathode material

The idea of the presented work was to use a cathode material for sodium-ion-batteries which shows a high initial specific capacity and improve its stability with a hierarchical structure as described in chapter 2.4.

In chapter 2.3 *Layered Oxides* one of the presented cathode material showed high capacity and stability. This composition was considered to be a promising candidate for SIB. P2-$Na_{0.6}Al_{0.11}Ni_{0.22}Mn_{0.66}O_2$ (NANMO) from the work of Hasa et al. [36] is made from the top 12 earth abundant elements [2]. This meets the purpose of sustainability described in Chapter 1. Nickel however is an exception to that which ranks in the same order of magnitude as Li, Co and Cu [2]. In terms of expense, nickel (together with cobalt, not present here) is a significant cost driver for battery materials [1] and the toxicity of nickel makes it questionable for a sustainable battery chemistry [1,53]. Since the self-declared purpose of this work is to reduce the amount of critical and toxic elements it is necessary to consider alternatives to nickel as well.

Nomenclature

In this work we present the synthesis of four different SIB cathode materials. Starting with the material from [36] $Na_{0.6}Al_{0.11}Ni_{0.22}Mn_{0.66}O_2$ (NANMO) the nickel content will be stepwise substituted with iron. $Na_{0.6}Al_{0.11}Ni_{0.11}Fe_{0.11}Mn_{0.66}O_2$ (NANMFO) contains only half the amount of Ni. Replacing Ni completely with Fe to $Na_{0.6}Al_{0.11}Fe_{0.22}Mn_{0.66}O_2$ (NAFMO) is one of the Ni-free materials. In a final step the electrochemical inactive Al will as well be replaced which leads to the material $Na_{0.6}Fe_{1/3}Mn_{2/3}O_2$ (NMFO).

Figure 3.1 shows an overview of the synthesized materials mentioned before, listed from highest nickel to highest iron content. The presented colour code (blue, cyan, green, purple) will be used in the following and allows simple distinguishing between the four cathode materials. All four materials were processed under the same conditions for easy comparison. To achieve a hierarchically structured material as described in chapter 2.4, spray drying was chosen as centrepiece of the synthesis process. The synthesis involves two oven heat treatments (see Chap. 4 *Experimental* and 5.1.1 *Morphology*). When in the following different temperatures and their influence are discussed this referrers to the

second heat treatment (sintering). The presented work gives a good overview on how the resulting properties like morphology, electrochemistry, conductivity, etc. depend on the chemical composition and how they can be tuned by changing a process parameter, e.g. sintering temperature.

4 Experimental

4.1 Material characterization

During and after the synthesis the material properties were investigated with the methods summarized hereafter.

The decomposition of the precursor powders was investigated by means of thermogravimetric analysis (TGA) using an *STA 449 F3* (Netzsch). A *Supra 55* (Zeiss) scanning electron microscope (SEM) was used to visualize the morphology of primary and secondary particles. SEM was also used to investigate cross-sections of particles, electrodes and pellets. An acceleration voltage of 10kV and the secondary electron signal was used to take the SEM-pictures. The specific surface area was investigated with a *Gemini VII 2390a* (NSA, Micromeritics) and calculated using the Brunauer-Emmet-Teller (BET) method. Porosity of the powder's particles was measured with mercury intrusion with a *CEI Pascal 1.05* (Thermo Electron). To control the chemical composition of the cathode materials, inductive coupled plasma optical emission spectroscopy (ICP-OES) was performed (iCAP 7600 Duo, Thermo Fisher Scientific). The carbon content was measured with a CS-analyser and the oxygen content was determined with carrier gas heat extraction (TGHE). The particle size distribution was measured via laser diffraction (Horiba LA950, Retsch Technology). A 0.03 M solution of tetrasodium pyrophosphate in water was used to stabilize the suspension during laser scattering measurement. Mößbauer spectroscopy was used to investigate the Fe^{3+}:Fe^{4+} ratio of the three iron containing samples (NANMFO, NAFMO, NMFO) in their pristine state (after synthesis) and after being fully charged. Measurement of ^{57}Fe Mößbauer spectroscopy was performed at room temperature on a WissEL constant-acelleration spectrometer in transmission mode with a $^{57}Co(Rh)$ source. X-ray diffraction (XRD) was performed ex situ on a *D2-Phaser* (Bruker) with Cu radiation and a mean wavelength of $\lambda = 1.54184\,\text{Å}$ with K_{α_1} and K_{α_2}.

4.2 Synthesis

The complete synthesis process is summarized in Figure 4.1 and consists of six steps. In few sentences it can be summarized as follows: The different educts were dissolved separately in distilled water and were then combined and stirred. Using the spray dryer *Mobile Minor* (shown on pictures) from GEA the solution was spray dried with an inlet temperature of 200 °C and an outlet temperature of 108 °C. The obtained precursor powders received a two-step heat treatment. The first heat treatment was done at 1000 °C in air to remove the organics of the reactants. Grinding in a *Pulverisette 5* planetary mill (shown in picture, made by Fritsch) with 3mm ZrO_2 spheres in distilled water for 24 h (setting 5: planetary disk at 206 rpm, bowl at 447 rpm) resulted in an aqueous suspension of fine primary particles. This suspension was spray dried again with the same parameters as before into a fine powder of secondary particles. With the second heat treatment at different temperatures in air the final morphology and crystal structure was established. Choosing different temperatures from 850, 900, 950

14

Process step	Step I *Aqueous solution*	Step II *1st Spray drying*	Step III *1st Heat treatment*	Step IV *Grinding*	Step V *2nd Spray drying*	Step VI *2nd Heat treatment*
	$C_2H_3NaO_2$ $C_4H_6MnO_4$ $Al(NO_3)_3$ $C_4H_6NiO_4$ $Fe(NO_3)_3$	Severe evaporation → Unstable structure → Grinding			Stable structure	
Amount per step	1-3 Liters	200-500g	25 - 60g	≥ 50g	Ca. 35g	100-300g
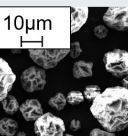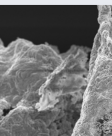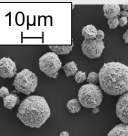
Figure 4.1: **Synthesis process:** The synthesis can be separated into six individual steps. A typical used amount per step is shown in the last row.

and 1000 °C influences these properties, which is relevant to their electrochemistry (see Chap. 5.4). Dwell time was 6h in all cases.

As mentioned before, spray drying is the centrepiece of the synthesis procedure since it provides the hierarchical structure and is suitable for upscaling [51]. In the following the different steps and their specialities or challenges are described in detail.

4.2.1 First spray drying: Precursor production

Since the presented cathode active materials (CAM) are not yet commercially available, the precursor materials need to be created from basic chemicals (steps I and II in Fig. 4.1). The creation of hierarchically structured CAM demands control only over the second half of the process presented in Fig. 4.1: Wagner et al. [5] bought commercial Li-NMC111 and started their process of grinding and spray drying (step IV in Fig. 4.1), which is described in Chap. 4.2.3. The synthesis presented here started with acetates and nitrates as educts.

Sodium acetate anhydrous $C_2H_3NaO_2$ (99 % Merck), aluminium nitrate nonahydrate $Al(NO_3)_3 \cdot 9\,H_2O$ (98 % Acros Organics), nickel(II) acetate tetrahydrate $C_4H_6NiO_4 \cdot 4\,H_2O$ (99 % Aldrich Chemistry), iron(III) nitrate nonahydrate $Fe(NO_3)_3 \cdot 9\,H_2O$ (98 % Alfa Aesar), manganese(II) acetate tetrahydrate $C_4H_6MnO_4 \cdot 4\,H_2O$ (99 % Aldrich Chemistry)

15

Table 4.1: **Synthesis quantity:** Here are the amounts of the different acetates and nitrates for all four precursors presented in gram. For NMFO thrice the amount was synthesized.

	NANMO	**NANMFO**	**NAFMO**	**NMFO**
$C_2H_3NaO_2$	50.76	50.94	51.09	147.61
$C_4H_6MnO_4 \cdot 4\,H_2O$	166.84	167.35	167.9	490.02
$Al(NO_3)_3 \cdot 9\,H_2O$	42.14	43.13	43.26	-
$C_4H_6NiO_4 \cdot 4\,H_2O$	56.46	28.34	-	-
$Fe(NO_3)_3 \cdot 9\,H_2O$	-	46.45	93.17	407.86

were used in this process. The masses used for the four precursors are presented in Table 4.1 in grams, based on calculations for the necessary ratio of the (alkali) metals. Purity of the chemicals was considered in the calculation of the necessary masses. In the case of NMFO three times the amount was used in the precursor's synthesis, which is simple to increase for the spray drying process, demonstrating the potential for upscaling.

The chemicals are soluble in water. For the synthesis distilled ultra pure water was used to prevent contamination in step I (compare to Fig. 4.1). The different water volumes used for dissolving the educts were chosen based on previous synthesis experience with lithium CAM precursors at the institute. NANMFO can be used as reference here since it contains all used chemicals: Na acetate was dissolved in 250 mL, Mn acetate in 500 mL, Al nitrate in 250 mL, Ni acetate in 250 mL and Fe nitrate in 250 mL water. The water volumes were scaled to the amounts of educts: E.g. for NAFMO the Fe nitrate was dissolved in 500 mL. Hence a typical synthesis batch corresponds to a volume of 1.5 L, or in case of NMFO 4.5 L. To ensure complete dissolution the educts were stirred in separate beakers overnight. The water in the beaker with Ni-acetate was heated to 60 °C for approx. 2h and then stirred at room temperature overnight. This was done due to the low solubility of Ni-acetate. After that the separated solutions were combined in one single beaker and stirred for another two hours.

During this time the spray dryer (see Fig. 4.1 step II) was heated to the desired temperatures. When the inlet temperature $T_{in} = 200\,°C$ and outlet temperature $T_{out} = 108\,°C$ were stable the solution was still stirred and supplied to the spray dryer via a feed pump. The atomizer wheel atop the spray dryer was set to maximum speed of ca. 32 000 rpm during the entire process. A solution of 1.5 L took approx. two hours to spray dry. The used spray dryer allowed to collect two types of powder granularity: At the bottom of the central spray drying chamber right underneath the atomizer wheel the so-called „tower fraction" was collected: Big and heavy particles fell down into a container. Smaller and lighter particles were swirled by the permanent carrier gas stream and carried on, to be collected after the „cyclone" chamber. Typical amounts for the synthesis with 1.5 L were 160 g of cyclone- and 60 g of tower-fraction. A distinction between these two fractions at this point was not yet necessary because of the following steps III and IV. It is

(a)   (b)
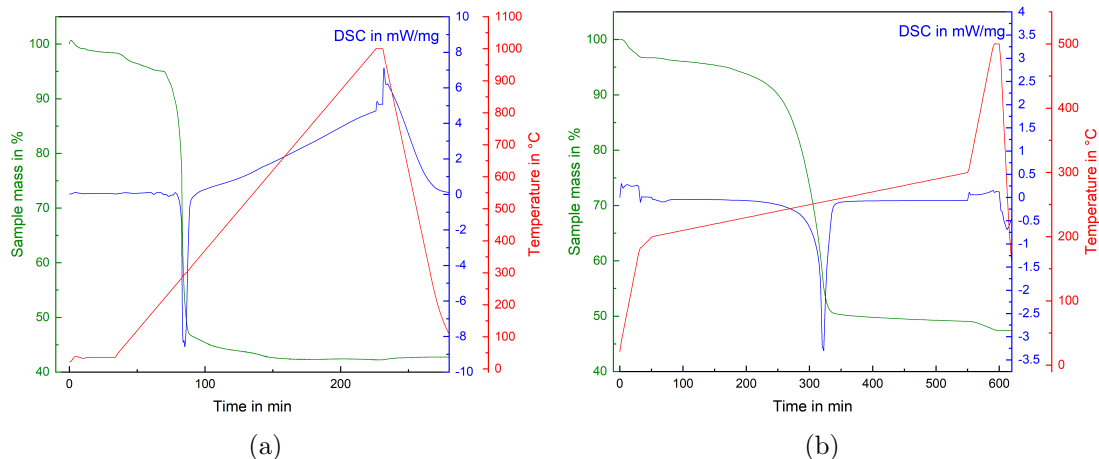
Figure 4.2: **Thermogravimetric analysis:** A sample of the NANMO precursor was heated in air at two different rates: (a) $5\,\mathrm{K/\,min}$ to $1000\,°\mathrm{C}$ and (b) in the range of $200\,°\mathrm{C}$ to $300\,°\mathrm{C}$ with a rate of $0.2\,\mathrm{K/\,min}$. The displayed curves are sample mass (green), differential scanning calorimetry (DSC, blue), and temperature (red).

however necessary in step V (second spray drying). Here after step II the two fractions were combined, resulting in ca. $220\,\mathrm{g}$ of precursor powder. In the case of NMFO with triple the amount of educts approx. $600\,\mathrm{g}$ of powder were obtained, demonstrating the upscaling potential. This concludes synthesis steps I and II. The powder obtained in step II is shown in a SEM picture in Figure 4.1. The particles have a wrinkled surface and appear not to be porous.

4.2.2 First heat treatment and challenge

In step III the first heat treatment was done in air, so it can be described as calcination. The powders were heated in aluminium oxide crucibles to $1000\,°\mathrm{C}$ with a dwell time of $6\,\mathrm{h}$ in a *CWF 13* oven (Carbolite Gero). A constant air flow of $80\,\mathrm{L\,h^{-1}}$ was regulated. Step III enables two transformations of the material: In the $250\,°\mathrm{C}$ to $400\,°\mathrm{C}$ region the organic parts of the precursor decompose and its products evaporate as gases. In the higher region of $850\,°\mathrm{C}$ to $1000\,°\mathrm{C}$ the crystal structure is developed. More information on the crystal structure development at different temperatures will be given in Chapter 5.1.4.

However, the evaporation of organic components was problematic; this can be understood with the data from thermogravimetric analysis (TG) and differential scanning calorimetry (DSC), shown in Figure 4.2. The measurements were done in synthetic air atmosphere, analogous to the heat treatment in step III. The first measurement, shown in Figure 4.1 (a), was performed by heating a NANMO sample at a rate of $5\,\mathrm{K/\,min}$ until a temperature of $1000\,°\mathrm{C}$ was reached. The development of the sample mass (green),

the DSC value (blue) and the temperature (red) are shown. Until approx. 200 °C the sample mass slowly decreases while no significant change in the DSC-curve is present. In a small window between ca. 250 °C to 300 °C a significant drop in the sample mass of almost 50 % is visible, with an exothermic peak in the DSC curve at the same time.

This can be interpreted as follows: At the beginning a small mass loss between 100 °C to 200 °C occurs due to water evaporation. In the region of 250 °C to 300 °C the strongest mass loss is related to the decomposition and evaporation of the organic part of the precursors. This explains the exothermic DSC peak as well. After that no other evaporation or mass loss occurs.

Since the strong mass loss at ca. 250 °C occurs in a rather narrow temperature window, this measurement was repeated with different heating rates: In (b) of Figure 4.2 the rates shown are 5 K/ min to 180 °C, continuing with 1 K/ min to 200 °C, followed by 0.2 K/ min to 300 °C and finally 5 K/ min again to 500 °C. The region of severe mass loss is now visible more clearly: 230 °C to 257 °C. Beyond 257 °C no other evaporation was detected.

This shows that even at a rate this slow the decomposition of half the sample mass into the gas phase is complete in two hours. To continue the synthesis with steps IV and V (grinding and spray drying) bigger sample amounts of at least 50 g (after mass loss) were needed for a proper spray drying procedure. However 25 g to 60 g of precursor powder lead to an overflowing of the crucible due to severe decomposition and therefore some loss of sample material in the interior of the oven. Closing the crucible with a lid was no option, since this would have blocked the stream of air atmosphere from the sample. Repeating step III several times with small samples amounts was possible, but laborious and inefficient. In regard to upscaling this seemed to be less handy. The severe decomposition of the organic parts is also the reason why there are no more particles visible in the SEM pictures as seen at step III in Figure 4.1. The particle structure is destroyed during the abrupt evaporation of decomposition products and leaves big chunks without any particle morphology or hierarchical structure. This is the reason why the synthesis was continued with the grinding of this chunk-like material to be spray dried again.

For grinding at least 50 g of calcinated material was necessary as mentioned before. To overcome the problem of overflowing, several tests were performed and the following approach turned out to be acceptable: Crucibles with high walls and large ground area (135 mm height, 160 mm length, 135 mm width) resulted in less material overflowing the walls. A crucible lid with 9 holes of 10 mm diameter (custom product) was used and an even slower heating rate in the critical region of severe evaporation was employed: An initial rate of 5 K/ min to reach 180 °C, then 1 K/ min to 220 °C, 0.1 K/ min to 280 °C, and finally 5 K/ min to 1000 °C, before letting dwell for 6 h and then letting cool down to room temperature at an average rate of 1.3 K/ min (no active cooling). This heating procedure with about 20 h of active heating was a pragmatic approach to calcinate up to 80 g of precursor powder in one run with reasonable heating time. Higher amounts were not possible due to the limited capability of the oven to remove exhaust gas from the sample evaporation. When thinking about upscaling one must take into account that

half the sample mass evaporating in a small period of time can exceed the limits of the used ovens.

4.2.3 Milling and second spray drying

Milling was done in ZrO_2 grinding bowls with ZrO_2-spheres with 3 mm diameter as grinding medium. For 50 g of calcinated active material 150 ml of ultra pure distilled water and 150 g of grinding spheres were put in the containers. In the case of NMFO again three times the amount was used. Milling was done in a *Pulverisette 5* planetary mill (made by Fritsch, seen in Fig. 4.1 at step IV). „Setting 5" at the mill's potentiometer results in a rotation of 206 rpm and 447 rpm of the planetary disk and the bowl respectively. In accordance with the experience at the institute with the before mentioned similar synthesis of Li-based cathode materials, constant milling for 24 h was performed. To check whether this milling time was reasonable for the Na-based layered oxides as well, the particle size of the milled materials was measured with laser scattering which will be discussed in more detail in Chapter 5.1 *Material properties*. There the milled particles are described as primary particles (PP) of the hierarchical structure. The mill was stopped five times during the milling process and the PP size distribution was measured. The laser scattering data are presented in the appendix. In summary, it can be said that over the entire milling duration the PP size was decreasing, hence justifying the 24 h to achieve a smaller PP size.

With additional ultra pure water the suspension of milled layered oxide PP could be rinsed out of the grinding bowl. The grinding spheres were collected with a coarse sieve. More water was applied to completely clean the spheres and the bowl until the volume of the suspension reached ca. 1.5 L. For the second spray drying (step V) the same parameters as before were used: $T_{in} = 200\,°C$, $T_{out} = 108\,°C$ and the atomizer wheel was set to maximum speed of approx. 32 000 rpm. The suspension was continuously stirred. The produced amounts of cathode material were 35 g at the cyclonic chamber and 11 g at the tower chamber. This shows that some loss (here 4 g) of the milled 50 g occurs as some material sticks to walls, pipes and atomizer of the spray dryer. For step IV and V in the case of NMFO 114 g were used - not three times the amount as before, but more than double. The produced amounts this time were 90 g and 20 g at the cyclonic and tower chamber, respectively. In total, again just 4 g were lost. This indicates that with higher produced amounts in the same order of magnitude no additional loss is to be expected. This is valuable information for the intended upscaling.

4.2.4 Second heat treatment

In terms of upscaling and industrial application, the number of synthesis steps should also be kept to a minimum. However, in the work presented here a second heat treatment (step VI) is necessary, as mentioned before. A clear indication for the necessity of step VI can be seen in the XRD data in Figure 4.3 (Cu-radiation). After step III, reflections belonging to the P2-type phase (upper green hkl-dashes) are clearly visible. In addition
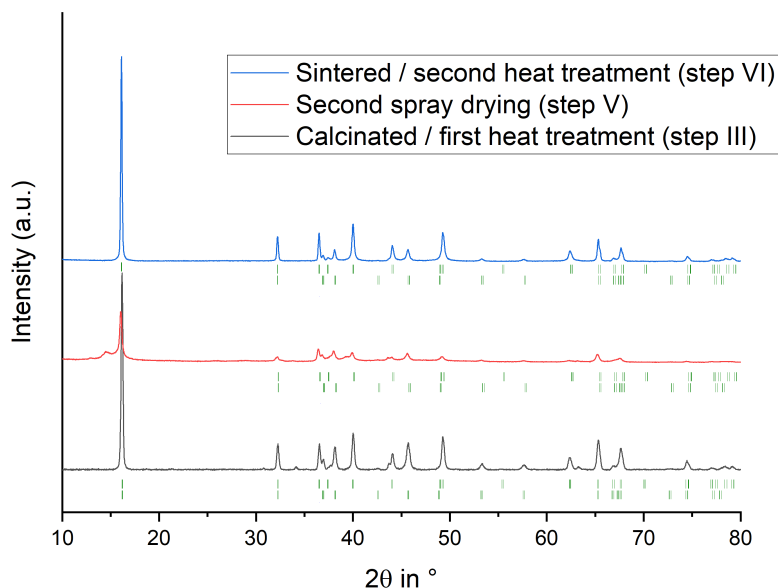
Figure 4.3: **Crystal structure change:** Here X-ray diffractograms at step III, V and VI are shown. Below the diffraction patterns there are two literature patterns indicated by hkl-ticks: The upper line of green hkl-ticks represents reflections positions of the layered oxide phase taken from literature [54]. The lower line of green dashes represents the impurity phase [55].

to that, an impurity phase can be seen (lower green hkl-dashes). The impurity phase can be assigned to $NaMO_2$ (M = Ni, Mn) with the space group $R\bar{3}mH$. A more detailed and quantitative interpretation including Rietveld refinement of XRD data will be presented in Chapter 5.1.4 of the *Results* section. However, a basic understanding of the crystal structure during the synthesis steps was necessary. A simple qualitative interpretation of the patterns in Figure 4.3 is already sufficient. After milling and second spray drying (step IV and V) all reflections have lost intensity and are broadened. Next to the main reflection 002 at ca. 16° an additional broad reflection is visible at ca. 15°. This is most likely due to the milling process. Not only has the size of crystallites decreased but also a large amount of energy from the grinding medium was transferred to the material, possibly damaging the structure. Exposure of layered oxides to air humidity over some time is also known to cause a hydrated phase [56]. Milling in water will have an even stronger effect on the crystal structure. With step VI the desired P2-type phase can be restored: The reflections are even sharper than before and the intensity of impurity reflections (e.g. at 38° and 46°) has decreased.

4.3 Electrochemical Experiments

4.3.1 Electrode preparation

Electrode preparation was done by mixing the cathode powder with an N-Methyl-2-pyrrolidon (NMP) based slurry with polyvinylidene fluoride (PVDF *Kynar Powerflex*

LBG-1, Arkema Inc.) and the conductive carbon *C65* (TIMCAL) in a mass ratio of 80:10:10 in a *SpeedMixer DAC 150* (Hauschild). The mixture was coated on aluminium foil using the doctor blade method, a gap size of 200 μm and 1.5 mm s^{-1} on the device *Coatmaster 510* (Erichsen). Average active material mass loading of prepared cathode sheets was 3.3 mg cm^{-2}. A two-step drying process was used to remove the solvent and moisture by heating the electrode sheet to 80 °C for 30 min (in air on top of the *Coatmaster*) and then to 120 °C under vacuum over night. Further processing of the sheets was done in argon filled gloveboxes. If another step (like calendering) brought the electrodes into air contact again they were vacuum dried again.

4.3.2 Cell assembly

Cathodes with a diameter of 12 mm were punched with a *Handheld punch* (Nogamigiken Co.) and pressed with a force of 5kN in a press tool with 15 mm diameter (calendering). Half-cells were built as coin cells CR2032 with the cathodes, 16 mm diameter glass fibre separator (Whatman GF/C, 260 μm thickness), a 12 mm sodium metal anode and 100 μL electrolyte. To prepare the electrolyte NaPF$_6$ was vacuum dried over night at 120 °C and stirred to a 1M solution with Propylene Carbonate (PC) and 5 % Fluoroethylene carbonate (FEC).

4.3.3 Galvanostatic Cycling

Galvanostatic cycling with potential limitation was performed on an *Arbin* potentiostat in the electrochemical window of 1.5 V to 4.0 V / 4.3 V / 4.6 V vs. Na$^+$/Na. The current of 1C for cycling was defined in accordance with Hasa et al. [36] based on 0.6 Na within the pristine structure (same value for the four different compositions in Fig. 3.1), which yields the follwoing currents: I(NANMO) = 164 mA g^{-1}, I(NANMFO) = 165 mA g^{-1}, I(NAFMO) = 165 mA g^{-1} and I(NMFO) = 159 mA g^{-1}. One needs to take into account that additional sodium from the metal anode can add more capacity if cycled below the open circuit voltage. At the beginning of an electrochemical cycling a formation cycle with 1C was performed. The reason for this is a pragmatic handling of the sometimes problematic and not yet commercially available electrolyte (own production), which is also a topic of current research [57]. A preceding 1C cycle increased the success rate of the cells. Long-time cycling with identical electrolyte and electrodes showed no difference in behaviour after 200 cycles with or without 1C at the beginning.

4.3.4 Impedance

Electrochemical impedance spectroscopy (EIS) was performed not on the half-cells but on pure cathodic material without any binder or conductive carbon. To do so the powders obtained in the second spray drying process (step V in Fig. 4.1) were pressed into pellets with a *PW10* manual laboratory press with a force of 20 kN and a press tool with a diameter of 12 mm. The resulting thickness, depending on the used powder and the amount, ranged between 0.9 mm to 1.2 mm and was taken into account. As sintering temperature 950 °C was chosen as it is one of the same temperatures used for

the cathode preparation. The sintered pellets were dry-smoothened with sand paper (grit size 1000) and sputtered with gold on both sides. To improve connection in deep pores, silver ink was added to both sides on top. Vacuum drying at 120 °C was done to remove moisture and the pellets were locked into swagelok cells under argon atmosphere. For the EIS measurement a *VSP-300* (BioLogic) potentiostat was used with 50mV amplitude in the range from 7 MHz to 10 mHz. The cells were kept in a *BTZ-175* (ESPECS) climate chamber. Temperature was set in 5 °C steps to values between −50 °C to 60 °C. Before measurement a waiting time of 0.5 h to 1 h was needed, until the temperature chamber was stable and another waiting period of 1h was incorporated to make sure that the swagelok cells had adopted the temperature. The data were investigated with the software *Relaxis 3 (Rhd Instruments)*

4.3.5 In situ analysis

For in situ X-ray diffraction a laboratory diffractometer for battery research with Mo-$K_{\alpha_{1/2}}$ radiation was used and data was collected for the 2θ range of 5° to 32°. To increase the intensity, thicker cathodes were prepared in the same way as described before but with a gap size at the doctor blade of 400µm, which resulted in a mass loading of 8.0 mg cm^{-1} to 9.5 mg cm^{-1}. Coin cells with silicon windows were prepared and after a formation cycle with 1C (analogue to galvanostatic cycling) the current during XRD measurement was C/10. As a compromise between good intensity-noise-ratio and continuous scanning during cycling one scan was done in 150 s and four scans summed to one picture giving a measurement time of 600 s. Rietveld refinement was executed with the Software *Topas Academic V6 (Bruker AXS)*, *jEdit* and *FullProf*.

(a)

(b)
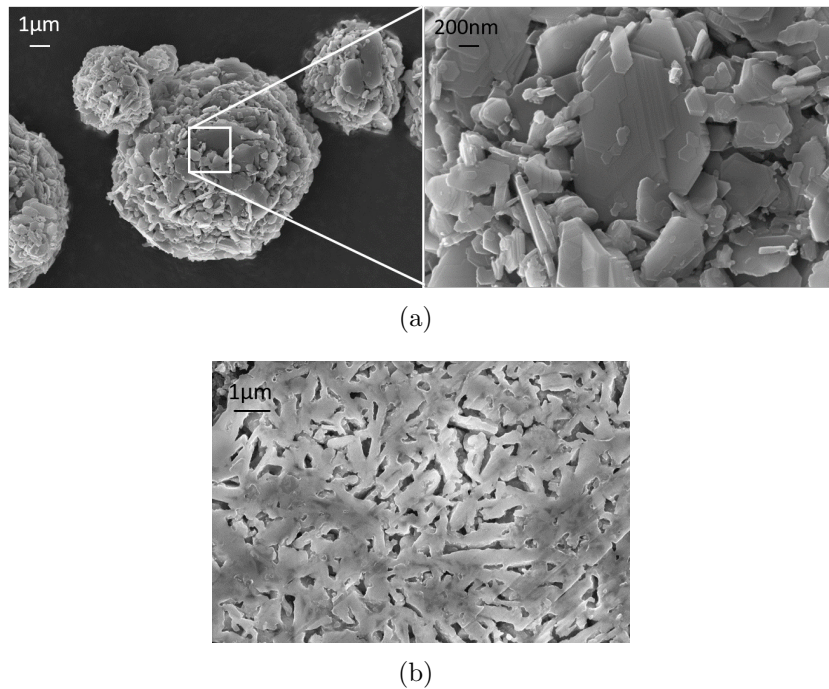
Figure 5.1: **Hierarchical structure:** SEM pictures of a spherical particle made from a P2-layered oxide material (NANMO after 950 °C). On closer inspection of (a) it can be seen that the big spherical particles consist of small flake-like particles. A cross section of a spherical particle is show in (b).

5   Results and discussion

The investigation started with the material $Na_{0.6}Al_{0.11}Ni_{0.22}Mn_{0.66}O_2$ (NANMO) presented by Hasa et al. [36]. To the best of our knowledge this is the first time that this material was synthesized with the process presented here, especially the spray drying step is uncommon but promising. Therefore it was first necessary to control if the material had received a hierarchical structure as it was anticipated. Powder in its final state after the second heat treatment was investigated with scanning electron microscopy (SEM) as well as a cross section of the particles to reveal its morphology. In Fig 5.1 some spherical secondary particle with different sizes and diameters of several micrometers are shown as a typical product of the spray drying process. It can be seen that these spheres are built up from many small, flake-like secondary particles with sizes in the submicrometer range (Fig. 5.1 (a)). A cross section of a secondary particle (b) shows the porous nature of these spheres.

This shows that with our approach a hierarchical structure was successfully created. The flake-like morphology of NANMO primary particles might be related to its crystal structure. One can vaguely see the layered nature with a hexagonal crystal system. Compared to a Lithium-NMC (Nickel-Manganese-Cobalt) material prepared with a sim-

ilar spray drying process from Wagner et al. [5] a few differences can be seen. The NMC primary particles are small and resemble sand grains while their secondary particles are more round as compared to NANMO. The most distinct difference between the achieved morphology of Wagner et al. and the NANMO morphology presented here is the primary particle shape. One reason for that is the use of an agitator bead mill for NMC with $0.2\,mm$ ZrO_2 beads at higher speed which resulted in smaller particles. The other reason is the chemical composition itself which has an influence on the sintering behaviour and therefore shapes the primary particles in a different way. Evidence for that can be found in the following text where the four different P2-type sodium transition metal layered oxides (Fig. 3.1) are compared and shown to have a different morphology even though their synthesis process was identical.

5.1 Material properties

Here it is presented how the particle morphology changes during the process steps. The ground suspension contains fine, colloidal nano particle called primary particles (PP) in this thesis. During spray drying they cluster together to the bigger, spherical secondary particles (SP) with a certain porosity Φ and specific surface area A_{BET} (according to the Brunauer-Emmet-Teller method). Both of these properties change during heat treatment.

The heat treatment brings up the next fundamental material property: The crystal structure which will be analysed thereafter by x-ray diffraction. The heat treatment also marks the final step in the preparation and presents the materials in their pristine state before electrochemical cycling. For that reason the analysis of the chemical composition was also measured past heat treatment.

It was also of interest to investigate the pristine, iron containing materials with Mößbauer spectroscopy to measure the amount of iron in oxidation state Fe^{3+}. In this context Mößbauer spectra of the charged, iron containing materials is already presented to give an impression on the oxidation to Fe^{4+}. This is foreshadowing their electrochemical behaviour which will be discussed later in Chapter 5.4 *Electrochemistry*.

5.1.1 Particle morphology

The primary particle size distribution was measured after the grinding process (step IV in Fig. 4.1 in Chap. 4.2). Small drops were taken from the aqueous suspension of ground material and measured with laser scattering. Ultrasound was applied to reduce agglomeration. Particle sizes were similar for the four chemical compositions with a distribution between $0.2\,\mu m$ to $10\,\mu m$ and a typical maximum at around $1\,\mu m$. The average particle size differs from highest nickel content to highest iron content from $1.67\,\mu m$, $1.65\,\mu m$, $1.42\,\mu m$ to $1.11\,\mu m$ for NANMO, NANMFO, NAFMO and NMFO respectively (see Appendix). This can be interpreted as the PP size of the later formed SP which can be observed at the spray dried powders. The change in its sizes seems to originate from the chemical composition since all materials underwent the same grinding process. This might impact the final morphology of the secondary particles as well, but one needs to

Table 5.1: **SP sizes:** Overview of the mean SP sizes at different stages of the synthesis. The ultrasound was only applied for the size measurement during laser diffraction.

SP size in µm	**NANMO**	**NANMFO**	**NAFMO**	**NMFO**
spray dried	11.2	11.9	11.9	10.8
sintered before Ultrasound	10.7	10.9	11.5	15
sintered after Ultrasound	8.2	7.4	9.2	13.8

take into account that the second heat treatment causes the PP to sinter and thereby change their sizes which can then be estimated from the SEM pictures. Different degrees of grinding of the primary particles were tested for NANMO only in the early stage of this work. The morphology of the resulting primary and secondary particles is presented in the appendix in chapter 7.3. The electrochemical performance of these differently ground materials can also be found in the appendix in chapter 7.4.1.

Laser scattering was also performed to measure the secondary particle size. After both steps, V (second spray drying) and VI (second heat treatment) of the synthesis process (see Fig. 4.1 in Chap. 4.2) the four different materials were sieved with 32 µm mesh size to remove small amounts of bigger particles. Laser scattering resulted in different values for the four different materials.
A distribution of the sizes of secondary particles was expected and measured. The distributions cover a range from ca. 3 µm to 30 µm for all materials. The calculated mean values for secondary particle sizes are summarized in table 5.1. After the spray drying process (step V) the four different materials show quite similar SP sizes. Only for NMFO the average value is slightly smaller than for the other three. The SP size is determined during the spray drying process and depends on the inlet temperature at the atomizer and the speed of the atomizer wheel. One would expect to receive the same SP size for all materials since the spray dryer and the adjusted parameters were the same. This appears to be the case. Slightly smaller NMFO particles could be a result of the before mentioned smaller PP, which were a result of the grinding.

When measuring the size distribution of the sintered SP (after step VI) one needs to understand that during the sintering process not only primary particles (PP) but also neighbouring SP can be sintered together and might still fit through the finest sieve of 32 µm. To reduce this agglomeration ultrasound can be applied during the laser scattering. While it can be assumed that sintered SP are more mechanically stable since the PP create stronger connections one must still consider that some SP will break due to ultrasound. This gives us two particle size distributions, both with some uncertainties: Before ultrasound (uncertainty: Agglomeration) and after ultrasound (uncertainty: breaking SP). Table 5.1 shows the average values of SP-size measured after the step VI with the sintering temperature $T_s = 950\,°C$. In the appendix the curves of particle size

Table 5.2: **Densities of active materials:** Calculations from Rietveld refinement of cathode material sintered at $T_s = 950\,°C$ resulted the densities of the layered oxides.

	NANMO	**NANMFO**	**NAFMO**	**NMFO**
ρ in g/cm^3	3.83	4.08	4.02	4.10

distribution are plotted and the corresponding data is presented in tables (see Chap. 7.1.2). It can be seen that the values differ moderately for the four different compositions. Applying ultrasound reduces the mean size slightly. This suggests little SP agglomeration and little SP breaking. NMFO differs in this comparison from the other three materials: After sintering the average size is considerably larger than before and applying ultrasound could not restore the original size which was measured after spray drying. This tells us that in case of NMFO it is more likely that the SP sinter together and these sinter connections are difficult to break. A similar behaviour can be observed throughout the presented investigations of the particle morphology in this chapter and the following two. At several points in the results discussion an increasing sinter activity can be attributed to an increasing iron content. NMFO exhibits the highest iron content of the presented materials.

For a particular and quantitative analysis of the particle morphology the porosity Φ and specific surface area A_{BET} were measured before and after the final heat treatment to understand what part of the hierarchical structure is determined by spray drying and how the sintering process influences that. SEM pictures were again taken to visualize this aspect qualitatively.

For the measured Hg-porosimetry data a density was needed to calculate a specific porosity value Φ. Therefore densities ρ were determined via Rietveld refinement of the sintered materials and are summarized in Table 5.2.

Figure 5.2 gives an overview about the particle morphology. From (a) - (d) SEM images of different cathode active materials (CAM) and values for the specific surface area A_{BET} and porosity Φ are shown. For every material there are two images on the left after step V (spray drying) and two on the right after step VI (950 °C) of the synthesis process. The different magnifications (top and bottom) show different aspects of the morpholgy. This visualizes how the hierarchical structure has evolved for each material in a sintering process at 950 °C (step VI). The sintering temperature 950 °C was not chosen for a particular reason. It was the first to be investigated and is one of the central temperatures in the range from 850 °C to 1000 °C. The visual morphology is likely to change with the different temperatures presented later as well, but it can be assumed that the most significant change of a particle's surface is visible when comparing a spray dried (step V) and sintered (step VI) sample. Though different surface roughness might be visible in SEM pictures at different sintering temperatures, but a more plain interpretation can be extracted from a comparison of porosity and A_{BET} data. This data is shown in Table

(a)   (b)

(c)   (d)
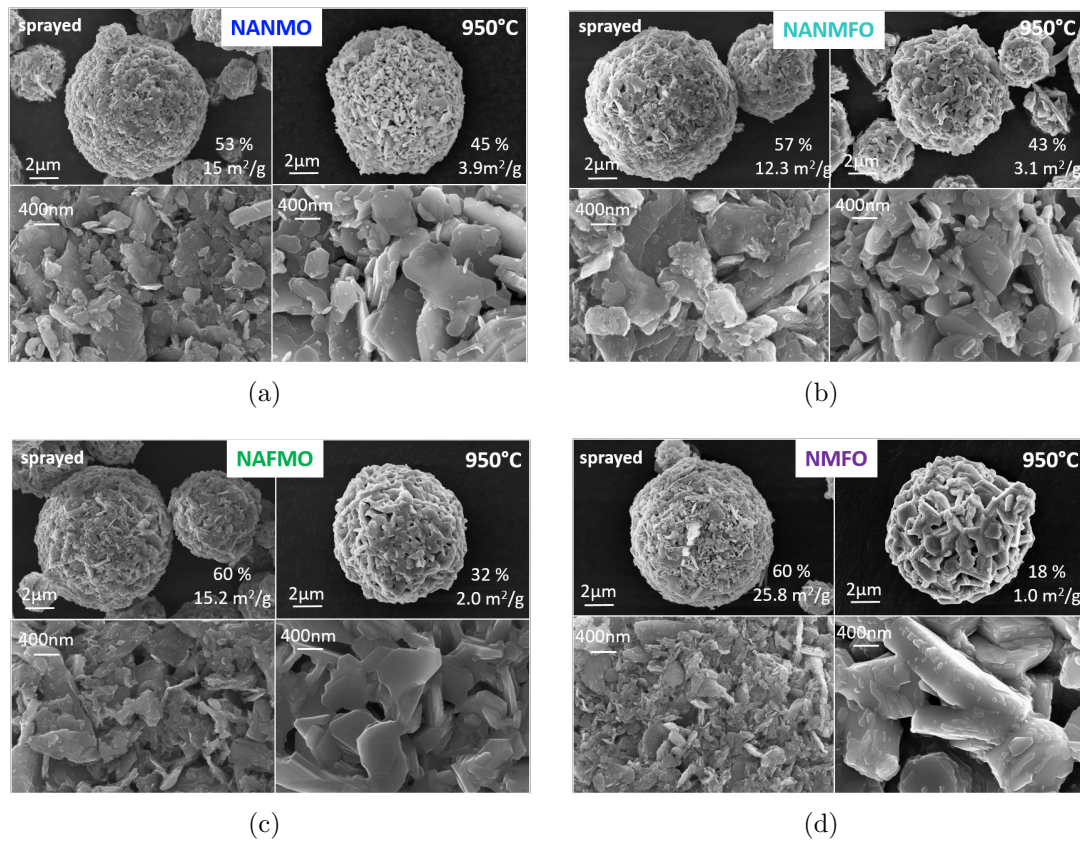
Figure 5.2: **Material overview:** SEM micrographs and corresponding values for porosity and specific surface area for the four materials (a) - (d). Each material is displayed before (left) and after (right) sintering with 950 °C.

5.3 and will be discussed later in Chapter 5.1.3 *Tuning morphology via sintering temperature.*

The SEM pictures in Figure 5.2 were taken for each material and both steps with magnifications of $5 \cdot 10^3$ (2 µm scale) and $25 \cdot 10^3$ (400 nm scale) to show a complete SP and detailed view of the PP on its surface.

Several spherical SP of different sizes (size distribution) can be seen after step V (spray dried). From high nickel content (blue) to highest iron content (purple) the PP appear to get finer. Especially NMFO shows a much higher BET-surface. The porosity is increasing with the iron content but for NAFMO (green) and NMFO (purple) the same value was obtained.

An interpretation of that is, that with higher iron content finer PP sizes can be achieved under the same grinding conditions. It was evident before when comparing the average PP size after grinding above where NMFO had considerably smaller PP sizes. This is the reason for the increased A_{BET}. It is not clear why the porosity of spray dried SP of NAFMO and NMFO is higher, since one would expect that finer particles can be packed more densely together. However, it also needs to be noted that a SP at this point of the

synthesis (after step V, before sintering) is not yet completely stable and the PP just stick loosely together.

Figure 5.2 shows how these properties have evolved after a sintering process (second heat treatment) with 950 °C and a duration of 6 h in air. The same SEM magnifications as before are shown along with the corresponding values for porosity and BET surface. It can be seen in both pictures and values, that there has been a sintering process which has reduced the surface roughness of the PP. They have turned into flake-like shapes with smoother surfaces. These flakes give the SP a somewhat spiky appearance. When moving from highest nickel content to highest iron content ((a) to (d)) a change in the morphology is notable: The length and thickness of the PP flakes are increasing. This is supported by the specific surface area which has become much smaller than before due to sintering and is decreasing from (a) to (d). The porosity is following this trend. Under the same conditions the nickel containing materials (NANMO & NANMFO) strongly differ from the iron rich materials (NAFMO & NMFO). While NANMO and NANMFO maintain a relatively high value of their porosity (53 % to 45 % and 57 % to 43 % respectively) the porosity of NAFMO and NMFO drops from about 60 % to 32 % and 18 % respectively.

In case of NMFO this apparently strong sinter activity can be explained by the much higher BET value which allows more surface for particles to merge together. But this cannot be the only origin for the strong sinter activity, since prior to the sintering step a similar A_{BET} was measured for both NANMO and NAFMO of about $15 \, \text{m}^2 \, \text{g}^{-1}$. Still it is visible that the porosity and specific surface area has decreased for NAFMO much more than for NANMO. We suppose that with higher iron content a stronger sintering is happening in general. Saitou et al. [58] were investigating the sintering behaviour of pellets made from pure metal powders. If these results can simply be translated to the sinter activity of layered oxides is unclear. However what they found is a lower activation energy of the shrinkage parameter of iron pellets as compared to nickel [58].

The sintering activity depending on the iron content can be supported with dilatometry. Figure 5.3 (a) shows in different colours how the length change of pressed pellet with pure cathode material is propagating with increased temperature. For that the shrinkage parameter $\frac{\Delta L}{L_0}$ is compared. According to Saitou et al. [58] the shrinkage parameter can be calculated as the ratio of the original length L_0 and the change of the length ΔL. For T < 250 °C a small drop of $\frac{\Delta L}{L_0}$ is visible. The reason for that is not clear. Perphas the powders did accumulate air moisture during storage, which caused this offset. It can be seen that it is similar for the pairs of nickel containing materials (NANMO & NANMFO) and nickel free materials (NAFMO & NMFO). These pairs also exhibit similar porosities. However, the significant part is located in the range from 400 °C to 1100 °C. It can be seen that with increasing iron content (NANMO, NANMFO, NAFMO, NMFO) the length change becomes more distinctive. In case of NANMFO this only happens rather late at a temperature of ca. 970 °C. This might be due to the offset at the beginning of the measurement, which is different for the materials. But it can be seen that the slope of the curves is getting steeper with increasing iron content. A more quantitative analysis of that is presented in (b) with the time derivation of the $\frac{\Delta L}{L_0}$ curves, which represents

(a)   (b)
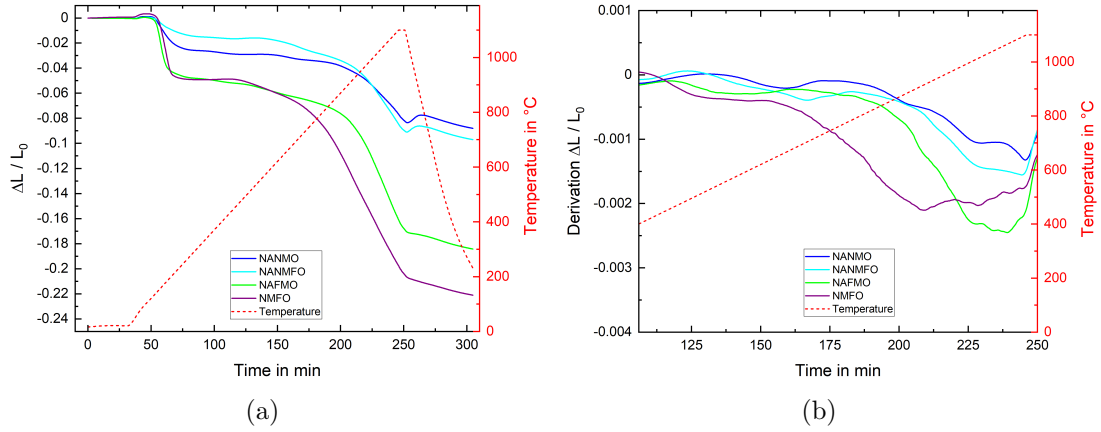
Figure 5.3: **Dilatometry:** In (a) the shrinkage parameter $\frac{\Delta L}{L_0}$ is plotted over the time of measurement. The temperature (dotted line) is increased from room temperature to 1100 °C with a rate of 5 K/min. (b) shows the first time derivation of the shrinkage parameter in the section from 400 °C to 1100 °C.

the gradient of the dilatometry curves. For most temperatures the gradient is increasing with the iron content, only in the end of at approx. 960 °C NAFMO exhibits a higher value than NMFO. However it needs to be noted that in order to scan over a certain range of temperatures no dwell time at a specific sintering temperature was implicated in this dilatometry measurement. In case of the sintering of the cathode materials a dwell time of 6 hours was used.

At this point we can refer to another experiment with sintering of pellets and the same dwell time of 6 h from chapter 5.2. This data is about impedance measurement on sintered cathode materials and will be presented later in Chap. 5.2 but we can already refer to the sinter behaviour. For the four different layered oxides pellets with a diameter of 12 mm were pressed with 20 kN and sintered at 950 °C for 6 h, analogous to the powder samples shown above. Listed from highest nickel content to highest iron content the shrinkage parameters result in $2.32 \cdot 10^{-2}$, $3.06 \cdot 10^{-2}$, $5.52 \cdot 10^{-2}$ and $7.28 \cdot 10^{-2}$ for NANMO, NANMFO, NAFMO and NMFO respectively.

This supports the previously proposed idea that high iron content (NAFMO and NMFO) results in more sinter activity, while NANMFO and NANMO have similar shrinkage parameters and their powders show similar high values for porosity and A_{BET}.

5.1.2 Cathode morphology

The understanding of the SP morphology sintered at 950 °C presented before will be complemented here by the morphology of cathodes created from the same material (sintering at 950 °C). The electrode sheets were prepared in the ratio of 80/10/10 (active material/binder/conductive carbon) as described in Chapter 4.3 of the *Experimental* section. In addition to the SEM images of the spherical SP from Figure 5.2 there are images of electrode cross sections shown. These reveals two more properties: The in-

29
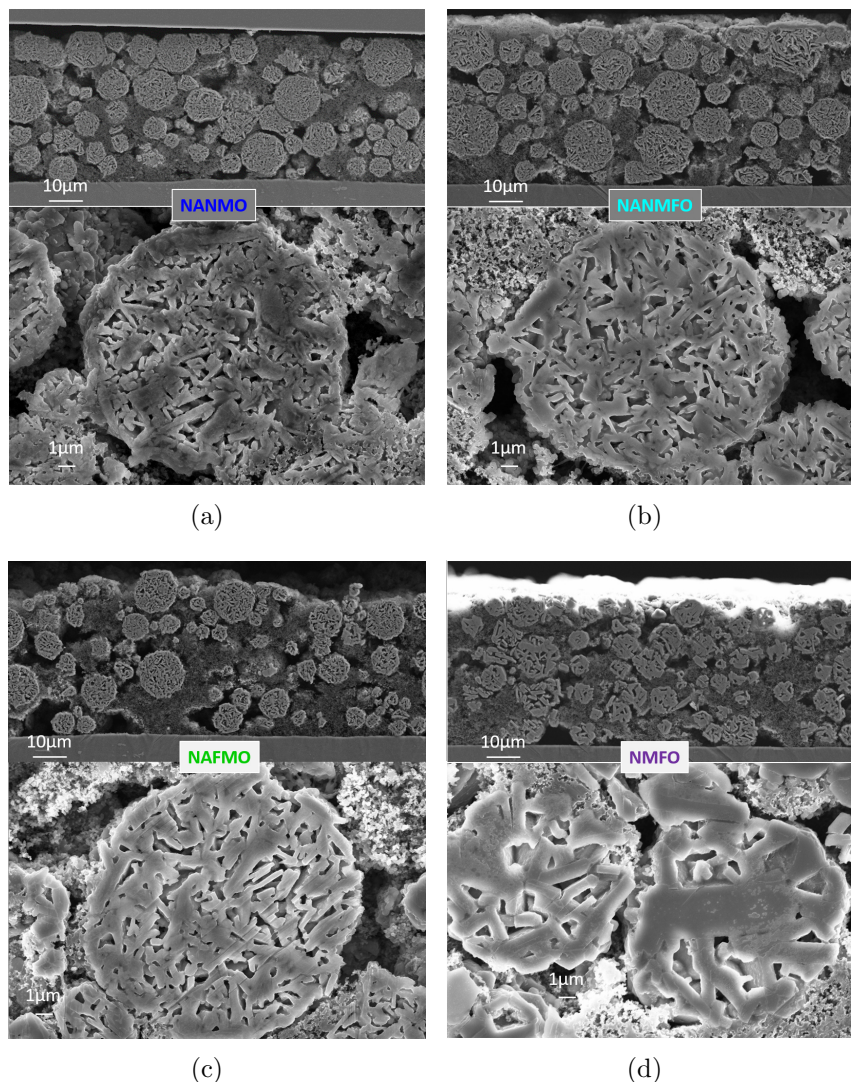
Figure 5.4: **Electrode cross section:** Overview of the homogeneity and internal pore structure of the four layered oxides (a)-(d). For NANMO in (a) $\Phi = 45\,\%$, for NANMFO in (b) $\Phi = 43\,\%$, for NAFMO in (c) $\Phi = 32\,\%$ and for NMFO in (d) $\Phi = 18\,\%$.

ternal structure of a secondary particle and how the particles in a electrode sheet are distributed with the performed preparation. The cross sections were prepared with an ion-etching device. This allows a smooth surface of the cross section without damaging the particle morphology. Figure 5.4 shows for each material ((a) - (d)) two magnifications of these cross sections. The top images show each a wide range of the electrodes with many spherical secondary particles of different sizes. The size distribution of the SPs for the four active materials was discussed before (see Tab. 5.1). A flat gray surface can be seen at the lower part of these wide range images. It is the cross section of the aluminium foil which acts as the current collector of the electrode. Between the active

<div align="center">(a)   (b)</div>
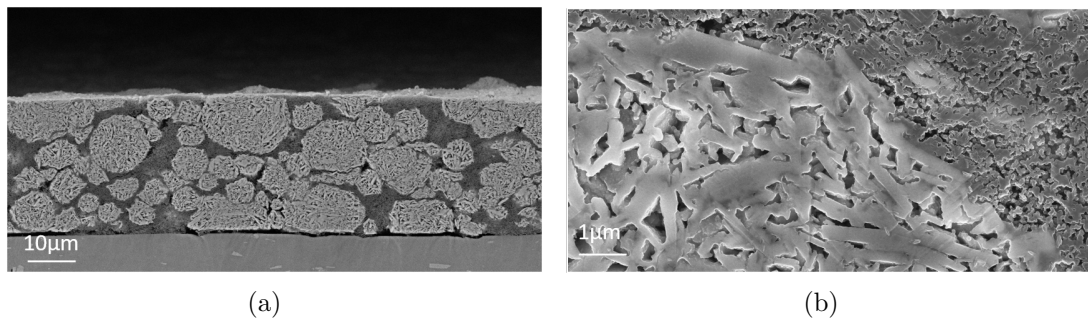
Figure 5.5: **Calendering:** Cross section of a calendared NANMO cathode. (a) Overview of particle deformation and (b) close-up of pore structure of active material and binder-carbon-matrix.

material particles there is a matrix of binder and conductive carbon for stabilizing and connecting the particles to each other and the current collector. At higher magnification (bottom picture of each (a)-(d)) the inner porosity of the SPs can be seen. The flake-like shape of primary particles on the surfaces described before continues into the insides of the secondary particles. With higher magnification it is also visible that the binder-carbon-matrix shows a certain degree of porosity as well.

The active material inside the cathodes is for the most part homogeneous distributed. Some smaller particles fill holes between bigger ones and sometimes small areas with no particles are seen. An optimization slurries and of electrode sheet coating might bring further improvements to this matter. The cross sections of the single particles allow a visual evaluation of the measured porosity data. As a reminder from the previous section the measured porosity of each CAM is given in the caption of Figure 5.4. NANMO (a) and NANMFO (b) almost exhibit the same porosity and therefore also look quite similar. The pore structure of both resembles each other. In case of NAFMO (c) the lesser porosity is also recognizable in the SEM images. That NMFO (d) shows the lowest porosity of the four CAMs can at once be verified visually when comparing the cross sections: Between the pores there are relatively thick walls of primary particles. In case of NANMO, NANMFO and NAFMO it can be seen that the SP exhibit a slightly thicker wall on the outside. This can be seen for many spray dried materials. For NMFO it is difficult to see, since the primary particles in general have a bigger size

For NAFMO in Figure 5.4 (c) it can also be seen, that sometimes big pores inside the binder-carbon-matrix form. The reason for that might be that the electrode sheets presented here are produced on the laboratory scale, which means they cover rather small areas (e.g. 7x20 cm). On an industrial scale the electrode sheets are in general coated in a continuous procedure on foils revolving over a system of rolls [59] and therefore showing quite uniform sheets. The big pores in the electrode sheet might indicated that this particular electrode was punched at the end of the electrode sheet. It is unlikely that NAFMO exhibits another material property leading to holes in electrode

sheet. The point however is, that big holes between the CAM particles and the binder-carbon-matrix can reduce the overall capacity and rate-capability of a battery. Active material without an electrical contact to the current collector cannot contribute to the capacity and is literally dead weight. If the contact to the current collector is existing but too small then big currents at high C-rates would deliver smaller capacities [60]. Compressing the electrode sheet to a certain degree will improve these two electrochemical properties [60, 61]. The industrial compressing is done with calenders and therefore called calendering. This was imitated by pressing on the electrodes with a specific force, increasing both capacity and rate capability and creating overall more reproducibility by uniform cathodes. Figure 5.5 shows an ion-etched NANMO cathode calendered with $5\,kN$ per $1.13\,cm^2$ (see Chap. 4.3). (a) gives an overview of the shape change of the secondary particles. Some of them have maintained the spherical shape, others have been deformed strongly. However, it can also be seen that the particles did not break and no cracks have been formed. This is valuable information for future work regarding calendering tests with hierarchically structured particles. The binder-carbon-matrix has been compressed and fills out the empty space between the active material. Big holes as observed before are not visible. In (b) a higher magnification shows, that the porosity of both particle and matrix is still intact, hence allowing electrolyte penetration.

5.1.3 Tuning morphology via sintering temperature

With the presented data from Chapter 5.1.1 before, one can understand that the final morphology of the powders depends strongly on the chemical composition and not on processing only. The latter was investigated in the following to tune porosity and specific surface area for the different layered oxides.

Table 5.3 gives an overview about the four materials and their porosity Φ and specific surface area A_{BET}. Listed are values similar like before after spray drying and after different sintering temperatures. Overall it can be seen that Φ and A_{BET} decrease with increasing sintering temperature. The BET surface area changes strongly when comparing step V (spray dried) with even the lowest sintering temperature. This is in agreement with the expectation. The high surface area arises from the milling process (step IV) of the primary particles. These fine milled high-surface PPs are packed together into the secondary particles and a lot of surface can quickly sinter together. Interesting is how the BET surface and the porosity are evolving with the different sinter temperatures. In this context the previous mentioned assumption is supported again: Particles with a higher iron content show a stronger sinter activity: While $Na_{0.6}Al_{0.11}Ni_{0.22}Mn_{0.66}O_2$ (NANMO) only shows a moderate change in its porosity from $53\,\%$ to $42\,\%$ over the investigated temperature range there is already more change visible for $Na_{0.6}Al_{0.11}Ni_{0.11}Fe_{0.11}Mn_{0.66}O_2$ (NANMFO) from $57\,\%$ to $42\,\%$. Also A_{BET} is reduced to smaller values with increasing temperature in case of NANMFO. Still these materials display quite similar morphological properties, caused by the similar composition of NANMO and NANMFO.
A stronger sintering temperature dependence of the morphology is visible when all nickel is removed and the iron content is raised further to $Na_{0.6}Al_{0.11}Fe_{0.22}Mn_{0.66}O_2$ (NAFMO).

Table 5.3: **SP morphology:** Porosity Φ and specific surface area A_{BET} for all four layered oxides after the final spray drying process and several sintering temperatures.

	NANMO	NANMFO	NAFMO	NMFO
spray dried				
Φ in %	53	57	60	60
A_{BET} in m^2/g	15.0	12.3	15.2	25.8
850°C				
Φ in %	51-53 [01]	52	48	39
A_{BET} in m^2/g	5.9	4.4	4.3	2.5
900°C				
Φ in %	51	47	43	28
A_{BET} in m^2/g	4.7	3.5	4.0	1.5
950°C				
Φ in %	45	43	32	18
A_{BET} in m^2/g	3.9	3.1	2.0	1.0
1000°C				
Φ in %	42	42	22	12
A_{BET} in m^2/g	2.8	2.2	1.5	0.7

The stronger sinter activity causes more dense secondary particles with less porosity. The same is true for $Na_{0.6}Fe_{1/3}Mn_{2/3}O_2$ (NMFO). For NMFO a higher A_{BET} of the spray dried particles as compared to the other is likely an additional reason for the even stronger sintering behaviour.

The influence of different morphologies on the electrochemical behaviour is compared and analysed in Chap. 5.4.

5.1.4 Crystal structure

The structural properties of the different materials were characterized through X-ray diffraction. In Figure 5.6 several diffractogramms of the four layered oxides after a heat treatment of 950 °C are shown. In the case of the NANMO material some impurity reflections (*) can be observed which can be denoted to a compound of $NaMO_2$ (M = Ni, Mn) with the space group $R\bar{3}mH$ [55]. While for NANMO some impurity reflections are visible clearly, they fade and almost vanish with NANMFO. NAFMO displays no

---

[01] Due to malfunctions of the porosimeter the measurement failed several times. Since it turned out, that the electrochemical performance of NANMO sintered by 850 °C was quite poor this value was not of much interest (see Chap. 5.4 *Electrochemistry*). The only interest would be to complete Table 5.3. But since Φ for spray dried NANMO and sintered at 900 °C are very close anyway, the porosity can be sufficiently narrowed down to 51 % to 53 %.
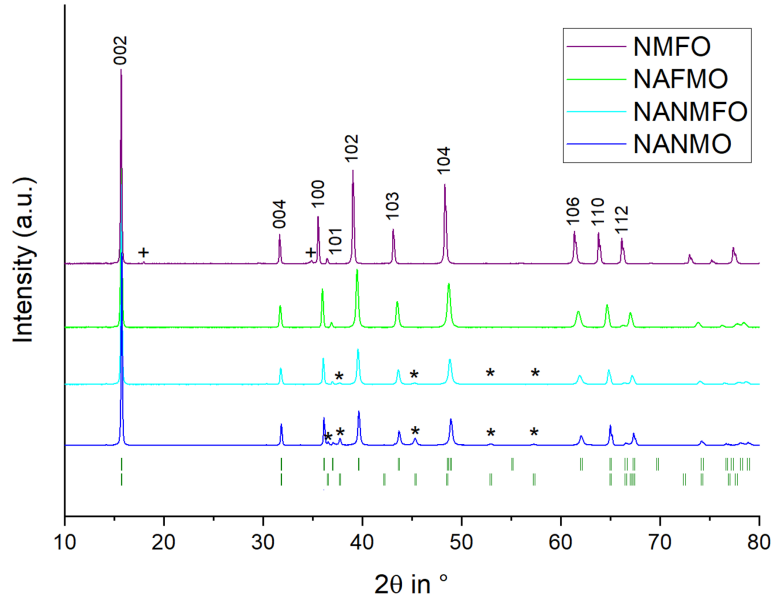
Figure 5.6: **X-ray diffraction:** Investigation of the P2-type layered crystal structure of the cathode materials. Measurements were taken at room temperature after the second heat treatment with 950 °C. The upper line of green dashes represents reflection positions from literature [54] of the P2-type layered oxide phase. Impurity phases are marked with + and * symbols. The lower line of green dashes represents the trigonal impurity * phase $NaMO_2$ (M = Ni, Mn) ($R\bar{3}mH$) [55]. A spinel phase of $Fe_2Mn_1O_4$ [62] is corresponding to the impurity marked with +, which is only present in case of NMFO.

impurity reflections at all while for NMFO two tiny reflections of an unknown impurity phase are visible (+). Later in Fig. 5.7 the evolution and vanishing of the impurity phase is shown and discussed. When the main reflections 002 of the four different materials are scaled to the same intensity (different intensities might arise from slightly thicker or thinner preparation of powder) the intensities can be compared better. It can be seen that the intensity ratio between main reflection and reflections of higher angles (beyond 30 °) is different for the four materials. From lowest to highest iron content (NANMO to NMFO) the intensity of higher angle reflections are increasing relatively to 002. It can also be observed that the reflections are getting thinner and sharper.

For all materials it is visible that the P2-type layered oxide crystal structure was formed [63]. The reflection positions can be compared to the green dashes underneath the diffractogramms where literature reflection positions are marked (see: [54]). The P2-type layered oxides crystallized in the hexagonal crystal system with the space group $P6_3/mmc$ and a characteristic main reflection 002 which shows the highest intensity. Reflections with more intensity and sharper shape generated from materials with higher iron content support the understanding of the different sintering behaviour formerly observed in Chap. 5.1.1. Their higher iron content resulted in a stronger sintering behaviour. This appears to be related to the formation of the crystal structure as well,

Table 5.4: **Structural parameters:** Rietveld refinement was done for the four chemical compositions NANMO, NANMFO, NAFMO and NMFO. All were sintered with $T_S = 950\,°C$. The corresponding XRD patterns are shown in Fig. 5.6. Refined lattice parameters a and c are given in Å. Additionally the occupancies of the two sodium sites Na_1 and Na_2 were calculated.

NANMO	Lattice	a= 2.8684 Å	c =11.2367 Å			
	Atom	Wyckoff	x	y	z	Occupancy
	Na_f	2b	0	0	1/4	0.253
	Na_e	2d	1/3	2/3	3/4	0.347
	O	4f	1/3	2/3	0.0916	1
NANMFO	Lattice	a=2.8747 Å	c =11.2587 Å			
	Atom	Wyckoff	x	y	z	Occupancy
	Na_f	2b	0	0	1/4	0.244
	Na_e	2d	1/3	2/3	3/4	0.356
	O	4f	1/3	2/3	0.0915	1
NAFMO	Lattice	a=2.8829 Å	c =11.2843 Å			
	Atom	Wyckoff	x	y	z	Occupancy
	Na_f	2b	0	0	1/4	0.216
	Na_e	2d	1/3	2/3	3/4	0.384
	O	4f	1/3	2/3	0.0975	1
NMFO	Lattice	a=2.9163 Å	c = 11.2982 Å			
	Atom	Wyckoff	x	y	z	Occupancy
	Na_f	2b	0	0	1/4	0.219
	Na_e	2d	1/3	2/3	3/4	0.381
	O	4f	1/3	2/3	0.1025	1

which would make sense if the origin is indeed a higher diffusivity of iron. In that case one would expect crystallites to grow faster and bigger. The measured reflections which are sharper and display higher intensity as a function of iron content support this assumption.

Rietveld refinement was done with the software *Topas* to determine specific structural information. The plots of measured and calculated XRD patterns are shown in the appendix. The refined values were the lattice parameters a (=b) & c and the occupancy of the two possible sodium sites Na_1 & Na_2. The results of the four different materials (sintered with $T_S = 950\,°C$) are shown in Table 5.4. Lattice parameter a gives information about the distance of transition metals inside the layers while parameter c gives information about the distance between neighbouring layers. These values are in accor-
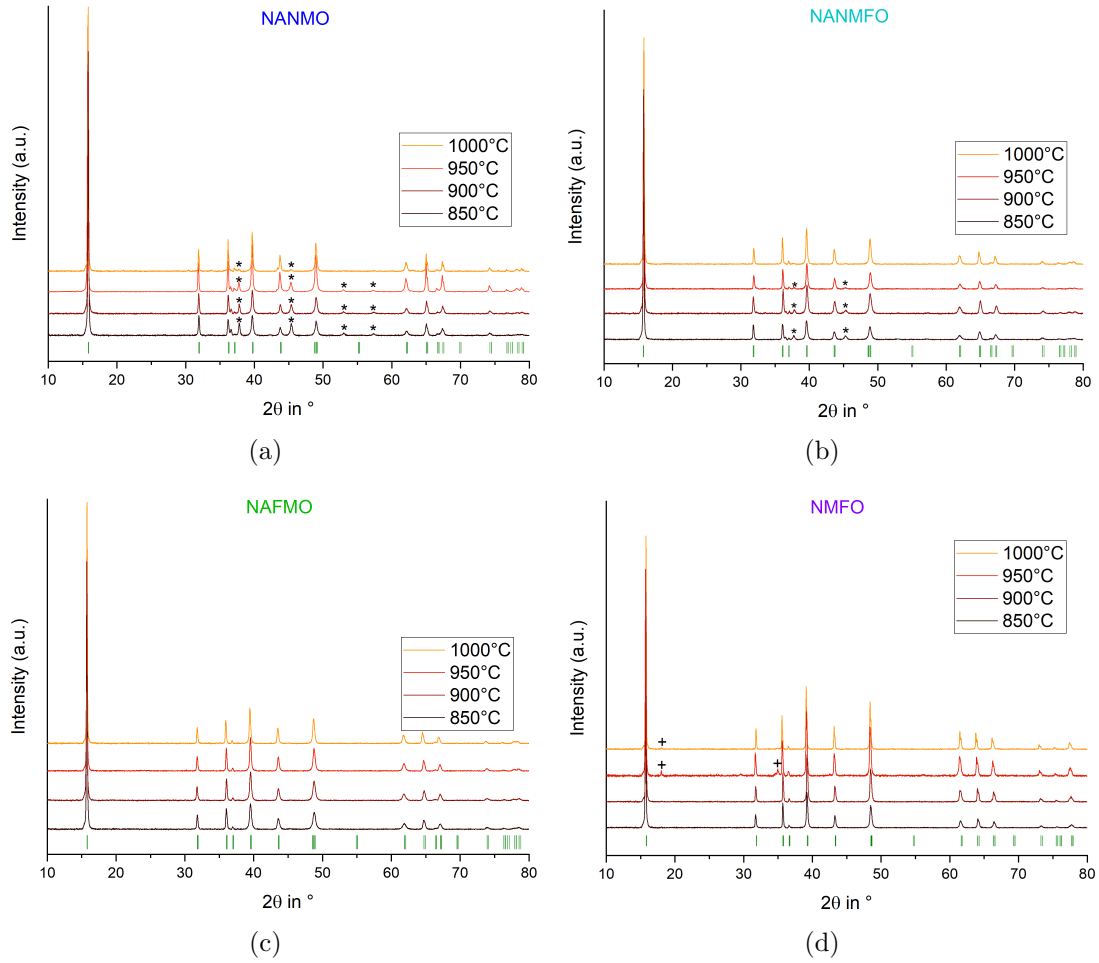
Figure 5.7: **Sintering temperature dependence of crystal structure:** Displayed is how the diffractorgramms evolve within the sintering temperature range from 850 °C to 1000 °C (ex situ measurement taken at room temperature). Separated in the four tiles are the different chemical compositions. The impurity phases + and * are marked analogous to Fig. 5.6, as well as the Bragg positions of a P2-type structure [54] which are indicated with green hkl-ticks.

dance with the literature, e.g. for NMFO Zhao et al. [64] or for NANMO Hasa et al. [35] where the same cathode materials were investigated. The small differences in the lattice parameters may arise from the temperatures used in the literature (900 °C and 1000 °C respectively).
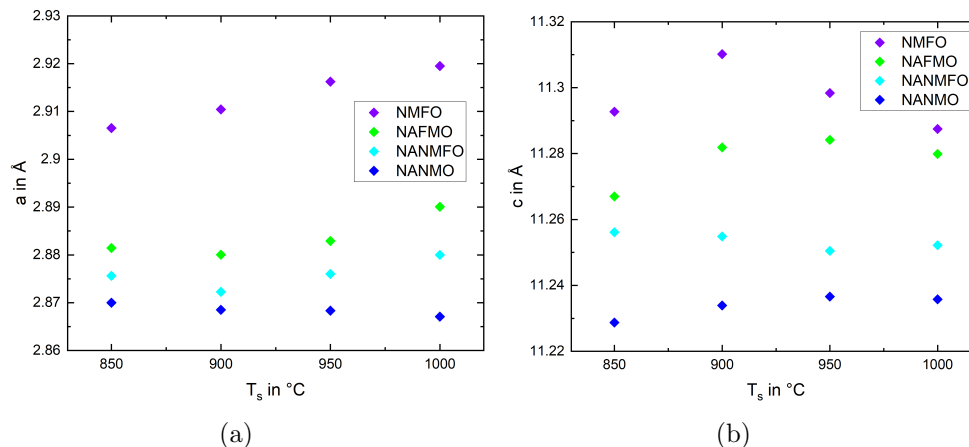
Figure 5.8: **Sintering temperature dependent lattice parameters:** The two lattice parameters a and c are shown in (a) and (b) respectively. Refinement was done for the XRD patterns shown in Figure 5.7, resulting in four refinements for each sintering temperature T_s and each material.

In Chapter 5.3 the evolution of these parameters during electrochemical cycling is described and compared for the different materials. Especially the c-parameter which is twice the distance between the transition metal oxides layers, changes significantly during insertion and deinsertion of the sodium ions. In Chapter 5.3 in situ XRD during charge and discharge will be used to investigate how the lattice parameters a and c and the sodium occupancy changes during electrochemical cycling.

Analogous to the investigation before about how different temperatures affect the particle morphology (Table 5.3) and how this affects the electrochemistry later in Chapter 5.4 one must take into account how the crystal structure is temperature dependent as well. Figure 5.7 shows a comparison of how the crystal structure has evolved with different sintering temperatures. Again there is a distinct difference between the nickel containing (NANMO & NANMFO) and nickel-free materials (NAFMO & NMFO). For NANMO and NANMFO the trigonal impurity phase $R - 3mH$ (marked with *) is most prominent at lower temperatures and receding with higher temperature. All other reflections belong to the P2-type structure (marked with green hkl-ticks analogue to Fig. 5.6). The intensity ratio between the reflections of the individual scans is changing for the nickel containing materials (e.g. 102 at around 39°). At angles beyond 30° higher sintering temperatures increase the intensity and sharpness of the reflections.

Contrasting this there are almost no impurity phases visible for the nickel-free materials (Fig. 5.7 (c) & (d)). Only for NMFO additional reflections (unknown impurity) start to appear but this time at high temperatures (vice versa to nickel-containing at low temperatures). In the temperature range investigated the intensity does not change much with higher temperatures.

Rietveld refinements with the software *Topas* resulted in lattice parameters presented in Figure 5.8 (diagrams of refinement in the appendix). The XRD patterns and the

refinements show that the P2-type layered crystal structure are well developed for all investigated T_s. The structure of NAFMO and NMFO is already well developed without impurities at lower temperatures (850 °C to 900 °C). Higher temperatures have a strong influence on the particle morphology, while shifts in the lattice parameters are visible as well. It was observed before that sinter activity of iron-rich materials is higher than for the two nickel containing CAMs. The nickel-containing materials (NANMO & NANMFO) require higher temperatures (950 °C to 1000 °C) until impurity phases vanish, while the lattice parameters change slightly. In terms of sustainability and energy consumption during sintering the lower temperature would be preferable in general.

5.1.5 Chemical analysis

To control the chemical composition of the synthesized materials measurements with ICP-OES were performed. The materials after the second heat treatment were measured since this represents the final state of the material which was later used for battery cycling. The amount of carbon in the samples was also measured, since the precursor materials consisted of acetates and nitrates. Table 5.5 summarizes the measured values of the elements in mass percent (M%). The error $\pm$ arises from the measurement itself as a measuring inaccuracy. Light elements like carbon, oxygen and sodium show relatively high measurement errors with the chosen analysis method. The chemical composition according to the molecular formulas (like in Fig. 3.1) was calculated without considering the carbon content any further, since the formulas do not provide any amount of carbon, while the carbon content in the samples was very low as it was expected after heat treatments at 950°C in air atmosphere. The measured oxygen amount corresponded approximately to the expected value of an oxide ($NaTMO_2$) which was also no surprise when sintering in a oxygen-rich atmosphere, but due to the big error it was also not taken into account for the calculations.

The calculated chemical composition (Calc. CC in Tab. 5.5) for sodium, aluminium and the transition metals reaches the theoretical (Theo. CC). Small differences are within error range. The synthesis of the desired composition was performed successfully.

Table 5.5: **ICP-OES data:** The amount of the measured elements is listed in mass percent (M%) along with inaccuracy ($\pm$). From that the chemical composition accordingly to the molecular formulas (see Fig. 3.1) was calculated (Calc. CC) again with the corresponding error ($\pm$) . The theoretical chemical composition (Theo. CC) is listed in the last column.

		M %	$\pm$	Calc. CC	$\pm$	Theo. CC
NANMO	C	0.27	0.024			
	O	31.90	2.520			
	Na	13.44	0.444	0.591	0.020	0.6
	Al	2.90	0.075	0.109	0.003	0.11
	Mn	36.20	0.615	0.666	0.011	0.66
	Ni	13.01	0.169	0.224	0.003	0.22
NANMFO	C	0.34	0.030			
	O	33.10	3.012			
	Na	13.70	0.425	0.602	0.019	0.6
	Al	3.06	0.073	0.115	0.003	0.11
	Mn	36.20	0.796	0.666	0.015	0.66
	Fe	5.43	0.163	0.098	0.003	0.11
	Ni	6.36	0.095	0.109	0.002	0.11
NAFMO	C	0.31	0.027			
	O	32.40	2.948			
	Na	13.30	0.412	0.587	0.018	0.6
	Al	3.01	0.072	0.113	0.003	0.11
	Mn	36.30	0.799	0.671	0.015	0.66
	Fe	12.00	0.360	0.218	0.007	0.22
NMFO	C	0.24	0.021			
	O	31.40	2.857			
	Na	12.90	0.400	0.583	0.017	0.6
	Mn	36.20	0.796	0.685	0.014	0.666
	Fe	17.50	0.525	0.326	0.009	0.333
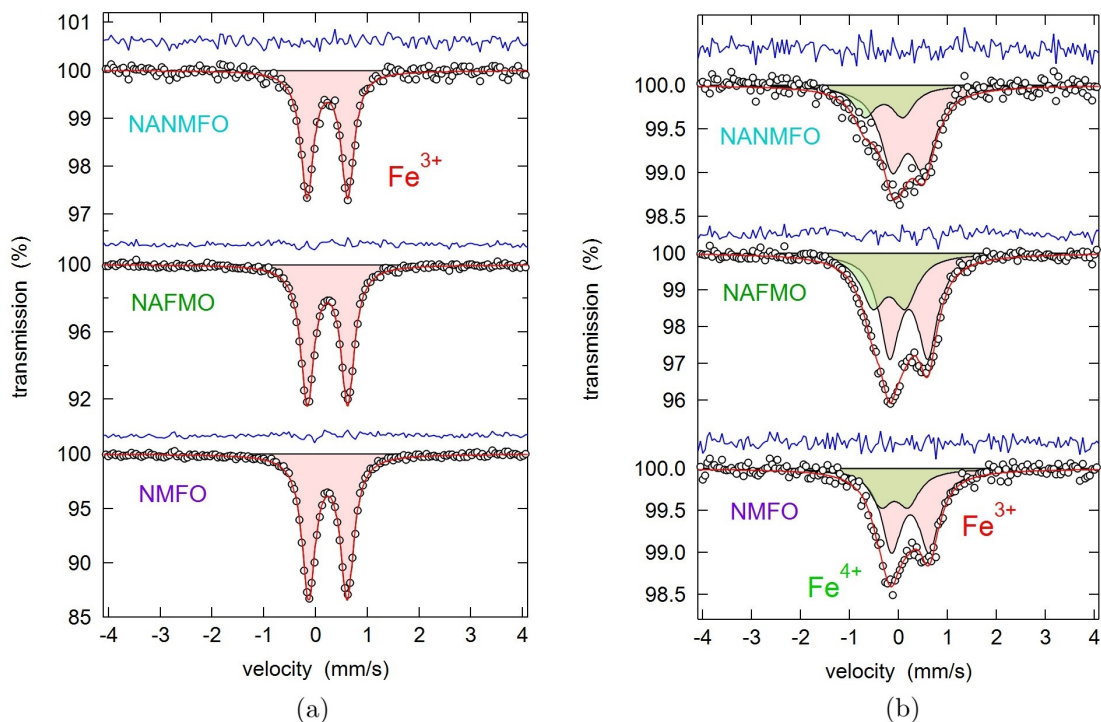
Figure 5.9: **Mößbauer spectroscopy:** From top to bottom: NANMFO, NAFMO, NMFO. (a) Shows the pristine materials after the heat treatment of 950 °C and (b) charged cathode material measured ex situ.

5.1.6 Mößbauer spectroscopy

When substituting nickel with iron in a cathode material one expects the substitutional element to attribute to the capacity with its redox reactions. In other words the redox pairs of iron need to replace the pairs of nickel. It is not certain if that is possible in the same electrochemical window. Textbook knowledge suggests that elements with higher atomic number show higher redox potentials (e.g. Fe < Ni). It can also be expected that in general the redox potential of higher oxidation states is higher compared to lower states [65]. However Nanba et al. [65] pointed out that the redox potential positions of late transition metals may differ from those simple rules and depend on the chemical composition. In the case of P2-$Na_{2/3}Ni_{1/3}Mn_{2/3}O_2$ by Xiao et al. [66] the redox reaction of Ni^{4+}/Ni^{3+} was measured between 3.53 V to 3.69 V (Ni^{3+}/Ni^{2+} between 3.24 V to 3.33 V) which is in agreement with Hasa et al. [35] where corresponding potential was close and below 3.7 V for the composition of NANMO. However Fe^{4+}/Fe^{3+} shows in general a higher redox potential in sodium ion batteries compared to the nickel counterpart [67]. For the composition $Na_{2/3}Fe_{1/3}Mn_{2/3}O_2$ Phuong et al. [67] found a voltage of 4.1 V. In general when P2-type layered oxides are charged to high voltages beyond 4.0 V some of the occurring redox reaction is attributed to a phase transition from P2 to O3 type [36, 68]. This might overlap with the Fe^{4+}/Fe^{3+} process (discussed later in Chap. 5.4 Electrochemistry, & 5.3 In situ XRD).

Since in the later Chapter 5.4 *Electrochemistry* the different chemical compositions of cathode materials are compared in the same voltage range it was of interest to investigate if and to what extent the oxidation state of Fe^{4+} was achieved when the three iron containing samples were charged to 4.6 V. As it was described before in Chapter 5.1.1 the iron amount has changed the morphology of the active material. So different iron amount influences electrochemical behaviour through two effects, morphology and chemistry. When trying to understand how a certain capacity is achieved the attribution of both needs to be known. It must be noted that Fe^{4+} is in general not stable outside of a battery cell however, which makes ex situ measurements difficult. Careful handling under argon atmosphere should at least minimize the risk of Fe^{4+} being reduced to Fe^{3+} [69].

Mößbauer spectroscopy was performed on the pristine material (uncharged) and on charged cathodes. In both cases material prepared with a final sintering step of 950 °C was chosen. To receive better intensities thicker cathodes were prepared in the same fashion comparable to the electrochemical cycling in Chap. 5.4 but with a 800 µm gap size of the doctor blade. The resulting mass loading was 4-5 times higher than with the regular gap sizes of 200 µm. The built half cells were treated with a formation step with 1C at the beginning and then slowly charged with C/20 to 4.6 V. This voltage was held until the necessary current fell below C/50. The coin cells were brought back into argon atmosphere of a glove box and opened. The cathodes were washed with pure Dimethylcarbonate (DMC) and scratched off the current collector. Even with the thicker electrodes not enough charged active material could be provided from one single coin cell to reach the desired 30 mg to 50 mg sample weight. This made it necessary to combine charged active material from two coin cells that were treated the same way and showed similar and good cycling profiles. 40 mg of the individual cathode materials were sealed in pouch bags under argon atmosphere and measured in the Mößbauer-Spectroscope for approx. two weeks (depending on the Fe concentration) until the signals were distinctly visible and the noise at a low rate.

Figure 5.9 shows the measured spectra of the three pristine (a) and charged materials (b). From top to bottom the following are displayed: NANMFO, NAFMO and NMFO. In case of the pristine material we can see a typical double peak representing a single oxidation state of iron. For all three charged samples a deformation is visible which corresponds to an overlap of two states. It is notable that for charged NANMFO with the lowest iron concentration the signal is less prominent over the noisy background.
The spectra of the pristine material exhibits an isomeric shift (IS) of about $0.33\,\mathrm{mm\,s^{-1}}$ and a quadrupole splitting (QS) of $0.75\,\mathrm{mm\,s^{-1}}$ to $0.79\,\mathrm{mm\,s^{-1}}$ (see also Tab. 5.6). It can be interpreted that iron is only present in trivalent form with octahedral oxidic environment. This fits the P2-type crystal structure described earlier [70, 71].
The doublet of Fe^{3+} can also be found in the case of the charged materials. Fitting a Fe^{3+} doublet in Fig. 5.9 (b) shows how the peaks have broadened, which is a sign for increased disorder in the structure. Oxidation of neighbouring manganese and iron are likely to have induced distortions and therefore disorder of the local oxygen octahedra environment. A second doublet with a much smaller isomeric shift attributed to

Table 5.6: **Fit parameters of Mößbauer spectroscopy:** Corresponding parameters to Fig. 5.9. Displayed are the isomeric shift (IS), quadrupole splitting (QS), line width Γ and the area under the curve covered by the doublet fits.

		IS	QS	Γ	area fraction
pristine					
NANMFO	Fe^{3+}	0.33 ± 0.01	0.79 ± 0.01	0.30 ± 0.01	100.0%
NAFMO	Fe^{3+}	0.33 ± 0.01	0.78 ± 0.01	0.31 ± 0.01	100.0%
NMFO	Fe^{3+}	0.34 ± 0.01	0.75 ± 0.01	0.31 ± 0.01	100.0%
charged					
NANMFO	Fe^{3+}	0.31 ± 0.02	0.65 ± 0.02	0.59 ± 0.04	73.5%
	Fe^{4+}	-0.20 ± 0.03	0.78 ± 0.04	0.55 ± 0.11	26.5%
NAFMO	Fe^{3+}	0.31 ± 0.01	0.78 ± 0.01	0.50 ± 0.02	62.6%
	Fe^{4+}	-0.09 ± 0.02	0.66 ± 0.02	0.60 ± 0.04	37.4%
NMFO	Fe^{3+}	0.35 ± 0.01	0.77 ± 0.01	0.50 ± 0.03	68.0%
	Fe^{4+}	0.02 ± 0.03	0.56 ± 0.04	0.55 ± 0.07	32.0%

Fe^{4+} [69] became visible for the charged materials. The oxidation of trivalent iron to the tetravalent state is therefore evident but apparently the oxidation did not take part completely. A complete oxidation could be achieved with a higher cut off voltage during charging, lower charging currents, thinner electrodes or more porous active material. To compare the ratio of Fe^{4+} / Fe^{3+} for the different charged materials one can take a look to the area fraction covered by the fitted doublets in Fig. 5.9 and Table 5.6. The lowest amount of Fe^{4+} was measured for NANMFO. One can explain this with NANMFO containing the lowest amount of iron but also nickel which is oxidized to Ni^{4+} at the voltage region 3.5 - 3.7V. When calculating the theoretical capacity from the available sodium and the redox couples less iron needs to be oxidized into tetravalent state to reach the measured capacity.

The other two compositions contain no nickel at all, which is why only Fe can attribute to the capacity when oxidized to Fe^{4+} in the higher voltage region. The ratio is higher for NAFMO than for NMFO. Reason for that might be the porosity and the primary particle size. In Table 5.3 in Chapter 5.1.1 it was shown that NAFMO shows a porosity of 32 % almost double of NMFO's porosity of 18 %. In case of NAFMO more active material from the centre of the particles can participate in the redox reaction into the higher state, which is a possible reason for the higher capacity shown later in Chap. 5.4. A similar effect can be attributed to the bigger primary particle size of NMFO. This is also a reason why an active material particle might not be completely de-sodiated, so less of iron is oxidized into the tetravalent state. Due to the long measurement time of Mößbauer spectroscopy and need of spectroscope for other works at the institute, it was not possible extend the presented work to measure also the three charged CAMs with different sinter temperature (3 materials, 4 sinter temperatures in total). It is assumed

that there would be little change for the spectroscopy data for the adjacent sinter steps of 900 °C and 1000 °C. Therefore the error by transferring the expected Fe^{4+} amounts to the sinter range of 850 °C to 1000 °C is considered to be small.

5.2 Conductivity properties

Layered oxides used as cathode materials in LIB exhibit a mixed conductivity of electronic and ionic nature [16]. In general, the electronic transport in a cathode is enhanced by adding conductive carbon when the electrode slurry is prepared. This acts as a connection between the particles and between particles and current collector. But the pure active material's electronic conductivity is not influenced by that and can be understood as a material constant specific for a certain chemical composition with a certain crystal structure and porosity [16]. The same material constant is intrinsically given for the ionic conductivity of the active material where the ionic kinetics begin after the ions have left the liquid phase of the electrolyte. Particle morphology, conductivities and charge transfer resistance at the interfaces determine the overpotential during charge and discharge in a cell [16]. All these mentioned properties are necessary for calculations and simulations of battery materials and their electrochemical behaviour. A digital model could predict certain behaviour of certain materials and help understand the involved processes [72].

5.2.1 About measurement and circuit model

There are only few reports about these intrinsic conductivity properties present in literature. For Lithium NMC-111 Zahnow et al. [16] managed to separate electronic and ionic conductivity with electrochemical impedance spectroscopy on pressed and sintered pellets of pure active material. There are even fewer reports for layered sodium oxides where a similar mixed conductivity of ionic and electronic nature can be expected. Walczak et al. [73] measured conductivities of layered sodium oxides with EIS but did not distinguish between electronic and ionic. This work presents a study of the before mentioned four different cathode materials based on the method of Zahnow et al. [16].

Pellets prepared as mentioned in Chapter 4 can be understood as a simple plate capacitor, where the gold and silver contacts act as electrodes and the pellet itself as a dielectric medium. A simple physical equivalent circuit that describes the measured impedance spectrum is shown in Figure 5.10 on the left. Resistor R_e represents the elec-
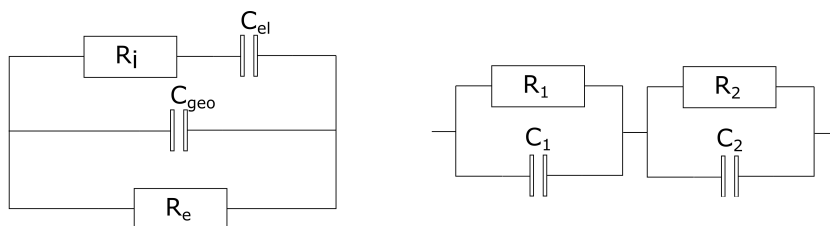
Figure 5.10: **Equivalent circuits:**   Left: Physically meaningful circuit from Zahnow et al. [16] with ionic resistance R_i, electronic resistance R_e, geometric capacitance C_{geo} and interface capacitance C_{el}. Right: Simple model with two RC-elements in series, used for the fit in the work of Zahnow et al..

tronic resistance of the pellet and capacitor C_{geo} (geometric capacitance) is equivalent to the gold/silver contact electrodes. Ions can flow through the pellet as well and their resistance is represented by resistor R_i. However they cannot penetrate the gold/silver layers which act as ion-blocking electrodes. This can be described with a capacitor C_{el} (electrode interface) in series to the ionic resistor R_i. In case of a direct current flow this would act as an open circuit since the ions can not transfer beyond the blocking electrodes.

This physically meaningful model however is difficult to fit to the measured data due to the overlap of the ionic an electronic elements in the equivalent circuit. In case of Zahnow et al. [16] there was a deformed semi circle visible (indicating the overlap) and in the analysis with distribution of relaxation times (DRT) two significant peaks were present, making a fit with two RC-elements in series feasible. Therefore, Zahnow et al. [16] suggested to fit a simpler model of two RC-elements with the resistors R_1 and R_2. Alternatively two RC-elements in series can be used if the semicircles show compressed shape (see Fig. 5.10 right). The equivalent values for the electronic and the ionic resistance are calculated according to the following equations:

$$R_e = R_1 + R_2 \tag{3}$$

$$R_i = \frac{R_e \cdot R_1}{R_e - R_1} = \frac{R_1^2}{R_2} + R_1 \tag{4}$$

In the following the experiments for this conductivity analysis are described with more details.

The pellets were prepared as described in Chapter 4.3.4: After being pressed with a force of $20\,\mathrm{kN}$ into small discs of $12\,\mathrm{mm}$ diameter and then sintered at $950\,°\mathrm{C}$ the internal texture of a pellet differs from the morphology of the powders. Figure 5.11 shows SEM cross sections of the pellets measured with impedance spectroscopy. They were mechanically polished and ion-etched to show the internal texture of the pellets. (a) shows a pellet from the material $Na_{0.6}Al_{0.11}Ni_{0.22}Mn_{0.66}O_2$ (NANMO): Here the material was densely sintered together to a porosity of $\Phi = 22\,\%$. $Na_{0.6}Al_{0.11}Ni_{0.11}Fe_{0.11}Mn_{0.66}O_2$ (NANMFO) (b) shows bigger pores between dense regions ($\Phi = 27\,\%$). In case of $Na_{0.6}Al_{0.11}Fe_{0.22}Mn_{0.66}O_2$ (NAFMO) (c) only pores in a dense material are visible similar to NANMO. Even after being pressed and sintered the former primary particles are still recognizable in case of $Na_{0.6}Fe_{1/3}Mn_{2/3}O_2$ (NMFO) (d). This can be compared to the values in table 5.3 (Chap. 5.1.1) about the porosity change of secondary particles after sintering at different temperatures. The intra-particular porosity changed for NMFO from $39\,\%$ to $12\,\%$ in the range of $850\,°\mathrm{C}$ to $1000\,°\mathrm{C}$ and for NAFMO from $48\,\%$ to $22\,\%$. This behaviour was ascribed to a stronger sinter activity if a higher iron content is present. The shrinkage parameters of the pellets were calculated to $2.32 \cdot 10^{-2}$, $3.06 \cdot 10^{-2}$, $5.52 \cdot 10^{-2}$ and $7.28 \cdot 10^{-2}$ for NANMO, NANMFO, NAFMO and NMFO respectively, increasing with the iron content. For the morphology of unpressed powders (presented in Chap. 5.1.1) it was visible that the primary particle size increased with

(a)   (b)

(c)   (d)
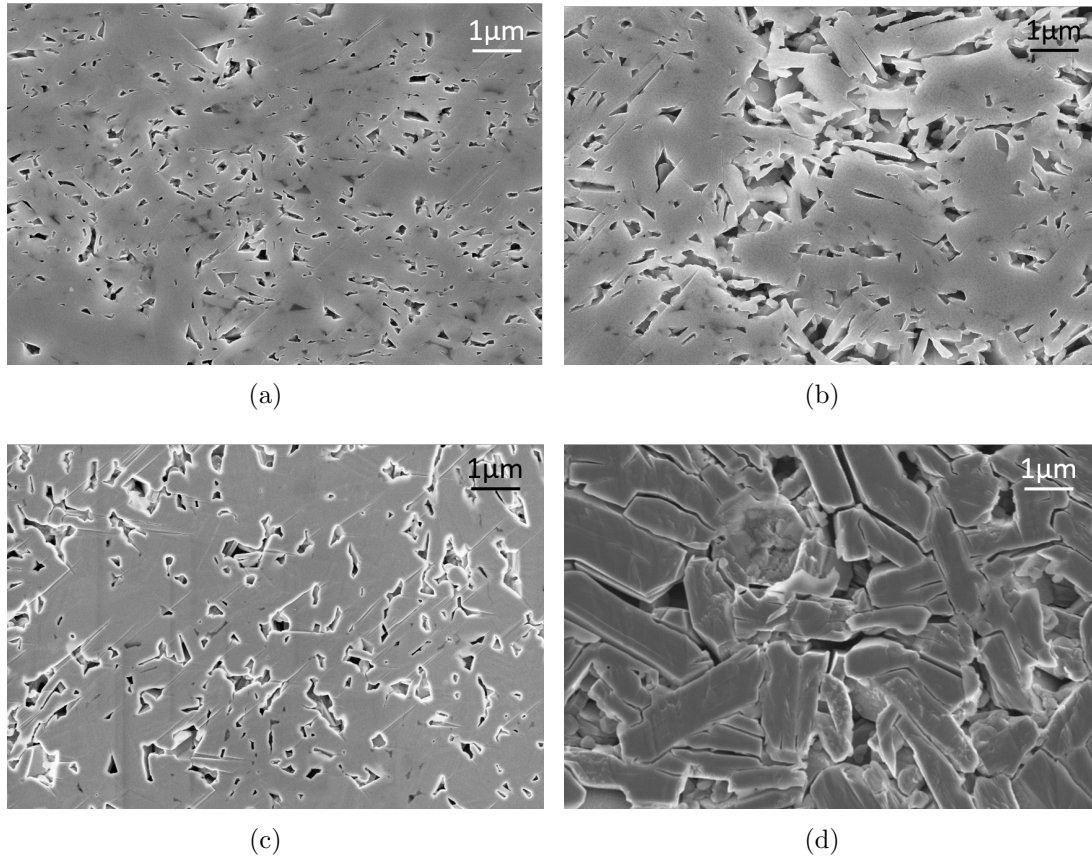
Figure 5.11: **Pellet cross section:** The pellets were processed with the same parameters
and different materials show different internal textures and porosities Φ.
SEM pictures of polished and ion-etched internal texture of the pellets: (a)
NANMO Φ = 22 % (b) NANMFO Φ = 26 % (c) NAFMO Φ = 20 % and
(d) NMFO Φ = 24 %.

increasing iron content, due to the stronger sinter activity. This strong sinter activity
and shrinkage of NMFO creates large primary particles (PP) but apparently merging
of large neighbouring particles is not favoured. The pores in the NMFO pellet appear
to be long crack-like gaps which has an influence on the measured conductivity of this
sample. In case of NAFMO (Fig. 5.11 (c)) some of the visible crack-like gaps look like
straight lines which are most likely carved into the material by the ion beams and not
a sample property. Here the sintering of neighbouring particles merged them beyond
recognition which also affects the conductivity measurement. Single particles are also
not recognizable for NANMO (a) and NANMFO (b) either. However for the internal
pellet porosity a simple proportionality depending on the iron content alone can not be
assumed as it was done before for the SP porosity.
For the EIS experiment a homogeneous porosity with similar values for all materials
would be preferred. The porosity appears to depend on the material even-though treated
with the same pressing force (20 kN) and sintering temperature ($T_s = 950$ °C). A falsifi-

cation of conductivity data due to different porosities makes an evaluation difficult when comparing different materials. It is possible that with higher pressing force (e.g. 30 - 40 kN) or longer dwell time at T_s (e.g. 12 h to 20 h) more dense pellets can be achieved. In such a way the more similar porosities for the different materials could be achieved and hence reducing the error due to different values of Φ. Zahnow et al. [16] compared the influence of different porosities on the conductivity behaviour. Even though the four materials exhibit not exactly the same porosities (ranging from 20 % to 27 %), the values for Φ are still rather similar. The measured conductivities are in that case derived from primary particle size and/or the chemical composition.

5.2.2 Nyquist-plots and updated model

Figure 5.12 (a) shows Nyquist-plots of the four different cathode materials at 60 °C. In a diagram with Nyquist representation the data points with highest frequency are located on the left, in general close to the origin. Passing through the set range of frequencies from high to low the next data point is shifted to the right. At highest frequencies (see Fig. 5.12 (b)) a small process is present, which is barely visible at temperatures around 60 °C. A big semicircle starting past the small process in the high frequency region similar to the literature of Zahnow et al. [16] can be seen for all materials but the shape of the spectra is changing significantly in the low frequency region for the individual materials. For NANMFO, NAFMO and NMFO a small, deformed semicircle appears to be overlapping the big one at low frequencies. The strongest deviation from a single depressed semicircle (like Zahnow et al. observed [16]) can be observed for NANMO. The big semicircle starting at high frequencies is not completely visible and continues into something that resembles a diffusional branch which can often be seen in the Nyquist-plots when investigating batteries with EIS.

This shows that the proposed model of Zahnow et al. [16] can not be used to fit the measured data. A semicircle that is not or only minimally compressed would be represented with an RC-element (ideal capacitor). However, the measured data in Figure 5.12 (a) shows a compression of the semicircles. This indicates that a model with non-ideal capacitors is required. For this purpose the capacitors in Figure 5.10 are replaced with constant phase elements (CPE). Therefore an RC-element in the model becomes a RQ-element. The updated model with two modified equivalent circuits is shown in Figure 5.13 and will be explained in the following. The smallest process at highest frequencies (seen in Fig. 5.12 (b)) is likely attributed to the contact resistance (according to Gaberscek et al. [74]). In the equivalent circuit model it is represented as resistor R_a for the offset on the x-axis (real part of the impedance Z') and a RQ-element with R_b and CPE_b. R_a is several orders of magnitude smaller and R_b one order of magnitude smaller than R_1 and R_2. R_a and R_b are not necessary for the further analysis and the understanding of the physically meaningful equivalent circuit and are just needed for a clean fit.

For the iron containing cathode materials (NANMFO, NAFMO & NMFO) a big semicircle starting at the high frequency region (left hand side of Nyquist-plots) is overlapping

(a)

(b)
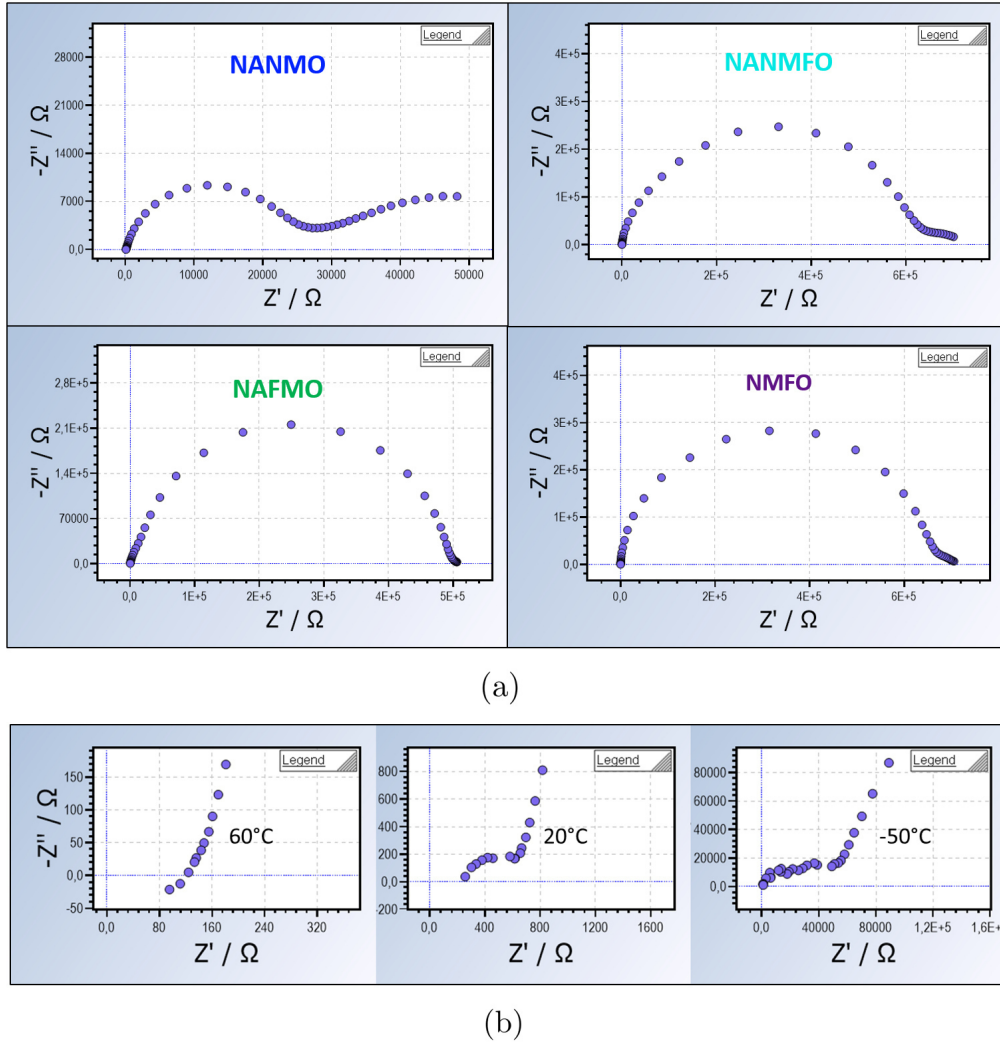
Figure 5.12: **Nyquist-plots:** Typical impedance spectroscopy data of the 4 layered ox-
ide materials at T $= 60\,°$C is presented in (a). The specific shape of the
Nyquist-plot strongly depends on the chemical composition. In (b) a mag-
nification close to the origin of the NANMO Nyquist-plot is shown at three
different temperatures. The axis in these plots is decreased by two orders
of magnitude as compared to (a). (Diagrams created with the software *Re-
laxis*)

the small one which starts at low frequencies (right hand side of plot). A use of two RQ-
elements in series is therefore reasonable [16]. In case of the nickel containing materials
NANMO and NANMFO the data points in the low frequency region are further away
from the x-axis, than for the other two CAMs. This can be seen especially for NANMO,
where the low frequency semicircle is not completely visible. Scanning to even lower
frequencies would reveal a complete semicircle and bring the last data point closer to
the x-axis. Since NANMO generates Nyquist-plots with unexpected shape, that differs
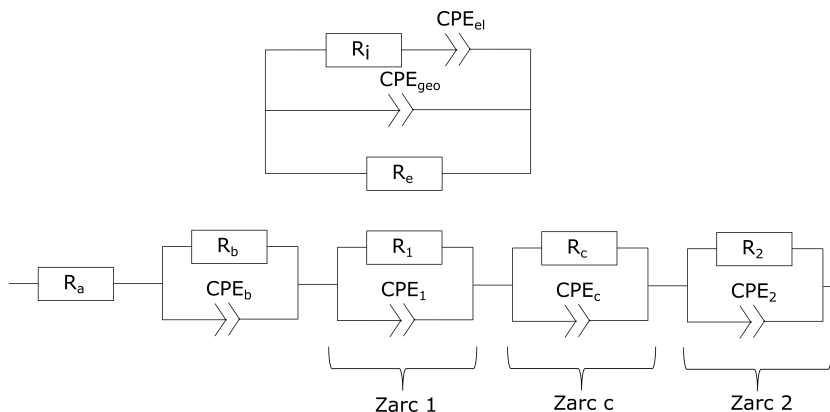
Figure 5.13: **Updated circuit model:**   At the top a physically meaningful circuit model with non-ideal capacitors describes a pellet with mixed conductivity, enclosed by a current collector, analogous to the top one in Fig. 5.10. At the bottom an alternative model for the fit is presented. The model from Zahnow et al. [16] from the bottom of Fig. 5.10 was modified: Non-ideal capacitors (constant phase elements) were used here as well and additional RQ-elements were necessary to fully describe the measured spectra.

strongly from the other CAMs it is necessary to check if a model with two RQ-elements in series still can be applied.

A possible approach is the analysis of the measured data with DRT [16]. Fourier transformation converts the frequency based impedance data into a distribution of time constants which corresponds to relaxation times of a certain process. Zahnow et al. confirmed their model with DRT as well. Using this technique, EIS data can be deconvolved to reveal the typical relaxation times of charge transfer processes.   The DRT analysis is shown in figure 5.14 with the DRT function γ depending on the relaxation time τ. At certain relaxation times the response of the system causes peaks in the γ function, which can be temperature dependent. Two strong peaks can be seen, which most likely correspond to the two RC- or RQ-elements, which were suggested by Zahnow et al. [16]. However, the DRT shows that another small peak in-between is present. According to literature [16] this supports another RQ-element for a clean fit, denoted by R_c and CPE_c. This model can be applied for the iron containing materials as well, where $R_c = 0$, since no additional process was visible. An overlap of the 2 or, in case of NANMO, 3 processes makes a fit difficult. Therefore it is helpful to give a start value. The relaxation time τ of the peaks in the DRT analysis can be used for this purpose, since each of them represents a RQ-element. An RQ-element can also be understood as a Zarc-element [16], consisting of a resistor and a relaxation time.

With this interpretation the equivalent circuit model at the bottom of figure 5.13 is complete. In analogy to equations 3 and 4 electronic R_e and ionic resistance R_i can now
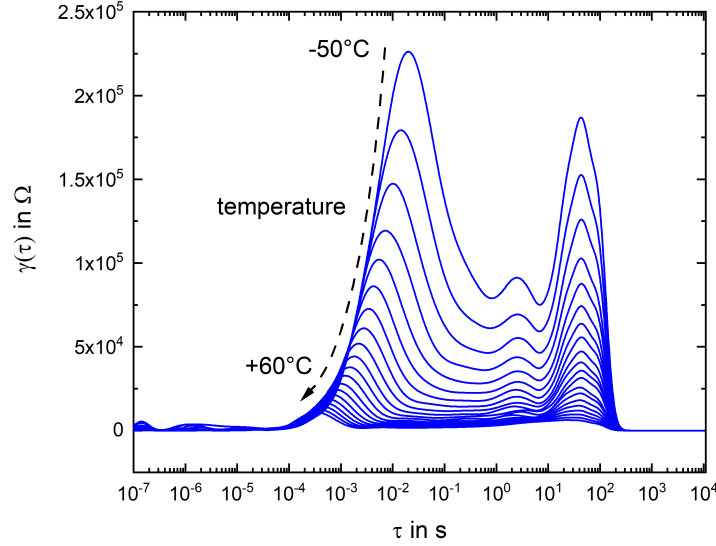
Figure 5.14: **DRT of NANMO:** The distribution is presented as the function γ depending on the relaxation time τ. For low temperatures and high resistance the response of the system is "strong", resulting in higher peaks as compared to higher temperature, with lower resistance.

be calculated according to:

$$R_e = R_1 + R_c + R_2 \tag{5}$$

$$R_i = \frac{R_e \cdot R_1}{R_e - R_1} \tag{6}$$

An exemplary simulation of this model is shown in Figure 5.15 to demonstrate that the data interpretation and model are valid. In Figure 5.15 four spectra are shown: In (a) the measured EIS spectrum of NANMO at $T = 60\,°\text{C}$ in the frequency range from $7\,\text{MHz}$ to $10\,\text{mHz}$ is presented (identical to Fig. 5.12). With the applicable model from the bottom of Figure 5.13 and equations 5 & 6 the values for R_e and R_i were calculated from (a). These values for electronic and ionic resistance were then used in the physically meaningful model (top of Fig. 5.13 or Fig. 5.15 (b)). With the tool *Circuit simulator* of the *Relaxis* software a simulation of the physically meaningful model was created. The Nyquist-plot of this simulation is shown in Figure 5.15 (b) and is quite similar to the measured data in Fig. 5.15 (a). (c) shows an overlay of measured and simulated data and reveals a small deviation which is due to the values of CPE_{el} and CPE_{geo}. These values were estimated and then fitted to the data, since they were not calculated in equation 5 and 6. Still a good agreement between measurement and simulation confirms the approach chosen here. Figure 5.15 (d) shows how the simulated circuit would behave if the lower frequency level were be shifted from $10\,\text{mHz}$ (like in the measurement) to $1\,\text{µHz}$. The latter would be difficult to observe experimentally, due to the long measurement time, which poses the risk of violating time-invariance [75]. Error-prone and invalid EIS
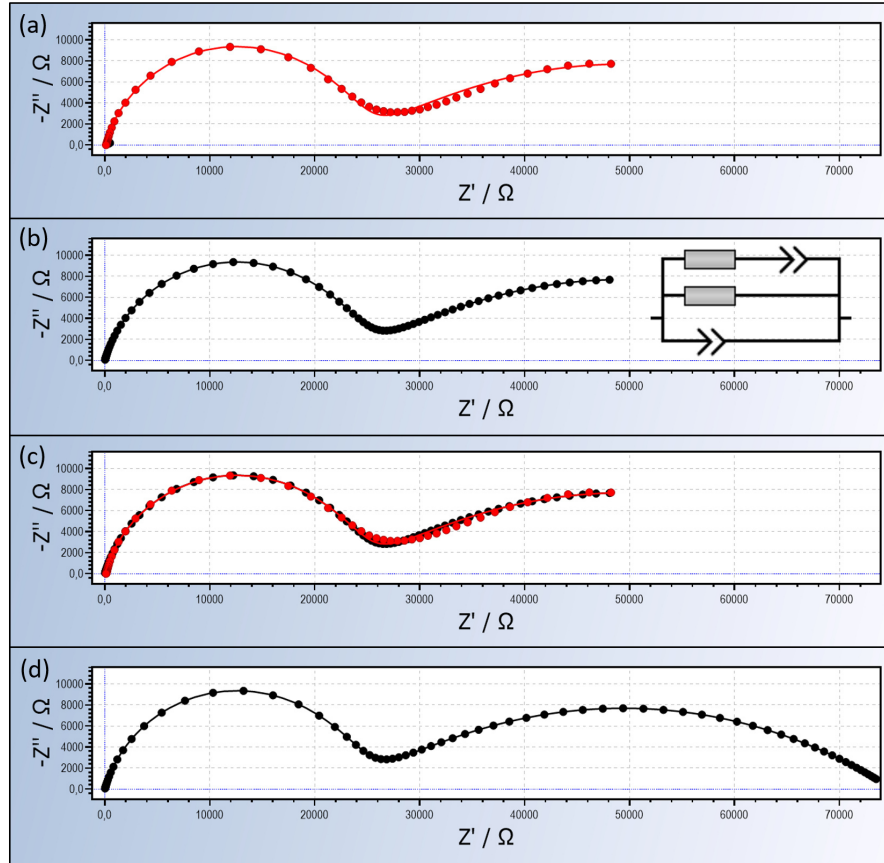
Figure 5.15: **Measured and simulated EIS spectra:** (a) shows the measured EIS data of a NANMO pellet at $T = 60\,°C$ in the frequency range $7\,MHz$ to $10\,mHz$. A simulation with the values of R_e and R_i in the physically meaningful model was created. Both model and simulation are shown in (b). An overlay of measured and simulated curve is presented in (c). (d) shows the simulation with a lower frequency limit of $1\,µHz$. Simulation and plots were created with the software *Relaxis*

data could be the consequence. The simulation makes it possible to demonstrate what the second semicircle could look like.

5.2.3 Conductivities and Arrhenius-plots

With the fitted model the resistances for both transport processes (electronic and ionic) were calculated via equations 5 and 6. With measured lenght l and area A of the pellets the specific conductivities σ_j $(j = e, i)$ for both processes were calculated via:

$$\sigma_j = \frac{l}{A} \cdot \frac{1}{R_j} \tag{7}$$

To receive the specific conductivities for a certain temperature this experiment was repeated in the range of $-50\,°C$ to $60\,°C$ with steps of $\Delta T = 5\,°C$. A linear depiction
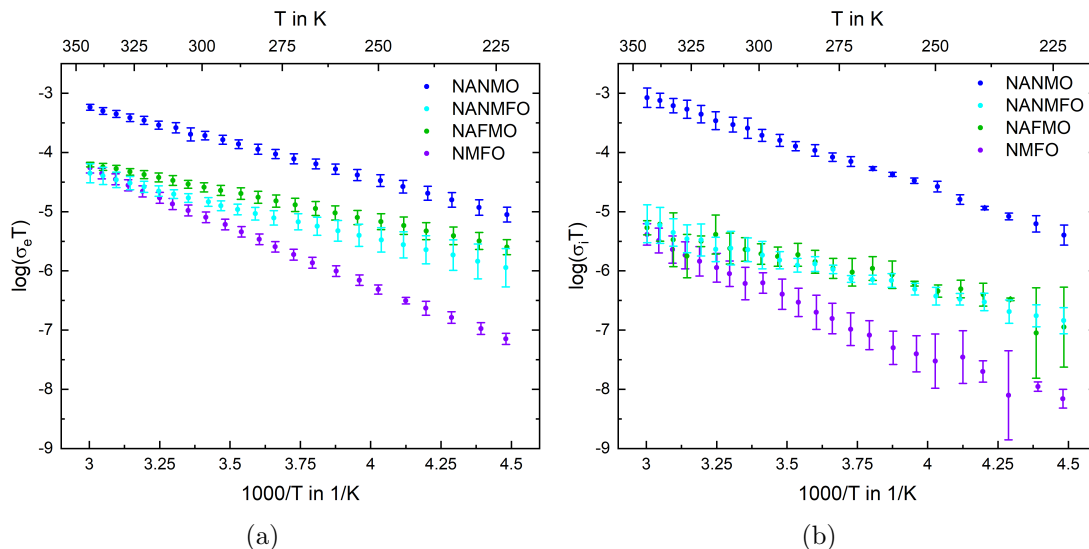
Figure 5.16: **Arrhenius plots:** Linear depiction of electronic (a) and ionic (b) conductivities. Colour code: NANMO (blue), NANMFO (cyan), NAFMO (green), NMFO (purple).

of the temperature dependent conductivities are shown in Fig. 5.16 and enables the calculation of the activation energies for the transport mechanism. Note that for the plots in Fig. 5.16 the decimal logarithm was used to allow an easier, visual interpretation but for the calculation of a linear regression the natural logarithm was used according to equation 8. For the ionic conductivity it can be noted that the values for most materials fluctuate at low temperature (<250 K) and deviate from the linear shape. In general, it can be noted that the resistor R_2 was more difficult to fit to the data and is therefore an error source. In the calculation of R_i via eq. 4 this error is more prominent than in case of R_e. Still for both electronic and ionic conductivities a typical exponential temperature dependence was observed which is in agreement with the Arrhenius-equation:

$$\sigma = \frac{\sigma_0}{T}\exp\left(-\frac{E_{\mathrm{A}}}{k_{\mathrm{B}}T}\right) \tag{8}$$

This can be understood as hopping motion of Na^+ electrons and ions with the activation energy E_A [16]. σ_0 is the conductivity prefactor and k_{B} the Boltzmann-constant.

The fluctuation of values for the ionic conductivity σ_i especially at low temperatures can be understood since the ionic processes are in general slower than the electronic ones. This means a long relaxation time can be attributed to the ionic processes and hence they can only be observed in the low frequency region of the electrochemical impedance spectroscopy. EIS at low frequencies however, is error-prone due to long measurement time and therefore bears the risk of violation of time-invariance which is a requirement for EIS measurements [75]. Additionally measurements at low temperature (<250 K$= -25$ °C) deviate strongly from room temperature conditions where the

Table 5.7: **Conductivity properties:** Activation energies E_{A_j} and conductivities at T = 20 °C σ_j for electronic and ionic mechanisms ($j = e, i$). Also listed is the average porosity Φ of the corresponding samples. The standard deviation was added for an error estimation.

Material	E_{A_e} in meV	E_{A_i} in meV	σ_e in S/cm	σ_i in S/cm	Φ
NANMO	241 ± 6	295 ± 19	6.4 ± 0.5 E-07	7.1 ± 0.2 E-07	22 ± 1
NANMFO	212 ± 52	215 ± 61	5.2 ± 0.8 E-08	6.8 ± 1.7 E-09	26 ± 1
NAFMO	187 ± 12	188 ± 12	9.0 ± 1.3 E-08	7.7 ± 2.8 E-09	20 ± 3
NMFO	390 ± 1	378 ± 13	2.8 ± 0.4 E-08	1.8 ± 0.6 E-09	24 ± 1

regulation through the cooling device works close to it's limits. This poses another risk for error since stronger temperature fluctuation is a change of the measurement system, violating the principle of stationariness [75]. These two errors add up and are most likely the reason for the non-linear behaviour in the ionic Arrhenius-plot (Fig. 5.16 (b)) at low temperature. The error from low temperatures due to the cooling device apply for the electronic conductivities as well. The error bars indicate this uncertainty.

5.2.4 Results and discussion of conductivity properties

The results of this analysis are summarized in table 5.7. Sorted from top to bottom the four cathode materials are shown from highest nickel content (NANMO) to highest iron content (NMFO). For each material the calculated value of the activation energy is given for the electronic (E_{A_e}) and ionic (E_{A_i}) hopping process. The activation energies for the electronic process are ranging from approx. $0.19\,\text{eV}$ to $0.39\,\text{eV}$.

It can be seen that the NANMO exhibits high electronic and ionic conductivity, while NMFO shows the lowest values for both. For NANMO (blue) and NAFMO (green) the values of Φ only differ by a few percent but their conductivities differ by one and two orders of magnitude respectively. While it can be assumed that the different porosities are responsible for some of the difference in σ_j, it is unlikely that it will change the value over several orders of magnitude. That means that some of the differences in the conductivities are probably related to the material itself. On the other hand NANMFO (cyan) and NAFMO (green) exhibit quite similar conductivities, despite more difference in their porosities.

In Chapter 5.1.3 *Tuning morphology via sintering temperature* it could be seen that Φ and A_{BET} are SP-properties with a correlation to the iron content. It was shown that from highest nickel content (NANMO) to highest iron content (NMFO) both Φ and A_{BET} were decreasing for the sintered secondary particles. This proportionality was observed for all investigated sintering temperatures ($T_s = 850\,\text{°C}$ to $1000\,\text{°C}$). However this simple proportionality can not be observed in case of conductivities (see Fig. 5.16 and Tab. 5.7). The conductivity mechanisms appear to be more complicated than that. Changing the amount of elements in the crystal framework or substitution of them can

influence the band structure of the material and therefore shift the transport mechanisms in different and complex ways [76].

Only some materials similar to NMFO are known in the literature. For comparison: Walczak et al. [73] made similar EIS investigations on $Na_{0.67}Fe_{0.5}Mn_{0.5}O_2$ & $Na_{0.67}Fe_{0.2}Mn_{0.8}O_2$ and observed a similar compressed semicircle like shown for NMFO in Fig. 5.16. However, they did not distinguish between electronic and ionic process and received their conductivity values from the fit of two RQ-elements in series which corresponds to R_e according to equation 3. These literature values of $0.39\,eV$ and $0.37\,eV$ (respectively) for the electronic activation energy E_{A_e} are similar to the obtained values for NMFO in this study and for the other chemical compositions as well. Therefore the composition of Ni-Fe-Mn results in values for activation energies higher than e.g. $NaFe_{0.5}Co_{0.5}O_2$ ($E_{A_e} = 0.16eV$) and lower than for most Nasicon $Na_3Fe_{2-y}Mn_y(PO_4)_3$ (y= 0 to 0.4) with $0.36\,eV$ to $0.55\,eV$ [77].

Table 5.7 also shows data for room temperature conductivities. $\sigma_e = 2.8 \cdot 10^{-8}\,S/cm$ (NMFO) to $6.4 \cdot 10^{-7}\,S/cm$ (NANMO) is in agreement with the measured data from Walczak et al. [73] where the composition with the highest iron content $Na_{0.67}Fe_{0.6}Mn_{0.6}O_2$ showed the lowest conductivity $\sigma_e = 5.78 \cdot 10^{-8}\,S/cm$. It needs to be noted that the sintering temperature for most samples in Walczaks work was 900°C. For Walczaks sample $Na_{0.67}Fe_{0.2}Mn_{0.8}O_2$ (similar to NMFO) a higher electronic conductivity of $\sigma_e = 4.02 \cdot 10^{-6}\,S/cm$ was measured but this sample underwent sintering at 800 °C. These two temperatures differ from the 950 °C used in this study which possibly explains the difference to NMFO. This supports the previously expressed assumption that for NMFO and NAFMO the optimal sintering temperature is below 950 °C (see Chap. 5.1.4), this time in terms of conductivity. Also, Walczak et al. did not specify which force was applied to press their pellets and what porosity was achieved in the sintering. Both have an influence on the finally achieved properties [16].

Since Walczak et al. [73] did not calculate an ionic share of the conductivity, the activation energy for ionic hopping E_{A_i} and ionic conductivity σ_i can instead be compared to the values for Li-NMC from Zahnow et al. [16]. They got $0.34\,eV$ to $0.59\,eV$ as activation energy for the ionic hopping mechanism which is almost the same for their measured E_{A_e}. The same appears to be true for the four layered sodium oxides were the activation energy for both processes is similar.

For a valid comparison of the conductivities a similar porosity and sintering temperature (e.g. 24 % and 950 °C) can be chosen and compare the room temperature data of NMC. The measured NMC data was $\sigma_e = 2.5 \cdot 10^{-8}\,S/cm$ and $\sigma_i = 4.9 \cdot 10^{-8}\,S/cm$, so the observed data was in the same order of magnitude for electronic and ionic conductivity with $\sigma_e < \sigma_i$. For the layered sodium oxides in Table 5.7 this is not the case. Here we can see that only for NANMO the conductivities are in the same order of magnitude. The other materials are an exception to that: The ionic conductivity is one magnitude smaller. The three iron conataining materials show $\sigma_e > \sigma_i$ which is contradictory to the NMC material. Only the nickel rich NANMO shows $\sigma_e < \sigma_i$, like it was the case for

NMC. NANMO also exhibits the highest value of σ_i for all of the here investigated materials. This is in agreement with the observed Nyquist-plots in Fig. 5.12 where for low frequencies the strongest diffusional branch was visible for NANMO which corresponds to good ionic conductivity.

A different feature is visible when comparing the activation energies for the ionic hopping process E_{A_i}. The activation energy in case of NANMO and NMFO are higher than in case of NANMFO and NAFMO. While these differences seem to be small they support another material property, which was observed with in situ XRD. Therefore E_{A_i} will be mentioned again later in Chapter 5.3 *In situ X-ray diffraction.*

In conclusion both conductivity processes of the four materials strongly differ with the chemical composition as seen in Fig. 5.16. σ_e and σ_i are both high for the nickel-rich composition NANMO (blue). It is remarkable that replacing half of the nickel with iron leads to a significant drop of both conductivities (NANMFO, cyan). A further replacement of the remaining nickel with more iron seems to increase both conductivities (NAFMO, green). Replacing Al with Fe (NMFO, purple) again leads to a reduced conductivity for both mechanisms. These intrinsic properties are apparently related via a more complex correlation. Substitution of TM in the cathodes crystal framework can influence the conductivity via several effects [76]. As already described in Chapter 2.3.4 *Substitution of elements in the crystal framework* substitution may cause a change in the band gap and thus affecting the electronic conductivity. Different ionic radii of substitution elements may expand or shrink the lattice parameter and thereby change ion diffusion. With the four steps of iron content variation from zero (NANMO) to 1/3 in $Na_{0.6}Fe_{1/3}Mn_{2/3}$ (NMFO) are perhaps not all changes visible and understandable.

In the work of Walczak et al. from 2022 [73] with layered sodium oxides $Na_{0.67}Fe_{1-y}Mn_yO_2$ an increase of the Manganese content from y = 0.4 to 0.8 lead to an increase of the total electrical conductivity by two orders of magnitude. A completely different crystal system was presented in the other work of Walczak et al. from 2019 [77] with Sodium-Nasicon-Phosphates $Na_3Fe_{2-y}Mn_y(PO_4)_3$. It is worth mentioning that with an increase of Manganese content from y=0 to 0.4 the conductivity first dropped, then increased with a local maximum and then decreased again, similar to the data presented in this study. While the iron-free composition NANMO had the highest measured σ_i, if this composition would be neglected and one could speak of a local maximum of both conductivity processes with the medium iron content in $Na_{0.6}Al_{0.11}Fe_{0.22}Mn_{0.66}O_2$ (NAFMO, green in Fig. 5.16). However one also needs to take into account that the visible internal texture of the pellets differs with the chemical composition. In Figure 5.11 there are more gaps between the particles inside the NMFO-pellet visible than inside the NAFMO-pellet. Also NANMFO exhibits a higher porosity, while NAFMO shows the lowest porosity. This reduced contact certainly is another reason for the lower conductivity, when comparing the similar materials NMFO & NAFMO or NANMFO & NANMO, respectively.

Further research is required to optimize the materials in terms of conductivity with different sinter temperatures and durations. Not only will this change their porosity and the intra-pellet contact via sinter necks but also the crystal structure. It can be expected

that especially for the two iron-rich materials NAFMO and NMFO a change in the range from 850 °C to 1000 °C should be visible, since a change of the secondary particle porosity from 48 % to 22 % and from 39 % to 12 % respectively was observed (see Chap. 5.1 *Material Properties*). EIS measurements of pellets from the four layered oxides in this temperature range would complement the work presented in the other Chapters 5.1 and 5.4 about particle morphology, crystal structure and electrochemical performance after different sinter temperatures. For now the data for σ_j $(j = e, i)$, sintered at $T_s = 950$ °C must be used as reference point for the other sintering temperatures.

The influence of different textures and porosity within the pellets should be reduced for an easier interpretation, when comparing different compositions (as seen in Fig. 5.11). This could be achieved by applying higher pressing force in the pellet preparation and higher/longer sinter temperature and duration. Another possibility for further understanding could be achieved with density functional theory (DFT). Band structures and ionic transport mechanisms can be calculated as numerical solution of the Schrödinger equation and in the recent years DFT calculations improved the understanding of battery materials [78].

5.3 In situ X-ray diffraction

In situ XRD analysis was performed to investigate the structural change in the crystal lattice during cycling. Some crystallographic properties of synthesized P2-type layered oxides were discussed in Chapter 5.1.4 *Crystal structure* of the section *Material properties*. As a reminder, the here presented cathode materials crystallize in the hexagonal space group $P6_3/mmc$. The transition metals (TM) create layers with sodium ions in-between. A P2-type crystal structure is shown on the left-hand side in Figure 5.17.
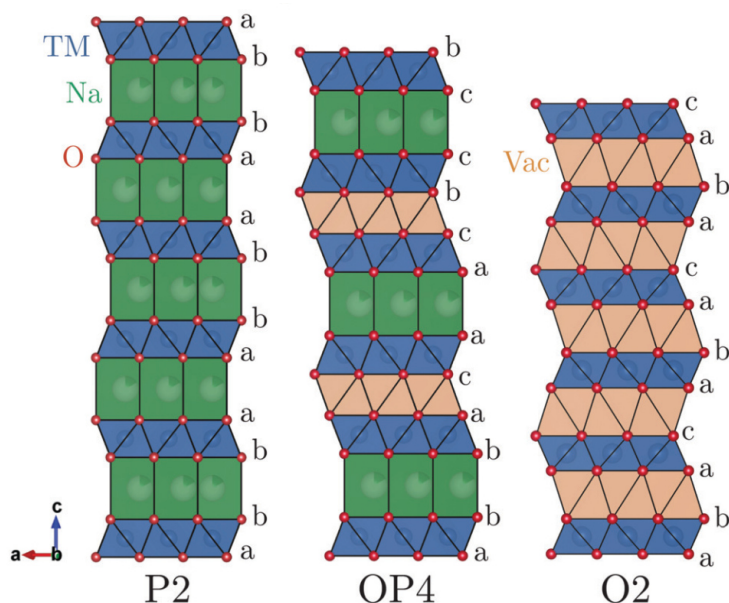
Figure 5.17: **Phase transition:** When sodium is removed from the TM-layers (charging) the P2-type structure transits to O2-type, with OP4 as an intermediate. The letter P indicates a prismatic and O an octahedral environment of the sodium sites and vacancies between the layers. The numeral represents the number of different stacking sequence of oxygen layers (taken from Somerville et al. [6]).

Also shown are two related layered oxide types, OP4 and O2. During electrochemical cycling a P2-type structure can evolve via OP4 into a O2-type. Some characteristics and details of this phase transition are described in Chapter 2.3 *Layered Oxides* of the *Theory*-section. The process is shortly described in the following for a better understanding of the in situ XRD data of the current section.

In general, P2-type layered oxides show severe change of lattice parameters during charging. When charged beyond 4.0 V vs. Na$^+$/Na phase transitions can occur [6,79]. The terminology in literature for the evolving phase is „Z-phase " [6]. This term usually describes the coexistence of several phases. The sketch in Figure 5.17 shows how the P2-phase evolves into OP4- and O2-phase (taken from Somerville et al. [6]). Between the TM-layers the sodium ions can be (de)-intercalated, which is the base of the ionic

storage mechanism. The name P2-type originates from the prismatic sites of Na^+ ions between the layers. The number indicates two different TM-layers (a-b and b-a, not to be confused with the lattice parameters). Upon removal of sodium ions from the prismatic sites of P2, vacancies with an octahedral environment are created between the P2-layers. This transformation is fluent until the OP4-phase, consisting of alternating octahedral and prismatic sites and in the same quantity, is present. Octahedral and prismatic sites are each enclosed by their individual layer stacks, so four in total (OP4). Further sodium removal results in a pure O2-type structure. A 2-phase transition mechanism between these three structure types leads to coexisting phases and the appearance of x-ray reflections from several phases in one pattern [6].

These phase transitions, the expansion and shrinkage of lattice parameters are one degradation mechanism of layered oxides. Different chemical compositions and doping elements influence this mechanism [42].

5.3.1 Measurement and qualitative interpretation

All of the four layered oxides of this work were investigated. Their chemical composition is listed here as a reminder, ordered from highest Ni-content to highest Fe-content:

- NANMO $Na_{0.6}Al_{0.11}Ni_{0.22}Mn_{0.66}O_2$

- NANMFO $Na_{0.6}Al_{0.11}Ni_{0.11}Fe_{0.11}Mn_{0.66}O_2$

- NAFMO $Na_{0.6}Al_{0.11}Fe_{0.22}Mn_{0.66}O_2$

- NMFO $Na_{0.6}Fe_{1/3}Mn_{2/3}O_2$

The final sintering temperature for the materials, presented here was $T_S = 950\,°C$ (in Chap. 5.1 & 5.4 several T_s were investigated). The in situ XRD measurements were performed on coin cells. Thicker cathodes than for electrochemical cycling were prepared to achieve more intensity from the active material (see Chap. 4 *Experimental*). It needs to be noted that these thicker electrodes were less efficient in terms of electrochemistry. The cathodes of the in situ measurement delivered only 78 % to 88 % of the specific capacities Q_{spec} presented in Chapter 5.4. XRD measurments were performed during the second cycle [02] with a current of C/10 (after formation with 1C, analogous to electrochemical cycling). Mo-$K_{\alpha1,2}$ radiation was used as X-ray beam.

Contour plots of in situ X-ray data and cell voltages are shown in Fig. 5.18. The reflections are labelled with the corresponding *hkl*-markers. Besides the P2-phase, additional reflections originate from the aluminium current collector (marked with +) and the sodium anode (marked with *). Another reflection occurs due to X-ray scattering on the XRD device (marked with #). These reflections are in general stationary and do not change during cycling. In contrast to these stationary reflections the positions of signals from the P2-type layered oxides shift as a result of lattice volume change.

---

[02] Due to problems with a clean refinement of lattice parameters for NMFO, a thicker electrode sheet was used for the measurement and in this case the 3rd cycle was used for refinement.
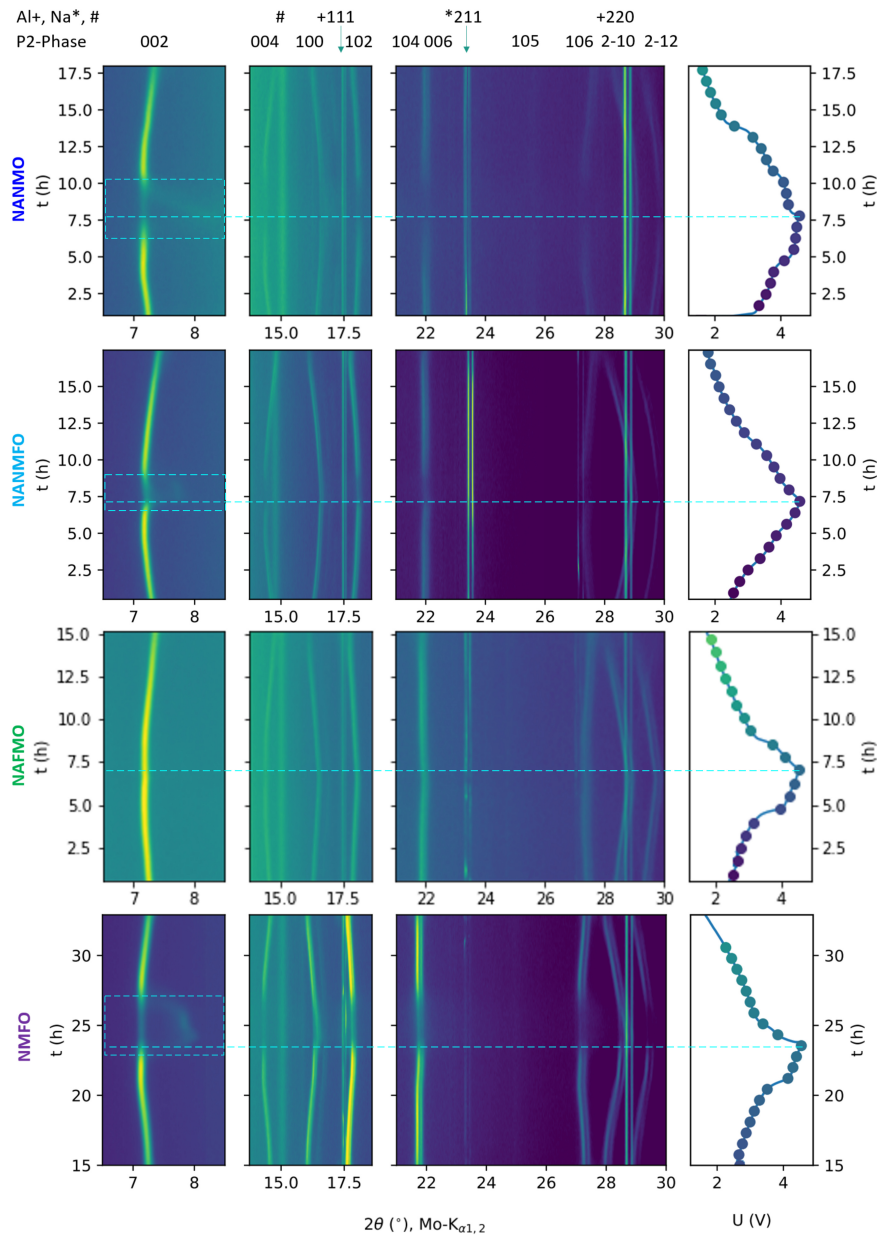
Figure 5.18: **In situ XRD:** Evolution of x-ray reflections of the P2-type structure during electrochemical cycling. The contour plots show the reflection intensity with the scattering angle 2θ on the x-axis and measurement time on the y-axis. On the right-hand side the charge-discharge curves with the voltage as x-axis are plotted. All materials exhibit shifts in reflections, corresponding to change of lattice parameters. A phase transition in the high voltage region beyond 4.3V is visible for NANMO, NANMFO and NMFO.

During charging the main reflection 002 (beginning slightly different for different materials: $2\theta \approx 7.3°$) and the 004 reflection ($2\theta \approx 14.6°$) of all materials are shifted to lower angles (contour plots in Fig. 5.18). This is consistent with an increase of lattice parameter c (or lattice-parameter c) [6]. At the same time the 100-reflection is shifted to higher angles, which is consistent with an decrease of the lattice parameter a.

A Z-phase development at high voltage is visible for NANMO, NANMFO and NMFO. The upper limit of 4.6V is marked with a dashed line. The intensity of the 002 reflection prominently decreases into a diffuse region (Z-phase development, dashed rectangle). The diffuse region is not centred with the highest potential of 4.6 V. A delay might occur due to sluggish Na^+-ion kinetics in layered oxides [80]. The 002 reflection reappears during discharge again, demonstrating a reversible transition. It is not distinctively clear where to mark the beginning and end of the Z-phase, the dashed rectangles mark one possible option: The beginning of the intensity drop of the P2-002-reflection. For NANMO this occurs at 4.3 V, for NANMFO at 4.36 V and for NMFO at 4.38 V.

A strong decay of the 002 reflection intensity is visible for NANMO and NMFO (to approx. 14 % of max.) and broad area of diffuse region. In case of NANMFO the 002 reflection intensity is less strong reduced (to approx. 29 % of max.) and a less broad diffuse area is visible. However, the broadness of the diffuse region might be false interpreted. Even with similar theoretical capacities and the same C-rate the different cathode materials differ in their experimental capacity. This leads to a different time scale for the individual materials (y-axis in Fig. 5.18). A closer inspection of the experimental capacities will be presented in Chapter 5.4 *Electrochemistry*. An interpretation of how much the P2-phase has transitioned will be analysed in the following Chapter 5.3.2 *Rietveld refinement*.

NAFMO did not show a development of a Z-phase in this setup. A transition directly into the O2-phase is also possible as presented by Somerville et al. [6], but there was also no evidence for an O2 development either. To make sure this is not an incorrect measurement, it was repeated 4 times with cathodes from two different electrode sheets. It needs to be noted that in the 2nd cycle (1st with C/10) the NAFMO cathode delivered a specific capacity Q_{spec} of only 70 % of the value obtained with the thinner electrode sheets (see Chap. 5.4). The charge-discharge process was not as complete as for a thinner cathode and hence reducing the chance of a phase transition. However, also in the third cycle (the 2nd with C/10), where 83 % of the expected capacity for NAFMO were obtained, no Z-phase was observed. Approx. 80 % (capacity of the thinner cathodes) was also achieved with the other three CAMs, which showed a phase transition, despite this reduced capacity. It also needs to be pointed out, that NAFMO showed the highest amount of Fe^{4+} of the three iron containing CAMs (see. Chap. 5.1.6 *Mößbauer spectroscopy*). This was achieved with even thicker electrodes than used here. A phase transition in NAFMO might be prevented if only a small amount of Fe would be oxidized into the tetravalent state. However this seems not to be the case, since the measured amount of Fe^{4+} in NAFMO cathodes was even higher than in NMFO. To understand more about the material effect of the absence of a Z-phase in NAFMO, future work could investigate an in situ experiment with even smaller C-rates of C/20 and ex situ

measurements on charged cathodes could be added.

The reduced performance with thicker electrodes is simply due to the fact that these cathodes were not yet optimized in terms of calendering and amounts of binder and conductive carbon in the cathode sheet. A thickening of cathodes increases the intensity to measure during an in situ XRD but leads also to a higher overall resistance of the cathode and less performance. This was observed for all CAMs.

A quantitative interpretation of the above described observation will be given in Chapter 5.3.2 *Rietveld refinement*. A short qualitative interpretation is summarized in the following.

When sodium is removed from the layers during charging and the 002 & 004 reflections are shifted toward smaller angles this can described as a increase of the *c*-parameter of the lattice. Half of the *c*-parameter can be understood as the layer to layer distance between which the ions can be intercalated and removed [6]. Imagining the sodium ions as simple spheres one would expect a decrease of c during removal of Na^+. However, the opposite is the case: The layer to layer distance increases because the Na^+-ions used to screen the repulsive force between the layers and therefore the distance is increased upon removal [6].

In contrast to that a shift of the 100 reflection to higher angles implies an decrease of the *a*-parameter and therefore a decrease of the in-plane TM-TM-distance [6]. This distance gets shorter due to the shorting of TM-oxygen bonds during oxidizing of TM when sodium is removed.

When a Z-phase is formed it creates stacking faults in the P2-type structure [6]. This leads to a reduction of the long-range order in the crystal and can be observed as intensity drop of the declining P2-phase (diffuse region in Fig. 5.18). In the measured diffractograms the Z-phase development starts well beyond the 4.0 V to 4.1 V vs. Na^+/Na reported from literature [6, 79]: At around 4.3 V a drop of P2-phase intensity was observed. One reason for that is the before mentioned thicker electrodes. With slow sodium kinetics and high resistance the thick cathode may cause a delay. Another reason is that C/10 was used as current, a compromise of short measurement time and slow charging/discharging. Somerville et al. [6] used only a third of this current. With longer measurement times the slow ion kinetics are not problematic and a delay less visible.

A further delay of the Z-phase development in case of NANMFO and NMFO can be related to their chemical composition. Both contain iron, which is redox active at higher voltages than nickel is. In Chapter 5.1.6 *Mößbauer spectroscopy* this difference was explained. The high-voltage redox pair of Ni^{4+}/Ni^{3+} of layered oxides can be expected between 3.53 V and 3.69 V [66], while the oxidation of Fe^{3+} to Fe^{4+} is located around 4.1 V [67]. This means Fe containing materials allow further removal of sodium only at higher voltages (corresponding to Fe^{4+}/Fe^{3+} redox reaction) and the Z-phase evolution is thereby shifted to higher voltages with increasing iron content: 4.3 V, 4.36 V and 4.38 V for NANMO, NANMFO and NMFO respectively.

5.3.2 Rietveld refinement

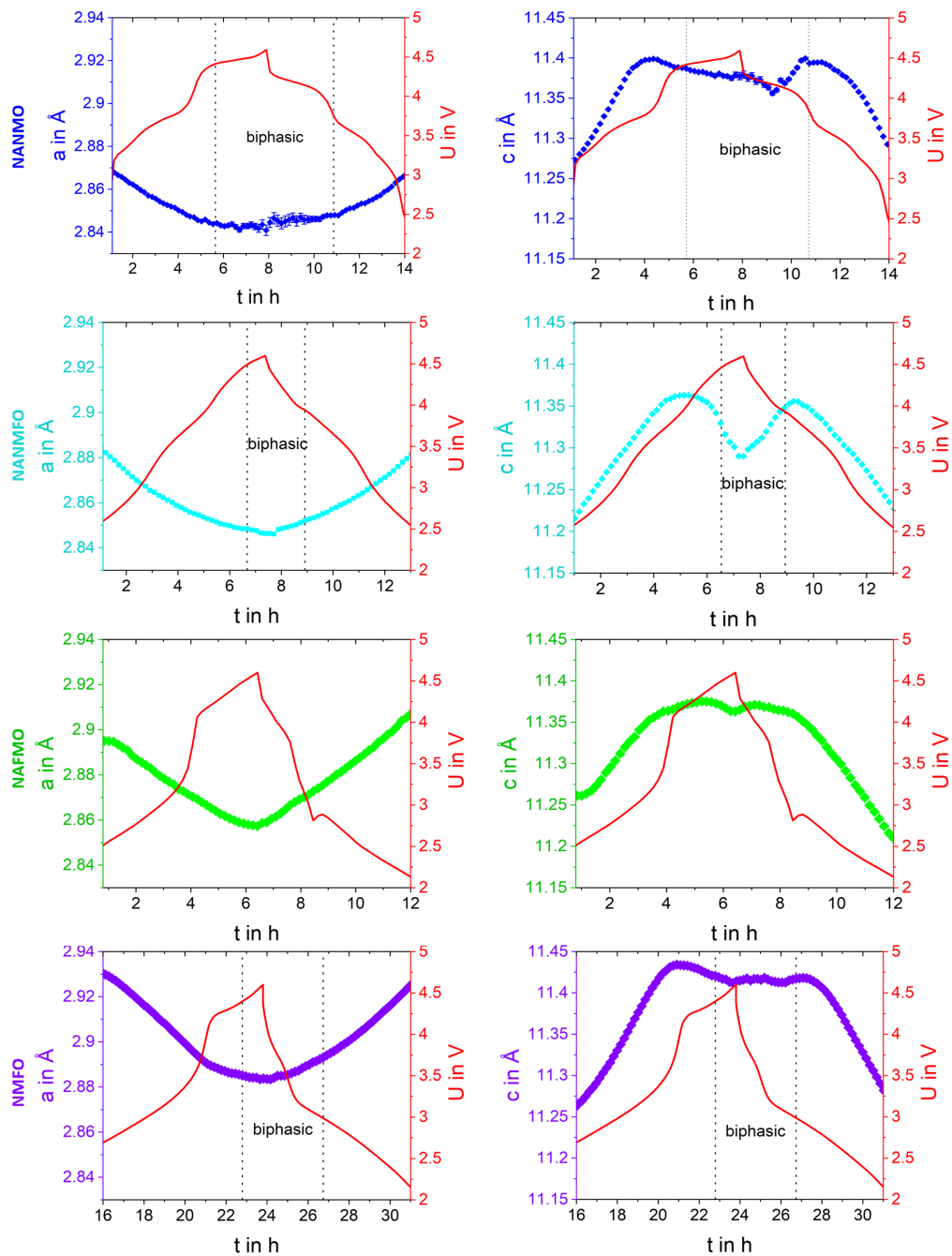

Figure 5.19: **Refined parameters:**   The *a*-parameter is shown on the left-hand side and the *c*-parameter on the right-hand side. The cell potential is shown in red. It can be seen how the lattice contracts along the *a*- and expands along the *c*-axis during charging (vice versa during discharging). At high potential values beyond 4.3 V, the phase transition is marked as biphasic region.

For a quantitative interpretation the measured XRD patterns were compared to a theoretical line pattern, which was refined until it matched the measured data. This approach is known as the Rietveld method and gives specific values for crystallographic properties. The software *jEdit* and *Topas Version 6* were used for the calculation of refined data. For the fit a pattern for a P2-type structure (space group $P6_3/mmc$), Al ($Fm\bar{3}m$) and Na ($Im\bar{3}m$) were used. In the higher voltage region, as soon as additional reflections were visible, a pattern for the OP4-phase ($P6_3/mmc$) was added.

In a hexagonal lattice the *a*-parameter is identical to the *b*-parameter. The results for the refined lattice parameters are shown in Figure 5.19 with *a* on the left and *c* on the right. The y-scale for *a* and *c* of the individual cathode active materials (CAM) is kept the same for an easy direct comparison.

As starting point of the refinement at the beginning of the cycling the values from the ex situ XRD measurements (see Tab. 5.4 in Chap. 5.1.4) were used. At the beginning of the cycling the values for *a* and *c* are mostly similar to the values obtained from the ex situ measurements: *a* increases from highest nickel content to highest iron content. The ex situ values for *c* also increased from high nickel to high iron. In the in situ measurements some deviations from the ex situ data are visible. This deviation of both lattice parameters might be related to minor lattice change induced via cell assembly and pre-cycling with 1C. So the difference in lattice is of electrochemical nature. Something similar has also been reported in literature [81].

Figure 5.19 shows how the previously described decrease of *a* and increase of *c* evolves for the four materials. For NAFMO the values for *a* change almost linearly, while for the other three materials with phase transitions a broad minimum at high voltage is shown. The phase transition creates some „noise" for the refined values of the *a*-parameter or small steps which deviate from a smooth curve. But this disturbance is rather small, indicated by the error bars, which are only visible but still insignificant for NANMO. Note that the shown „error bars" are in reality estimated standard deviations, shown as error bars. For *c* the increase stops shortly before the biphasic region and then drops again in the middle of the biphasic region. The onset can even be seen for NAFMO, where no phase transition occured. A similar behaviour was reported in literature of lithium based layered oxide. The *c*-parameter consists of two heights: The height of the Li-O and the TM-O slabs [82]. Kondrakov et al. [82] measured that the TM-O height decreased during the charging process, while the Li-O height at the beginning was increasing, therefore moderating the decrease of the other height. After the lithium amount was further reduced in the high voltage region both heights decreased which results in a drop of the *c*-parameter. A similar effect might be the cause of the decline of *c* in the high voltage region, where more sodium is removed.

The changes of both lattice parameters are summarized in table 5.8 In case of NANMO and NANMFO the change in lattice parameter *c* is similar while for NANMO the smallest change in *a* was measured. For both materials the changing in parameters *a* and *c* is of the same order of magnitude but shifted due to their different onsets at $t = 0\,\mathrm{h}$ (beginning). Both materials are similar in their pristine crystal structure and morphology (see material properties in Chap. 5.1.4 and 5.1.1).

63

Table 5.8: **Refined lattice parameters:** As starting point (a_{start}, c_{start}) was $2.6\,\mathrm{V} \approx$ OCV chosen. The minimum of a and the maximum fo c was visible at the upper voltage limit $UL = 4.6\,\mathrm{V}$. These values were taken from Figure 5.19.

	a_{start} in Å	a_{min} in Å	c_{start} in Å	c_{max} in Å
NANMO	2.869	2.841	11.27	11.40
NANMFO	2.882	2.846	11.22	11.36
NAFMO	2.895	2.857	11.26	11.38
NMFO	2.933	2.884	11.25	11.43

For NAFMO without a Z-phase development there is the smallest change for c and a moderate change in a. The strongest change of both a and c was measured for NMFO. Since the layer to layer distance corresponds to half of the c-Parameter, the maximal change of this distance can be assigned to NMFO. It can be seen that for all cathode materials the lattice change is mostly completed before the biphasic region appears in the diffractograms.

A receding intensity of the P2-phase indicates the weight percent of P2 in the active material is reduced as well. It needs to be noted that the P2-intensity is already decreasing before reflections of the new phases are visible. At this point the P2-phase seems to be already undermined by a structural change. The continuous changing amount of P2 needs to be considered in the following when the sodium occupancy is calculated. The lowest amount of P2 was calculated in weight percent for NANMO 57%, for NANMFO 67% and for NMFO 78% according to refinement with P2 and OP4 structure in the high voltage region. With higher iron content more of P2 remained in this voltage window, which might be related to the different potentials of the redox pairs of Ni and Fe, as mentioned before.

As a reminder from *Theory*-section about layered oxides (Chap. 2.3), there are two possible sodium sites between the layers of a P2-type structure: Na_1 and Na_2. Neighbouring sites cannot be occupied at the same time which leads to an ordering of vacancies (superstructure). The reordering of vacancies during electrochemical cycling creates diffusion barriers and becomes visible in distinct voltage plateaus [31]. Introducing substitutional elements into the framework can reduce these energy barriers. An observation on how these two sites are emptied during charging gives information about the diffusion barriers.
Refinement from XRD data of lithium positions is difficult in general, since Li has only a few electrons (low electron density), so there is low interaction of the incident X-ray beam with Li. On the other hand the X-ray beam can notably be scattered more strongly on a higher electron density, which is the case for sodium. This adds the possibility to gain values for occupancy on the two sodium sites. Figure 5.20 shows the refined occupation numbers for the Na_2 and Na_1 sites. The starting values can be compared to the refined ex situ XRD values from Table 5.4 in Chapter 5.1.4. For all materials there
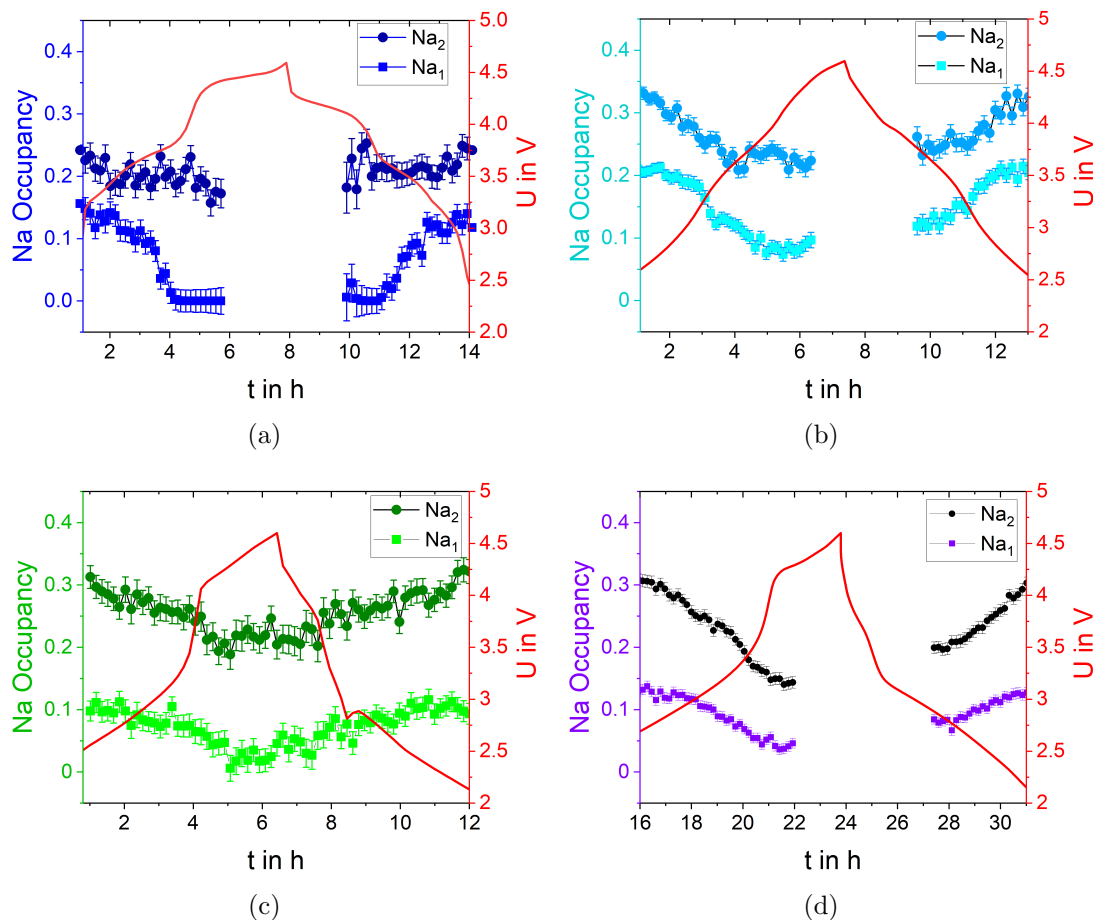
Figure 5.20: **Sodium occupancy:** Refined occupancies for the two possible sodium positions in a P2-type layer. The cathode materials are sorted accordingly to the colour code from highest nickel content to the highest iron content: NANMO (a), NANMFO (b), NAFMO (c) and NMFO (d). In the biphasic region a clean refinement was not possible. The cell voltage is shown in red. During charging sodium gets removed from the layers and both sodium sites get depleted (vice versa for discharging).

is a higher occupation on the Na_2 site, which is in agreement with the ex situ data. However, the refined values for both sodium sites are lower in case of the in situ data. For Na_1 and Na_2 the ex situ data provided values between 0.2 to 0.4, which added up to about 0.6 of sodium content in total. This was in agreement with the values targeted in the synthesis and supported from chemical analysis with ICP-OES. The reason why a lower amount was measured here might be due to the precycling with 1C (which was necessary for better cycle stability with the thicker cathodes). This first cycling with a fast rate changes the amount of sodium to begin with at the second cycle. It also needs to be noted that the even with thicker electrodes the signal of the P2-structure with a laboratory XRD equipment still provides a moderate intensity (as compared to a syn-

65

chrotron radiation source for in situ XRD). This bares some difficulties and uncertainties to the refinement in general and especially to the sodium occupancy (also indicated with stronger error bars in Fig. 5.20). At the onset of the biphasic region, where the intensity of the P2-reflections becomes diffuse and the OP4 signal is not distinctive, the delicate refinement of the Na sites is no longer possible. Therefore the redefined Na sites in the biphasic region were not taken into account.

What still can be observed is the trend in the occupancy curves. The same trends can be observed for both charging and discharging of the individual materials, supporting each other. For NANMO in Fig. 5.20 (a) the occupancy of Na_2 appears to be almost stable and is just slightly decreasing during charging. On the contrary, the Na_1 position is depleted a bit quicker at the beginning already and after ca. 3.5 h the occupancy drops to zero. Vice versa during the discharge process when sodium sites are filled again. This means the depletion and filling of the Na_1 position is favoured over the Na_2 position.

For NANMFO (b) and NAFMO (c) the occupancy curves of both sites exhibit a similar slope and rise and fall at the same time. With the precision of the presented method a favoured process could not be identified. In case of NMFO (d) the occupancy curves for Na_2 exhibits a steeper slope. Here the diffusion of Na^+ ions from the Na_2 is favoured over Na_1, but less distinctive as for NANMO (a).

This effect can best be understood when comparing NANMO and NANMFO with each other. As presented by Wang et al. [31] less vacancy ordering can be introduced by substitution with another TM metal. Less ordering means a lower activation energy barrier for the ion hopping between the two sites Na_1 and Na_2 and is visible through the absence of distinctive plateaus for NANMFO. A hopping from neighbouring sites enhances the overall sodium diffusion. The change of the occupancy of both sodium sites at the same time for NANMFO supports this assumption. The activation energies E_{A_i} for the ionic hopping mechanism were investigated in Chapter 5.2 *Conductivity properties*. The impedance spectroscopy data is summarized in table 5.7. It was found that NANMFO exhibits a lower activation energy $E_{A_i} = 0.22\,\text{eV}$ as compared to NANMO with $E_{A_i} = 0.30\,\text{eV}$. Even though the difference is small, it supports the interpretation of the sodium vacancy ordering. This can be understood as a reason for some different electrochemical behaviours of NANMO and NANMFO which are presented in the Chapter 5.4 *Electrochemistry*. In case of a solid-solution-reaction (absence of distinguishable plateaus), no vacancy-ordering of the superstructure is necessary. Faster ionic transport between interlayers under sodium intercalation is the result, which can be observed as better performance at higher rates [31]. For NAFMO also a relatively small ionic activation energy of $E_{A_i} = 0.19\,\text{eV}$ was found with EIS. This is also in agreement with less sodium vacancy ordering as compared to NANMO and NMFO. For the latter $E_{A_i} = 0.38\,\text{eV}$ was measured.

To understand the electrochemical cycling in Chapter 5.4 one needs to keep in mind the other difference between NANMO and NANMFO which became clear in current chapter: In case of NANMFO the phase transition begins at higher cell potential and the biphasic region covers a smaller area in the plots of Figure 5.18 and 5.19. In the

following chapters it is presented how the cycling stability of the cells is changed with different upper voltage limits. A reduction of the upper limit in case of NANMFO has a different influence on the cycling stability than it has for NANMO.

5.4 Electrochemistry

The electrochemical properties of the cathode materials were tested in half-cells. Electrode sheets, electrode discs, electrolyte and cells were prepared as described in Chapter 4 *Experimental*. SEM images of cross sections from these electrodes were shown in Chapter 5.1.2 *Cathode morphology* to reveal their porous structure. In the following the electrochemical performance of the synthesized layered oxides is shown. Expected redox processes can be assigned in the charge-discharge-curves. A comparison of different sintering conditions and voltage windows is presented as part of their individual optimization.

5.4.1 First cycles and redox reactions

In this Chapter all cathode active materials (CAM) presented underwent the sintering procedure at $T_s = 950\,°C$, as before in the chapters about in situ XRD, conductivity properties and Mößbauer spectroscopy. This can be understood as the starting point of the presented work. The first investigated chemical composition of NANMO was taken from the work of Hasa et al. [36], where the heat treatment was done at $1000\,°C$. The influence of different sintering temperatures T_s on the cycling behaviour can best be seen in Chapter 5.4.4. The average open circuit voltages (OCV) observed on half cells with the here presented materials after were 2.74 V, 2.72 V, 2.79 V and 2.68 V for NANMO, NANMFO, NAFMO and NMFO respectively. Figure 5.21 shows charge-discharge-plots of the first two cycles in the range of 1.5 V to 4.6 V, C/20 and C/10 respectively. At a certain point in the presented work 1C was used in the first cycle (not shown here, see appendix), which may seem unconventional but as explained in Chap. 4 *Experimental* it increased the success rate of built batteries. This behaviour was attributed to the broad voltage window and the electrolyte not yet optimized. Side reactions may occur for the SEI formation on the sodium metal anode which could cause problems [83]. 1C at the beginning was chosen as pragmatic solution. Also, already mentioned, a long time test with 200 cycles showed no difference in cell performance between 1C at first cycle and without.

Theoretical capacities Q_{theo} and therefore the C-Rates were calculated with Faraday's law

$$Q_{theo} = \frac{F \cdot z \cdot m}{M} \cdot \frac{1}{3.6} \tag{9}$$

where F is the Faraday constant, z is the charge number of the involved charge carriers, m the mass and M the molar mass of the material. The factor of 1/3.6 is needed to receive the desired unit of mAh/g. According to Hasa et al. [36] $z = 0.6$ was based on the contained sodium in the cathode to take the sodium deficiency into account ($Na_{0.6}TMO_2$). Sorted from highest nickel to highest iron content, this results in theoretical capacities of $Q_{theo}(\text{NANMO}) = 164\,\text{mA h g}^{-1}$, $Q_{theo}(\text{NANMFO})=165\,\text{mA h g}^{-1}$, $Q_{theo}(\text{NAFMO})=165\,\text{mA h g}^{-1}$ and $Q_{theo}(\text{NMFO})=159\,\text{mA h g}^{-1}$. This capacity could
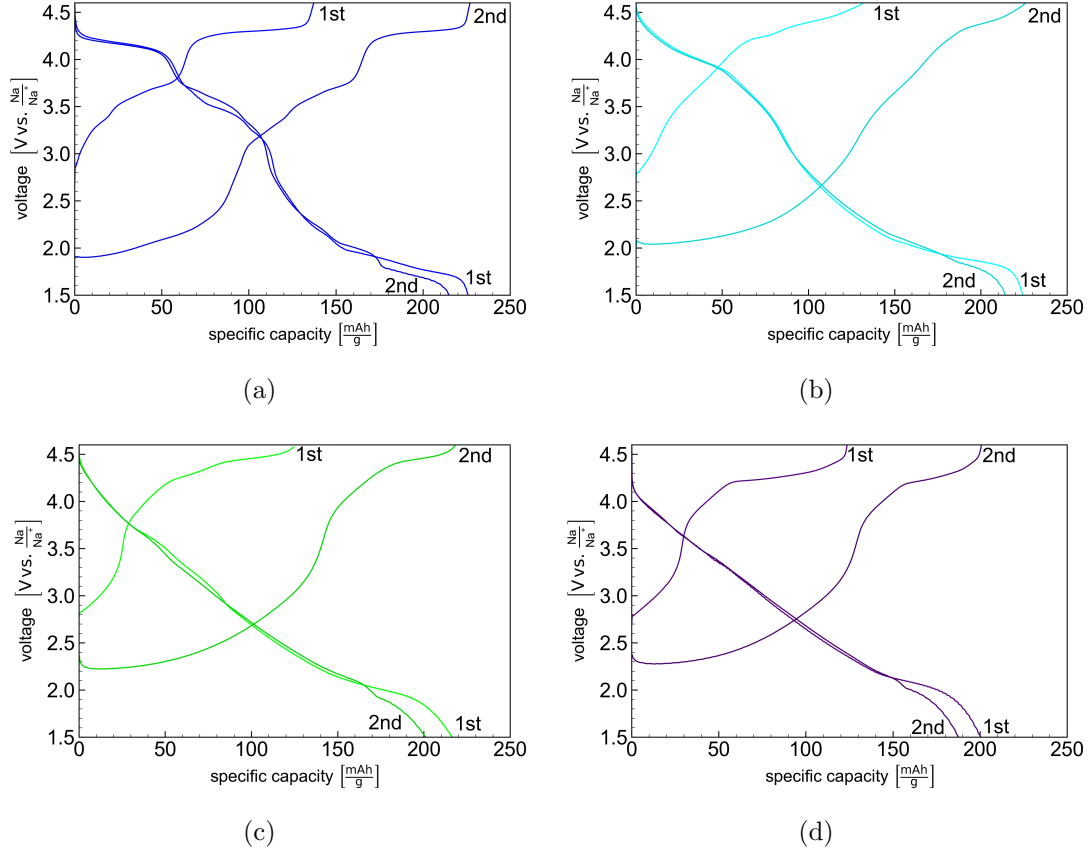
Figure 5.21: **Charge-Discharge-Curves:** The first two cycles of NANMO (blue (a)), NANMFO (cyan (b)), NAFMO (green (c)) and NMFO (purple (d)). Different C-rates were used as follows: C/20 and C/10.

be reached in an ideal full cell. Effectively, experimental capacities are lower in general due to a incomplete electrolyte penetration and therefore dependence on slow ion kinetics [5]. Smaller currents (lower C-rates) are one possibility to endure slow kinetics and still reach higher capacities [31] but for an application this is not always possible.

With this information one can understand the cycling behaviour in the first two cycles displayed in Figure 5.21. During the first charge cycle with C/20 the amount of sodium taken from the cathode cannot exceed $z = 0.6$ given from the chemical formula of the pristine materials. During the first discharge, sodium from the anode is inserted into the cathode. Since the cut off voltage $1.5\,\mathrm{V}$ is considerably below the OCV, additional sodium-ions from the Na-metal-anode are loaded into the sodium deficient P2-layered structure. This results in a capacity above the theoretical value, because now $z > 0.6$. The achieved specific capacity Q_{spec} in the first discharge cycle with C/20 can be used in equation 9 to calculate the amount of intercalated sodium equivalent z. Ordered from highest nickel to highest iron content this results in:

- NANMO $Na_{0.6}Al_{0.11}Ni_{0.22}Mn_{0.66}O_2$: $Q_{spec} = 226\,\mathrm{mA\,h\,g^{-1}} \rightarrow z = 0.83$

- NANMFO $Na_{0.6}Al_{0.11}Ni_{0.11}Fe_{0.11}Mn_{0.66}O_2$: $Q_{spec} = 224\,\mathrm{mA\,h\,g^{-1}} \rightarrow z = 0.82$

- NAFMO $Na_{0.6}Al_{0.11}Fe_{0.22}Mn_{0.66}O_2$: $Q_{spec} = 216\,\mathrm{mA\,h\,g^{-1}} \rightarrow z = 0.79$

- NMFO $Na_{0.6}Fe_{1/3}Mn_{2/3}O_2$: $Q_{spec} = 200\,\mathrm{mA\,h\,g^{-1}} \rightarrow z = 0.73$

The ability to intercalate additional sodium into the P2-type layer demonstrates its sodium deficiency but also its thermodynamical stability [36]. A synthesis with a sodium content of $x < 0.7$ in the formula Na_xTMO_2 would result in an O3-type layered structure instead of the presented P2-type [30] (see also Chap. 2.3 *Layered Oxides*). Increasing the sodium content inside the cell would only change P2-type to P'2-type, that is from hexagonal to orthorhombic phase [36].

In the second cycle one can see the beginning of a rate-capability-test with C/10 which will be shown and discussed in the following chapters. After the formation cycles with C/20, the values for charge and discharge capacity of cycle number three and the following ones are more similar to each other. Now the charge capacity is always slightly bigger than the discharge capacity, and not vice versa as before. This narrow difference is described as Coulombic efficiency with a value below but ideally close to 100%.

With the plots in Fig. 5.21 one can also estimate the regions of specific redox reactions of the transition metals in the layered structure. In case of NANMO (Fig. 5.21 blue) it is the simplest due to distinctive voltage plateaus. Also, NANMO can be compared directly to the cathode material in the work of Hasa et al. [36]. Aluminium is electrochemically inactive in this voltage range and does not contribute to the capacity [36].

After the assembly with the average OCV of 2.74 V the cathode material exhibits oxidation states of Mn^{4+}, Ni^{2+} [36]. At low voltages (high sodium content in the cathode) around 2.0 V, the redox reaction of Mn^{4+}/Mn^{3+} is located [36]. Since all materials contain manganese, it can be assumed that for all CAMs this redox process should be present around 2.0 V. During the low voltage redox process of manganese, the Jahn-Teller-effect may occur as well where Mn^{3+} induces lattice strain and could lead to a phase transition into the before mentioned P'2 phase [36, 84].

Two of the presented cathode materials contain nickel, their charge-discharge-curves can be seen at the top in Fig. 5.21 (NANMO and NANMFO). For them, the redox processes of Ni^{3+}/Ni^{2+} and Ni^{4+}/Ni^{3+} can be expected around 3.1 V to 3.38 V [36, 68] and 3.53 V to 3.74 V [66, 68] respectively. Especially for NANMO, voltage plateaus starting at 3.1 V and 3.54 V can be seen. For NANMFO, the curvature is smooth and without distinctive plateaus is difficult to see the start and beginning of the redox reactions. The values from literature ([36, 66, 68]) can be understood as an approximation. The exact position depends on the present transition metals and their amounts, or rather, their ratios.

In case of NANMFO, NAFMO and NMFO iron was used as substitutional element for nickel. The three iron containing cathode materials were investigated with Mößbauer spectroscopy as presented before in Chapter 5.1.6. The pristine materials showed only

evidence of Fe^{3+}, which means that divalent Ni^{2+} in the pristine material was substituted with trivalent iron. The materials must however keep an overall charge neutrality. As a result the iron containing cathode materials must exhibit some amount of Mn^{3+} at the beginning of cycling (OCV) to compensate the charge. When charged to 4.6 V and ex situ Mößbauer measurements were carried out, clear signals of the Fe^{4+} doublet became visible. This is supported by the achieved capacities in Fig. 5.21. If the redox process of Fe^{4+}/Fe^{3+} would not be active in the given electrochemical window (ECW) the resulting capacities $Q_{Fe^{3+}}$ would be much lower, namely for the second charging cycle (additional sodium considered) NANMFO $Q_{Fe^{3+}} = 213 \, \text{mA h g}^{-1}$, NAFMO $Q_{Fe^{3+}} = 183 \, \text{mA h g}^{-1}$ and NMFO $Q_{Fe^{3+}} = 175 \, \text{mA h g}^{-1}$. These values are all exceeded by the second charging cycle. Demonstrated by both electrochemical cycling and Mößbauer spectroscopy, the redox activity of Fe^{4+}/Fe^{3+} shows that iron is indeed suitable to replace nickel. However, from literature it is known that Fe^{3+} generally needs a higher cell voltage to be oxidized into the tetravalent state than its nickel counterpart (beyond 3.53 V for Ni and 4.1 V for Fe [66, 67]). The higher necessary voltage is also supported by the measured Mößbauer spectra (Fig. 5.9 in Chap. 5.1.6) where after being charged to 4.6 V the Fe^{3+} doublet was still clearly visible. This can be problematic in a battery cell. While higher cell voltages are a benefit for energy density however electrolyte components and battery materials are in general less stable at relatively high and low voltages (border areas of ECW) and suffer from side reactions [19]. Alternatively smaller C-rates ($<$C/20) and longer duration time at the upper voltage limit could also oxidize more of the remaining trivalent iron, but this is also problematic for an application.

5.4.2 Influence of the chemical composition on capacity

Here, the electrochemical behaviour of the four CAMs sintered at 950 °C are compared with each other. In Figure 5.22 the delivered discharge capacity for the window 1.5 V to 4.6 V is shown for 100 cycles (without the formation with a rate of 1C at the beginning). Different C-rates demonstrate the rate-capability. After that, a long term cycling with 1C shows the stability and degradation of the different materials. NANMO and NANMFO show similar capacities during the rate-test. With moderate C-rates of 0.5 to 5C, NANMFO delivers more capacity. In the long term cycling also a moderate rate of 1C was applied. Here, NANMFO also shows more stable cycling behaviour than NANMO. For NANMO 80 % capacity retention (counted from cycle 39, the beginning of the long term cycling) is reached in cycle 77, while for NANMFO it is reached in cycle 82. NAFMO shows overall less capacity and is less capable of high C-rates. The capacity degradation during the long term cycling with 1C appears to be similar to NANMO and NANMFO, where the slope of the data points for all three materials looks alike. NMFO delivers even less capacity and almost none during the higher C-rates of 5C and 10C. The capacity fading during the long term cycling takes place slower than for the other three materials. For an interpretation of this observation, the values of porosity Φ and specific surface area A_{BET} after sintering with 950 °C presented before in Chapter 5.1 are shown once more in Table 5.9.
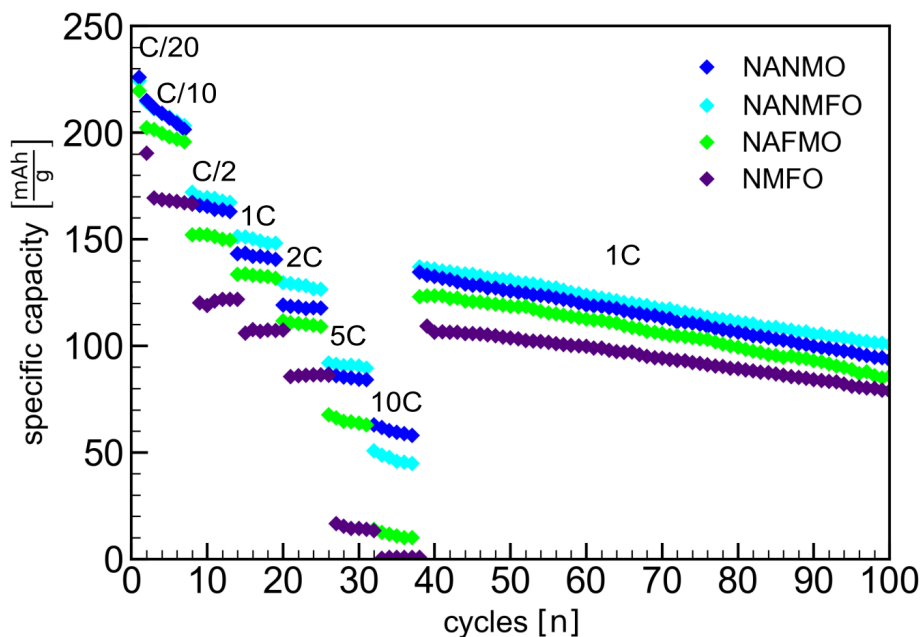
Figure 5.22: **Material comparison:** Half-cell cycling of the four layered sodium oxides sintered with 950 °C. The half-cells were cycled in the window 1.5 V to 4.6 V. The formation cycle with 1C at the beginning is not shown.

Table 5.9: **Morphology after** 950 °C **sintering:** Porosity Φ and specific surface area A_{BET} for the four layered oxides which were used as cathode material in Figure 5.22. The data was before shown in Table 5.3 in Chapter 5.1.

	NANMO	NANMFO	NAFMO	NMFO
Φ in %	45	43	32	18
A_{BET} in m²/g	3.9	3.1	2.0	1.0

The received capacity for NANMO is similar to the one achieved by Hasa et al. [36], who investigated the same chemical composition but with a different synthesis. Hasa et al. measured 240 mA h g^{-1} in the first cycle with C/10. The long term stability in the work from Hasa et al. was tested with 0.125C, where a capacity retention of 80 % was reached after 50 cycles [36]. In the presented work 80 % of capacity of the hierarchically structured material was maintained for 59 cycles while cycling with 1C, but with smaller capacity delivered due to the bigger current.

NANMO and NANMFO exhibit quite similar morphologies, especially the same porosity, which is known to have a great impact on capacity and rate-capability [5]. This explains why the obtained capacities are so similar. It also points out, that the iron content with the redox-pair of Fe^{4+}/Fe^{3+} was capable to replace half the nickel amount with the corresponding Ni^{4+}/Ni^{3+} pair. The Mößbauer spectroscopy measurements (see Chap. 5.1.6 *Mößbauer spectroscopy*) showed only 26.5 % of Fe^{4+} in a charged NANMFO

sample. Together with nickel this amount was sufficient for the same capacity, assuming that Ni^{4+} was formed as well.

A possible reason for the better rate-capability at 1-5C of NANMFO is the before mentioned vacancy-ordering. In the previous Chapter 5.3 *In situ X-ray diffraction* it was presented how replacing some nickel content with iron leads to the smoothing of the slopes of the charge-discharge-curves. The same was seen here in Figure 5.21. With the in situ XRD it was shown that the absence of distinct plateaus was caused by the absence or lack of sodium-vacancy-ordering: Both sodium sites Na_1 and Na_2 in the lattice of NANMFO were emptied and filled simultaneously, while for NANMO the preferred site was Na_1. This was supported by the lower activation energy for ionic hopping in the NANMFO lattice, measured with impedance spectroscopy (see Chap. 5.2). This lower activation energy can lead to a better rate-capability [31]. The collected in situ XRD data also showed that the phase transition for NANMFO started at higher voltage (more close to the cut off voltage 4.6 V) and therefore a smaller biphasic region was visible in the contour plot (Fig. 5.18). A less severe phase transition of NANMFO in the given ECW should also promise a more stable cycling behaviour. At 10C however, NANMO delivered more capacity than NANMFO. Perhaps with these high currents of 10C the difference form vacancy-ordering and phase transition is no longer significant but another property such as porosity is more relevant. As mentioned before, both CAMs exhibit similar porosity and specific surface area, while the values are slightly higher for NANMO.

One goal of the presented work is to create a cathode material with less nickel to reduce another critical and costly element besides lithium and cobalt (see Chap. 1). Even with half of nickel replaced with iron the comparison of $Na_{0.6}Al_{0.11}Ni_{0.22}Mn_{0.66}O_2$ (NANMO) and $Na_{0.6}Al_{0.11}Ni_{0.11}Fe_{0.11}Mn_{0.66}O_2$ (NANMFO) showed no reduced capacity or stability. Instead, for moderate C-rates even an improvement was visible, which makes the material NANMFO a potential candidate for SIB with low nickel.

So far only the specific capacity has been considered. However, the cell voltage has to be taken into account for the energy density of a cell. The average discharge voltage (AV) multiplied by the specific capacity results in the energy density W [1]. To put this into perspective: The average voltage for NANMO in the first cycle with C/20 of Figure 5.22 is 2.96 V and for NANMFO it is 2.88 V. This difference arises from the voltage plateaus of NANMO (see Fig. 5.21). The calculation for the energy density returns the values 657 W h kg^{-1} for NANMO and 637 W h kg^{-1} for NANMFO. After 100 cycles (Fig. 5.22), both capacity and average voltage have decayed: 2.75 V average voltage and W = 257 W h kg^{-1} was obtained for NANMO and 2.5 V and W = 246 W h kg^{-1} for NANMFO. This is a disadvantage that accompanies the substitution of nickel and can not be nullified by further improvements of a hierarchically structured electrode. The values for energy density (only mass of cathode active material considered) and average voltage are shown for some specific cycles in Table 5.10. Here are also the other two nickel free materials shown. The CAMs are listed from top to bottom from highest nickel to highest iron content. It can be seen that the average voltage and thus the energy density is decreasing from high Ni to high Fe content. It can also be seen that the retention of

Table 5.10: **Energy densities:** The energy density W (of the mass of the cathode active material) and the average voltage AV of the cells is listed here. At the first cycle a C-rate of C/20 was used. For the other listed cycles the rate was always 1C. In the end the retention (Ret.) of both parameters is shown comparing first with last cycle.

	Cycle (Rate)	**1** (C/20)	**15** (1C)	**38** (1C)	**100** (1C)	Ret. in % Cycl. 1 to 100
NANMO	W in Wh/kg$_c$	657	424	380	257	39
	AV in V	2.96	2.99	2.82	2.75	93
NANMFO	W in Wh/kg$_c$	637	423	360	246	39
	AV in V	2.88	2.81	2.65	2.5	87
NAFMO	W in Wh/kg$_c$	600	348	298	189	32
	AV in V	2.73	2.6	2.42	2.2	81
NMFO	W in Wh/kg$_c$	517	253	252	163	32
	AV in V	2.7	2.36	2.27	2.05	76

the AV is highest in case of NANMO.

Table 5.10 shows also that the decay of the average voltage from cycle 1 to 100 is not (only) due to the change from a low to a higher C-rate, but is a fatigue effect. Even with the same rate (three cycles with 1C) a decay of the AV is visible over the cycling life.

The theoretical capacity of NAFMO (green in Fig. 5.22) is equal to the one of NAN-MFO. The smaller experimental capacity of NAFMO can be explained by the values from table 5.9: Secondary particles of NAFMO exhibit 32 % in comparison with 43 % for NANMFO. The reduced porosity was also shown in the SEM pictures of electrode cross sections in Chapter 5.1.2: Inside a spherical NAFMO secondary particle there were thick primary particles visible forming the internal structure. The measurement of Mößbauer spectroscopy (Chap. 5.1.6) showed that only approx. 37 % of the iron content was oxidized into Fe^{4+}. Iron in the centre of thick primary particles can only be oxidized and reduced when sodium ions diffuse through the solid phase. Na^+ ion diffusion suffers from sluggish kinetics [80]. In case of the Mößbauer spectroscopy the half-cells were charged with C/20 and the potential was held at 4.6 V until the flowing current fell below C/50. Even with this small C-rate and dwell time at high potential it was not possible to oxidize all iron completely. The smaller porosity and bigger primary particles can also be interpreted as the reason why the capacity drops strongly at high C-rates of 5C and is nearly zero at 10C. The rate capability of NAFMO is still better than for NMFO. One reason for that is the low porosity and thick primary particles of NMFO (discussed later). Another reason might again be a lower E_{A_i} for NAFMO than

for NMFO (see Chap. 5.2) which became visible as less vacancy ordering (see Chap. 5.3).

The degradation which is similar to the two materials with higher porosity (NANMO and NANMFO) implies that the capacity fading is influenced by more than just porosity. One reason is the upper voltage limit of 4.6V where severe change in the lattice parameters and lattice volume causes stress for the materials (see Chap. 5.3 *In situ X-ray diffraction*). Porosity can help to buffer this expansion and compression. NAFMO exhibits significantly less porosity than NANMO and NANMFO. Apparently, this moderate porosity is enough to buffer the volume change, especially together with another material effect of NAFMO: With in situ XRD in Chapter 5.3 the development of the crystal structure was investigated. In case of NAFMO no phase transition into the Z-phase was observed, a process that can lead to capacity fading via irreversible transition [6].

A similarity between NANMO, NANMFO and NAFMO, which is also affecting degradation, is the aluminium content. The incorporation of electrochemical inactive Al into the host lattice is known to increase the lattice volume of layered oxides $Na(TM, Mn)O_2$ when replacing Mn [45, 48]. Al in the structure also helps to dampen the distortion caused by the Jahn-Teller-mechanism due to the Mn^{4+}/Mn^{3+} redox reaction at around 2.0V [48].

Mößbauer spectroscopy has shown that the amount of tetravalent iron in a charged NMFO cathode is even lower than in case of NAFMO. Here, only 32% were obtained. Being the least porous material of the compared four (Tab. 5.9) and having the thickest primary particles (see cross sections in Fig. 5.4 in Chap. 5.1), NMFO exhibits the smallest specific capacity. Besides this small porosity NMFO contains no aluminium. It is therefore not understandable why it is resistant against the two mentioned degradation mechanisms, best visible in the long-term cycling with 1C in Figure 5.22. This long term stability depends strongly on the sintering temperature T_S. Later in the comparison of different sintering temperatures in the range from 850 °C to 1000 °C the degradation for NMFO is quite strong for all other temperatures (see Chap. 5.4.4).

In this context it is also worth mentioning the conductivities, measured in Chapter 5.2 *Conductivity properties*. The measured conductivities at room temperature are summarized in Table 5.11. It was measured that the electronic conductivity σ_e at room temperature for NANMO and NAFMO was higher (almost one order of magnitude) than for NANMFO and NMFO. The similar cycling performance of NANMO and NANMFO indicates that the influence by σ_e is small in this case. However it needs to be noted that in the used slurries for the cathode sheets the ratio of active material to conductive carbon and binder was 80:10:10. This is commonly used for testing new materials, the high amount of conductive carbon ensures a good overall electronic conductivity in the electrode. For LIB the typical amount of active material are rather in the order of 90 % to 95 % [85, 86]. The different electronic conductivities might have a stronger influence on the performance if the amount of conductive carbon in the electrode preparation is reduced.

Table 5.11: **Conductivities summarized**: Here is the data from Chap. 5.2 *Conductivity properties* summarized. The electronic σ_e and ionic conductivity σ_i are shown the four CAMs, sintered at 950 °C and measured at room temperature (20 °C). The standard deviation was added for an error estimation.

	NANMO	**NANMFO**	**NAFMO**	**NMFO**
σ_e in S/cm	$(6.43 \pm 0.5) \cdot 10^{-7}$	$(5.24 \pm 0.8) \cdot 10^{-8}$	$(9.01 \pm 1.3) \cdot 10^{-8}$	$(2.88 \pm 0.4) \cdot 10^{-8}$
σ_i in S/cm	$(7.14 \pm 0.2) \cdot 10^{-7}$	$(6.83 \pm 1.7) \cdot 10^{-9}$	$(7.73 \pm 2.8) \cdot 10^{-9}$	$(1.84 \pm 0.6) \cdot 10^{-9}$

The differences in the ionic conductivities σ_i were however stronger. Over two orders of magnitude σ_i was higher for NANMO when compared to NANMFO, NAFMO and NMFO. The difference may arise from the size of the primary particles and whether they are connected via thin sinter necks or if the particles are merged together. Solid state kinetic of sodium ions is affected via these mechanisms. Zahnow et al. showed this dependence on Li NMC [16]. The conductivities of their samples were decreasing, showed a minimum and where then increasing again, when the porosity was increased. On the other hand the conductivity was reduced with a bigger „grain size " (here primary particle size) for most of the samples.

High ionic conductivity is helpful for active material with low porosity or big primary particles, where less electrolyte can reach the centre of a CAM particle [5]. This might be another reason for the reduced performance of NMFO where both low $\sigma_i = 1.8 \cdot 10^{-9}$ S/cm and disadvantageous morphology ($\Phi = 12\%$ and big primary particles) are combined as compared to NAFMO with high $\sigma_i = 7.73 \cdot 10^{-9}$ S/cm and higher porosity (22 %). However the performance of NANMO and NANMFO was rather similar for most C-rates, even though $\sigma_i = 7.14 \cdot 10^{-7}$ S/cm for NANMO is two orders of magnitude higher than for NANMFO with $\sigma_i = 6.83 \cdot 10^{-9}$ S/cm. The disadvantage of lower ionic conductivity of NANMFO appears to be not significant in this context. The particles of NANMO and NANMFO exhibit both a high porosity of 45 % and 43 % (see Tab. 5.9). With this high porosity a good penetration of electrolyte inside the active material appears to make the higher σ_i non-essential for NANMFO. The before mentioned effect reduced sodium vacancy-ordering in NANMFO might also compensating the reduced conductivity by lowering the activation energy barrier for the diffusion process.

In the next subsection the cycling behaviour with different upper voltage limits will be discussed. After that, another subsection focuses on the influence of the sintering temperature. This can be understood as an individual optimization of the materials.

5.4.3 Influence of the electrochemical window

From LIBs, a typical thumb rule is that cycling between 20% and 80% state of charge (SOC) increases the battery lifetime [11]. The same is true for the here presented SIBs.

(a)

(b)

(c)

(d)
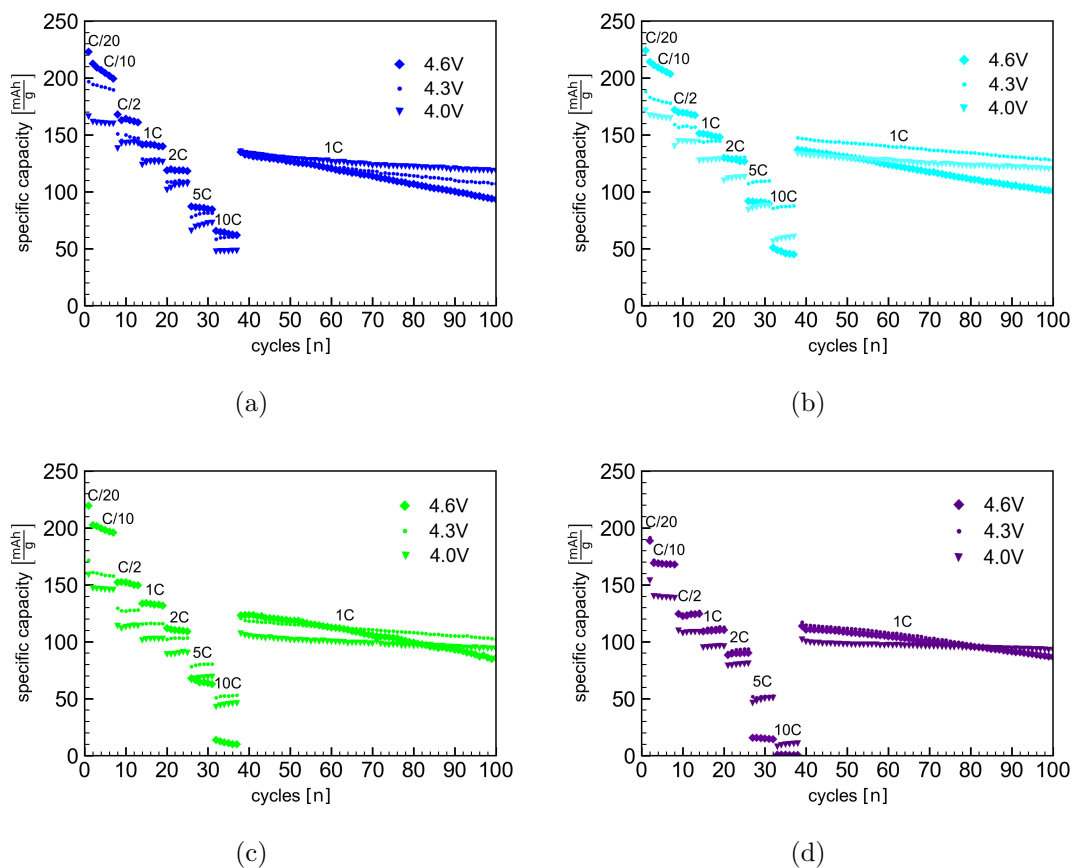
Figure 5.23: **Different upper voltage limits:** Half-cells cycled in the windows with 1.5 V lower limit and various upper limits: 4.0 V, 4.3 V and 4.6 V. The previously used colour code is used here as well: Blue for NANMO (a), cyan for NAN-MFO (b), green for NAFMO (c) and purple for NMFO (d).

So far, the cycling in the range 1.5 V to 4.6 V was considered as 100% SOC. Avoiding the upper limit means less change in lattice parameters and less or no phase transition. Also, the not yet optimized electrolyte for SIB has limits in the high voltage region [19]. Decomposition of electrolyte salts and solvents have an influence on capacity fading when cycled in the high voltage region [87].

In the following, the same materials (sintered at 950 °C) as before were tested with different voltage limits. While the lower limit was kept at 1.5 V, the upper was reduced to 4.3 V and 4.0 V. This reduces the obtained energy density and specific capacity, but also improves the cycling stability. Whether high capacity or longer lifetime is favoured depends on the application [11]. The cycling behaviour of the four layered oxides is shown in Figure 5.23: (a) NANMO, (b) NANMFO, (c) NAFMO and (d) NMFO. The different upper limits are indicated with a diamond symbol for 4.6 V, a point for 4.3 V and a triangle for 4.0 V. For all materials the obtained capacity gets reduced especially in the region of small rates of C/20 and C/10. With moderate rates, e.g. 1C, there is less

77

difference. It can be observed that a smaller electrochemical window (ECW) increases the cycling stability in the long-term cycling with 1C, visible with a less steep slope of the decay. The best stability or in other words the highest capacity retention after 100 cycles is always achieved with 4.0 V in this comparison. However it can be seen how the four cathode materials react in a different way on the changed cycling window.

The strong decay with 4.6 V as upper limit (UL) mostly related to the crystal structure. As seen in Chapter 5.18 *In situ X-ray diffraction* the P2-structure undergoes phase transition in the high voltage region. Beyond 4.1 V this phase transition can cause irreversible damage [88]. Even if the transformation from P2 to O2 is not completely performed (or does not take place, like for NAFMO), it has been shown in Chapter 5.18 that lattice parameters change strongly already before the transition. Avoiding this region therefore leads to a better cycling stability for all CAMs.

With 4.3 V as UL the cycling stability of NANMO was already improved while the cell still holds a high amount of capacity (Fig. 5.23 (a)). This can be compared to NANMFO (b), which has a quite similar particle morphology and therefore less risk of false interpretation. For a better comparison of the different materials in the same window another depiction of the same data from Figure 5.23 is presented in Figure 5.24. Here data is sorted by the upper voltage limit: 4.6 V (a), 4.3 V (b) and 4.0 V (c). The four materials are again distinguishable by the colour code. In case of NANMFO a similar improvement of cycling stability with still decent capacity was achieved, when switching to 4.3 V (Fig. 5.24 (b)). However it can be seen for moderate and high C-rates (1C to 10C) and during the long-term cycling more capacity was obtained as compared to NANMO. This difference may arise from two material properties that have been revealed by in situ XRD in Chapter 5.3. NANMFO (cyan) exhibits less sodium vacancy ordering than NANMO (blue) and therefore reduced diffusion barriers, which leads to an overall improvement of the ionic transport mechanism. This can be seen best as a delivering more capacity with moderate and high C-rates. The other effect visible in the XRD data was a late phase transition for NANMFO, which started at a higher cell voltage. A biphasic region is developed at 4.46 V for NANMFO and at 4.40 V for NANMO (thicker cathodes in case of in situ XRD). Also for NANMFO with absence of a voltage plateau in this high voltage area resulted in a shorter time period for the formation of a new phase. Therefore the biphasic region covered a smaller area in the contour plots as compared to NANMO (Fig. 5.18 2θ vs. time vs. intensity).

In case of NAFMO the reduction of the UL to 4.3 V had a similar effect like before for NANMFO: Reduced specific capacity was achieved, but the improvement of the cycling stability can be seen, here especially for the long-term cycling with 1C (Fig. 5.23 (c)). Since NAFMO did not show any phase transition in the in situ XRD analysis, it can be estimated that this improvement is mainly due to reduced stress on the lattice.

With the lowest porosity of 18 % and the biggest primary particle size (see SEM electrode cross section in Fig. 5.4) the cathode material NMFO (Fig. 5.23 (d)) shows less specific capacity than the others with UL 4.6 V. There is almost no difference visible

(a)

(b)

(c)
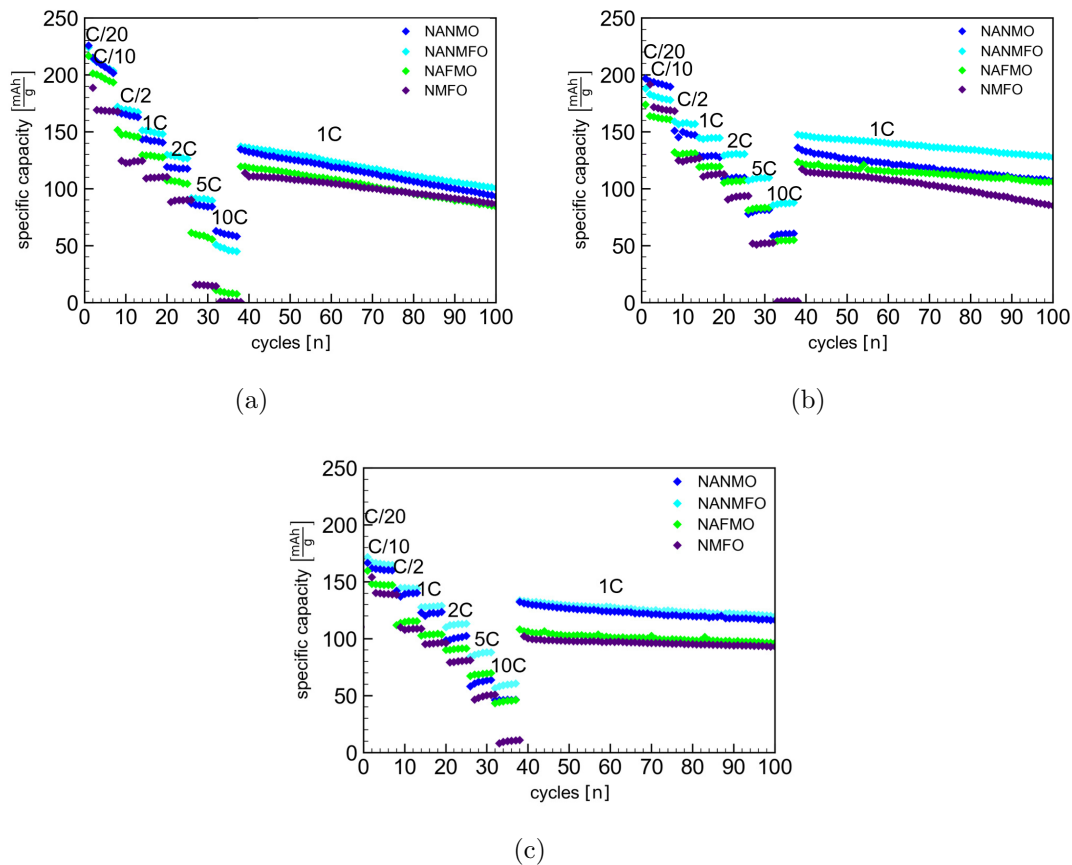
Figure 5.24: **Material comparison:** Half-cells data analogue to Fig. 5.23 with 1.5 V as lower limit and various upper limits: 4.6 V (a), 4.3 V (b) and 4.0 V (c).

when changing the UL from 4.6 V to 4.3 V. Demonstrating that not just the high voltage region is problematic but that the particle morphology of NMFO is not yet optimized. Avoiding the high voltage region with severe lattice change and phase transition completely by changing the UL to 4.0 V results in the most stable cycling behaviour for all materials (Fig. 5.24 (c)).

These different behaviours when choosing one of the three upper limits demonstrate, that the four CAMs need to be optimized individually. This will be addressed in the following chapter where different sintering temperatures will be tested. The three upper limits will as well be part of this optimization.

5.4.4 Optimizing

For an individual optimization it is not only necessary to choose an electrochemical window (ECW) for cycling, but also the sintering temperature T_s. In Chapter 5.1, the influence of sintering temperature on material properties was already discussed. Here,

(a) 1.5 - 4.6 V

(b) 1.5 - 4.3 V

(c) 1.5 - 4.0 V

NANMO				
T_s in °C	**850°C**	**900°C**	**950°C**	**1000°C**
Φ in %	51-53	51	45	42
A_{BET} in m²/g	5.9	4.7	3.9	2.8

(d)

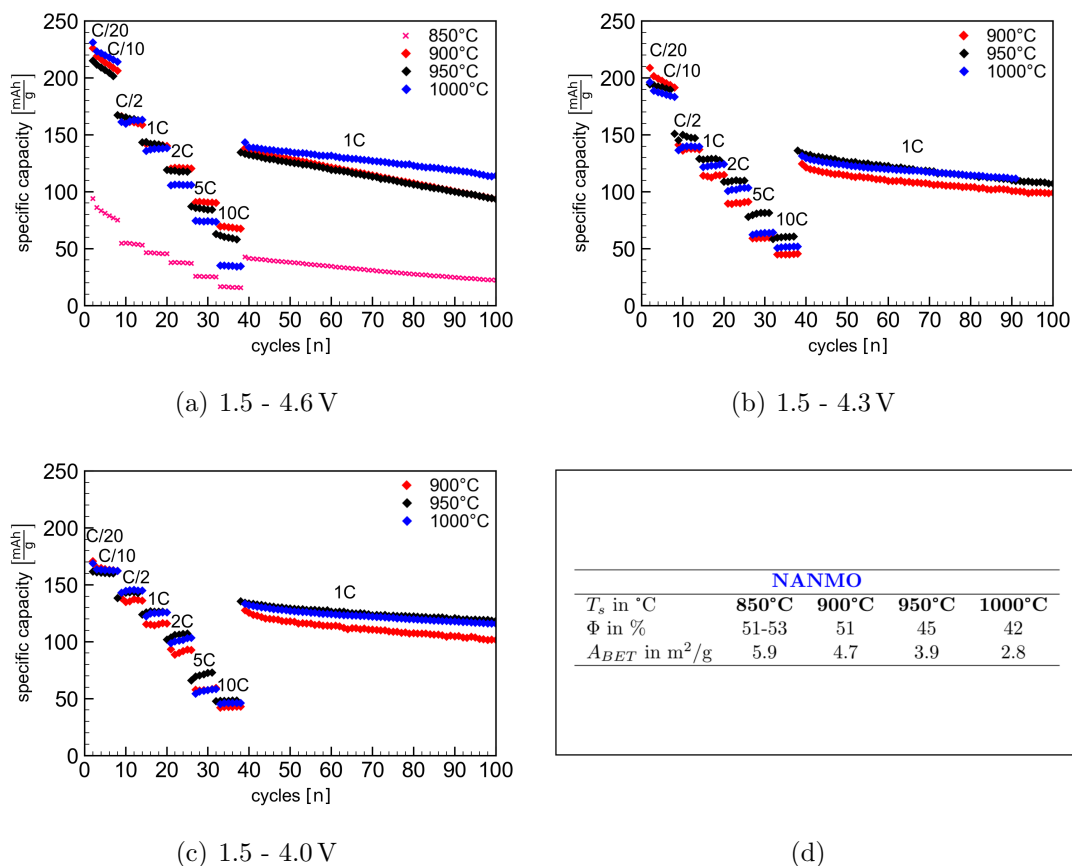Figure 5.25: **Optimization of NANMO:** Half-cells cycled with various upper voltage limits: (a) 4.6V, (b) 4.3V and (c) 4.0V. The active material was sintered at different temperatures which leads to different morphologies described with the porosity Φ [03] and specific surface area A_{BET} (d).

it will be shown how these properties influence the electrochemical behaviour. In literature with lithium based layered oxides which have been prepared with spray drying it is known that there is an optimum for the sintering temperature [5]. Each coin cell test was repeated to ensure reproducibility. At the end of the chapter, the material parameters and performances will be summarized in the Tables 5.12 and 5.13.

Figure 5.25 shows the specific capacity during cycling of NANMO in three different voltage windows. The lower voltage limit was always kept at 1.5V. The different upper limits (UL) were 4.6 V (a), 4.3 V (b) and 4.0 V (c) again. As a reminder from section

---

[03] As mentioned in Chap. 5.1.1 *Morpholoy*, the porosimetry device failed several times during the measurement of NANMO sintered at 850 °C. The value could be narrowed down to a small range, since spray dried particles showed 53 % porosity and sintering at 900 °C exhibited 51 %. On top of that, only poor electrochemical performance was obtained with 850 °C sintering. Therefore an other repetition of porositmetry measurement was not of interest.

5.1.3 of Chapter *Material properties* the values of porosity Φ and specific surface area A_{BET} after a certain sintering temperatures T_s are shown in (d). In addition to that, CAMs sintered at different temperatures from 850 °C to 1000 °C are displayed with different colours. In case of NANMO, the previously declared colour code was changed to different colours for better distinction. With a temperature of 850 °C only a poor electrochemical performance was achieved. Since this behaviour was reproduce-able and far from the theoretical capacity, the corresponding cathode material was not tested in the other two voltage windows. With the other three T_s, similar performances were obtained. CAM with $T_s = 900$ °C showed lower capacities in (b) and (c), while $T_s = 950$ °C and 1000 °C resulted in almost the same performance. An exception to that can be seen in (a), were more stability is achieved with $T_s = 1000$ °C.

This can be interpreted as follows: Even at the lowest sintering temperature 850 °C, the P2-type crystal structure was observed (see Fig. 5.7 in Chap. 5.1.4 *Crystal structure* of the section *Material properties*). Increasing the sintering temperature led to some changes, such as reflection positions (lattice-parameters), reflection sharpness and intensity ratio (crystallite sizes) and reduction of impurities. Since these changes were small, it was concluded that the P2-phase is already well developed at 850 °C. This cannot explain the poor cycling performance. The characteristic plateaus of redox reactions described before in Chapter 5.4.1 could also be observed for $T_s = 850$ °C (not shown), so an electrochemical activity was present.

An explanation of the poor cycling performance might be the sinter activity. In Chapter 5.1 *Material properties*, it was shown how the sinter activity of the active material particles depended on the nickel and iron content. After the second spray drying (step V in Chap. 4 *Experimental*) a spherical secondary particle (SP) is formed from loose connection of primary particles (PP). Increasing the sintering temperature leads to a reduction of porosity Φ and specific surface area A_{BET} of the SP. This was understood as merging of neighbouring PP. The internal connection of an SP is thereby increased. This has an influence on both electronic and ionic conductivity of an SP [16]. A low T_s and low sinter activity of the material itself would lead to a poor connection and therefore low conductivities. Low sintering activity was observed for high nickel content (NANMO), which increased with the iron content. Here it can be assumed that $T_s = 850$ °C is too low for good internal connection of a spray dried SP. In literature the same was observed for lithium based layered oxide: Wagner et al. [5] investigated different sintering temperatures for spray dried hierarchically structured NMC111. They also found that with too low temperatures too little sinter necks are formed and therefore poor electrochemical performance was obtained. The reduced internal contact in a secondary particle would also have an impact on the conductivity of the active material. In further work, this effect could be supported using impedance spectroscopy on pellets sintered at different temperatures, as it was presented for only one temperature in Chapter 5.2 *Conductivity properties*.

The other three sintering temperatures resulted in good cycling behaviour with similar performance. The highest Φ and A_{BET} at 900 °C did, however, not generally lead to an improved rate-capability. This was only observed for the window with 4.6 V upper volt-

age (a). Another property for the UL 4.6 V is also the superior stability of the CAM with $T_s = 1000\,°C$, even though its porosity and surface area is the lowest. Additional space inside the SP can generally buffer the lattice change [5], but this does not appear to make the observed difference. Lattice-parameter change and the chance of phase transition increase in magnitude with higher voltage (see Chap. 5.18 *In situ X-ray diffraction*). The higher sintering temperature of $T_s = 1000\,°C$ shifts reflection positions, increases intensities and reduces impurities as compared to lower temperatures (see Fig. 5.7 in Chap. 5.1.4 *Crystal structure*). This seems to improve the cycling stability in this high voltage region, where change in the crystal structure is most critical and irreversible damage is done to the P2-type structure [88]. This assumption could be investigated in further work with in situ XRD (as presented in Chap. 5.3), performed on NANMO with different sintering temperatures.

In case of 4.3 V (b) and 4.0 V (c) as UL, a sintering temperature of 950 °C is sufficient to reach the same capacity and stability. For an upscaling of the synthesis process (as mentioned in Chap. 4.2 *Synthesis*), reduced energy consumption would be beneficial.

For NANMFO, the electrochemical performance observed was similar to the performance of NANMO when comparing different sintering temperatures in different voltage windows. In Figure 5.26, the results of half-cell tests with NANMFO cathodes sintered at different temperatures are shown. 4.6V (a), 4.3V (b) and 4.0V (c) were used as upper limit of the ECW. The colour code was kept consistent (different shades of blue highlight that here only NANMFO is compared). With $T_s = 1000\,°C$ the cathode material showed an improved long-time stability compared to the others in the window 1.5 - 4.6V, while with $T_s = 850\,°C$ only poor performance was obtained. For this reason, the CAM with $T_s = 850\,°C$ was not tested in the smaller ECWs. With 4.0 V and 4.3 V as upper limit $T_s = 950\,°C$ showed the highest capacity at all C-rates.

The poor cycling performance for $T_s = 850\,°C$ can be explained in the same way as before for NANMO: With a low iron content, the sinter activity of 850 °C is not enough to create a good internal connection inside an SP.

With 4.6 V (a) as UL, the crystal structure undergoes severe stress. With $T_s = 1000\,°C$ the crystal structure is further developed (Fig. 5.7 in Chap. 5.1.4) and can better endure this stress. In case of 4.0V (c) and 4.3V (b) as upper voltage limit, $T_s = 950°C$ appears to be optimal as a compromise of higher porosity, specific surface area and developed crystal structure. Again, this is interesting in terms of energy consumption during synthesis procedure when thinking about scaling-up.

The data of the next CAM, NAFMO, one of the nickel-free materials, is presented in Figure 5.27. Different shades of green were used for the sintering temperatures and the upper voltage limit of the cell tests was 4.6 V (a), 4.3 V (b) and 4.0 V (c). The obtained morphology data is again shown in (d). In this case, all sintering temperatures from 850 °C to 1000 °C resulted in good cycling performance. Over all temperatures and ECWs, similar results were obtained. With 4.6 V (a) for the upper limit, the CAM with $T_s = 900\,°C$ delivers the highest capacity. However, the degradation in this window is

(a) 1.5 - 4.6 V

(b) 1.5 - 4.3 V

(c) 1.5 - 4.0 V

	NANMFO			
T_s in °C	**850°C**	**900°C**	**950°C**	**1000°C**
Φ in %	52	47	43	42
A_{BET} in m^2/g	4.4	3.5	3.1	2.2

(d)

Figure 5.26: **Optimization of NANMFO:** Active material sintered at different temperatures and cycled as half-cells with various upper voltage limits: (a) 4.6V, (b) 4.3V and (c) 4.0V. The porosities and specific surface areas obtained are shown in (d).

once more lowest for $T_s = 1000\,°C$. With $4.3\,V$ as UL, there is almost no difference in the performance and degradation. Only at high C-rates the CAM with $T_S = 1000\,°C$ delivers less capacity. In the window $1.5\,V$ to $4.0\,V$, the sintering temperature $850\,°C$ resulted in higher capacity for all C-rates.

The reason for the best stability of $T_s = 1000\,°C$ in (a) ($4.6\,V$) might be the same as before: A further developed crystallite can take the lattice stress best, but since the porosity is considerably lower as compared to NAFMO with $T_s = 850\,°C$ to $950\,°C$, there is less specific capacity gained for currents $> C/10$.

Since less lattice strain is created in the smaller windows, there is no significant difference shown in (b) with $4.3\,V$. In (c) with $4.0\,V$ as upper limit $T_s = 850\,°C$ seems to be an optimum of particle morphology and developed crystal structure. Here, it can be seen that increasing temperate from $850\,°C$ to $900\,°C$ reduces the specific capacity for most C-rates. Increasing T_s further rises the obtained capacities again, suggesting a contrastive influence. Since the optimum in (c) seems to be $T_s = 850\,°C$, an upscaling

(a) 1.5 - 4.6 V

(b) 1.5 - 4.3 V

(c) 1.5 - 4.0 V

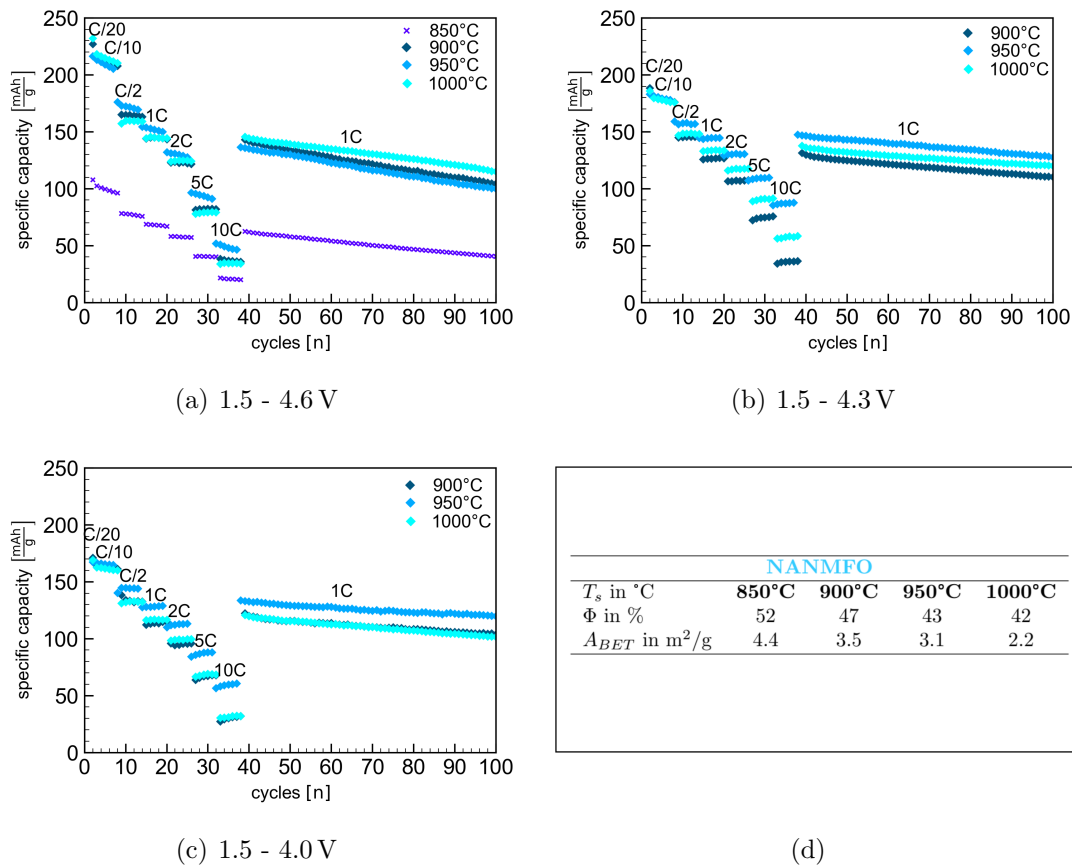| NAFMO				
T_s in °C	**850°C**	**900°C**	**950°C**	**1000°C**
Φ in %	48	43	32	22
A_{BET} in m²/g	4.3	4.0	2.0	1.5

(d)

Figure 5.27: **Optimization of NAFMO:** Active material sintered at different temperatures and cycled as half-cells with various upper voltage limits: 4.6 V (a), 4.3 V (b) and 4.0 V (c). Morphology data is shown in (d).

of the synthesis process would benefit a lot from the low sintering temperature in terms of energy consumption.

For the last of the four layered oxides, NMFO without any electrochemical inactive aluminium is presented. Figure 5.28 shows the cycling performance in the same windows as before: 4.6 V (a), 4.3 V in (b) and 4.0 V (c) as UL of the ECW. Morphology data of the different sintering temperatures is shown in (d). In (a), with 4.6 V as upper limit, higher capacities can be obtained with $T_s = 850\,°C$ to $900\,°C$. For all sintering temperatures, the degradation during long-time cycling is strong, only for $T_s = 950\,°C$ more stability can be observed. In (b) (UL = 4.3 V) the CAM with $T_s = 850\,°C$ shows higher capacity than the others again, and the same stability as for $T_s = 950\,°C$. In the smallest ECW (c) with UL = 4.0 V, the cathode material with $T_s = 850\,°C$ shows the highest capacity during the C-rate-test and a good cycling stability during the long-time-cycling. The stability for all other materials is improved as well.
In case of NMFO, the influence of T_s is the strongest. This is supported by the strong

(a) 1.5 - 4.6 V

(b) 1.5 - 4.3 V

(c) 1.5 - 4.0 V

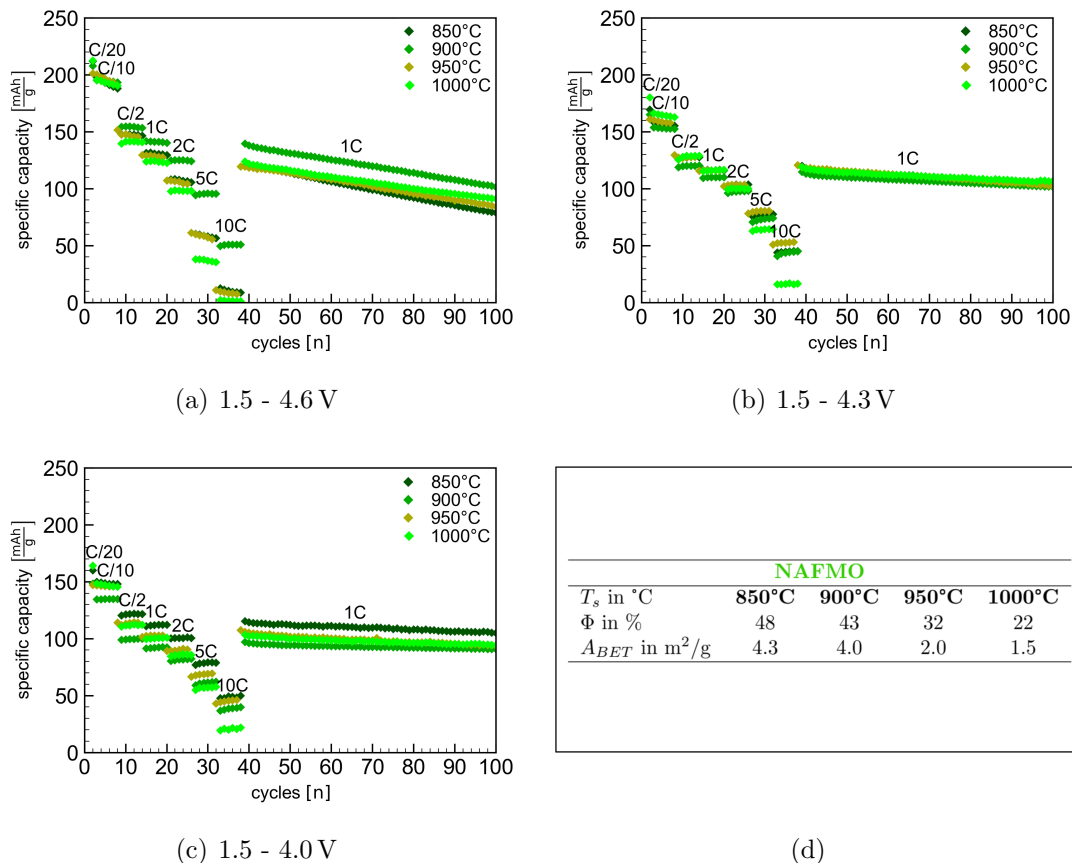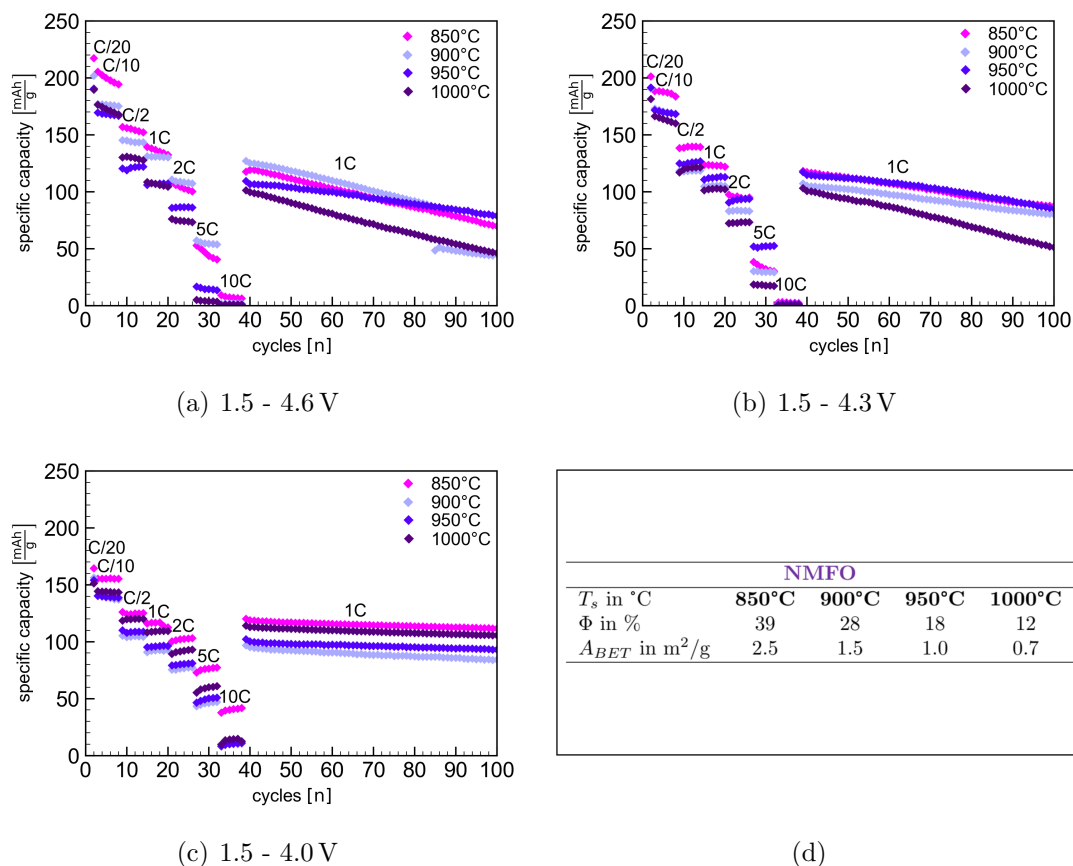|	NMFO			
T_s in °C	**850°C**	**900°C**	**950°C**	**1000°C**
Φ in %	39	28	18	12
A_{BET} in m^2/g	2.5	1.5	1.0	0.7

(d)

Figure 5.28: **Optimization of NMFO:** Active material sintered at different temperatures and cycled as half-cells with various upper voltage limits: (a) 4.6 V, (b) 4.3 V and (c) 4.0 V. Morphology data is shown in (d).

change of SP porosity (compare to (d)). The strong degradation for UL = 4.6 V and UL = 4.3 V can be attributed to the absence of Al, as it was discussed in Chapter 5.4.3 before. An optimum in terms of capacity retention was found for UL = 4.6 V with T_s = 950 °C, while for the smaller ECWs T_s = 850 °C is favourable. This can also be considered as an advantage for less energy consumption during production.

For a better overview, a summary of capacity and capacity retention of all presented data is displayed in the Tables 5.12 and 5.13. Some specific data points from the Figures in this section (Fig. 5.25, 5.26, 5.27, 5.28) were taken into account: The specific capacities from the first cycle with a current of C/20, from cycle no. 39 (first cycle of long time cycling with 1C) and the last cycle (no. 100) of the long time cycling. The retention is calculated under consideration of cycle 39 and 100 (61 in total) and refers therefore to a current of 1C. The retention and still remaining Q_{spec} in the last cycle can be compared for the four different CAMs, the four sintering temperatures T_s and the upper voltage limit.

Here it can easily be seen that the highest retentions between $80\,\%$ to $90\,\%$ for the individual materials can be found with the upper voltage limit (UL) of $4.0\,\text{V}$, which matches the before described change in lattice parameters and phase transitions. It can also be seen, that for the aluminium containing materials the obtained retention with UL = $4.3\,\text{V}$ also shows retention in the same range.

A suitable material to replace $Na_{0.6}Al_{0.11}Ni_{0.22}Mn_{0.66}O_2$ (NANMO) with high nickel content can be found with $Na_{0.6}Al_{0.11}Ni_{0.11}Fe_{0.11}Mn_{0.66}O_2$ (NANMFO), with only half of nickel necessary, yet still a high capacity. E.g. with $T_s = 950\,°\text{C}$ and UL = $4.3\,\text{V}$ a specific capacity of $Q_{spec} = 128\,\text{mA}\,\text{h}\,\text{g}^{-1}$ remains in the last cycle with a retention of about $86\,\%$. The highest retention of approx. $90\,\%$ for this material was achieved for UL = $4.0\,\text{V}$ and $T_s = 950\,°\text{C}$ and $Q_{spec} = 120\,\text{mA}\,\text{h}\,\text{g}^{-1}$.

$Na_{0.6}Al_{0.11}Fe_{0.22}Mn_{0.66}O_2$ (NAFMO) without any Ni delivers its highest remaining capacity of $Q_{spec} = 108\,\text{mA}\,\text{h}\,\text{g}^{-1}$ in cycle no. 100 with UL = $4.3\,\text{V}$, $T_s = 1000\,°\text{C}$ and a retention of $91\,\%$. Also lower sintering temperatures deliver quite similar results in this window. The highest retention $93\,\%$ was obtained for UL = $4.0\,\text{V}$ and $T_s = 900\,°\text{C}$.

If $Na_{0.6}Fe_{1/3}Mn_{2/3}O_2$ (NMFO) is to be considered as a replacement for NANMO it seems to operate decently only in the window of $1.5\,\text{V}$ to $4.0\,\text{V}$. This can be understood as a disadvantage due to the lower average potential. In this case however the lowest energy consumption during synthesis with sintering temperature $T_s = 850\,°\text{C}$ results in the highest remaining capacity $Q_{spec} = 112\,\text{mA}\,\text{h}\,\text{g}^{-1}$ and best retention of $93\,\%$.

Table 5.12: **Summarized capacities of Ni containing CAMs:** Data taken from Fig. 5.25 and 5.26. Specific capacities Q_{spec} from cylce 1, 39 and 100. The capacity retention obtained with different upper voltage limits (UL) and sintering temperatures T_s can be compared in the last column.

<div align="center">

NANMO

</div>

UL	T_s in °C	Cycle 1 (C/20)	Cycle 39 (1C) Q_{spec} in mAh/g	Cycle 100 (1C)	Retention in %
	850	95	43	23	53
4.6V	900	226	139	94	68
	950	225	135	93	69
	1000	232	144	116	81
	850	-	-	-	-
4.3V	900	209	125	100	80
	950	196	138	108	78
	1000	196	132	112[04]	85[04]
	850	-	-	-	-
4.0V	900	172	128	102	80
	950	166	135	119	88
	1000	170	133	116	87

<div align="center">

NANMFO

</div>

UL	T_s in °C	Cycle 1 (C/20)	Cycle 39 (1C) Q_{spec} in mAh/g	Cycle 100 (1C)	Retention in %
	850	109	62	41	66
4.6V	900	228	143	104	73
	950	226	137	101	74
	1000	232	146	115	79
	850	-	-	-	-
4.3V	900	189	132	111	84
	950	189	148	128	86
	1000	186	138	121	88
	850	-	-	-	-
4.0V	900	172	124	105	85
	950	172	134	120	90
	1000	170	121	102	84

---

[04] Only until cycle 91

Table 5.13: **Summarized capacities of Fi containing CAMs:** Data taken from Fig. 5.27 and 5.28. Specific capacities Q_{spec} from cylce 1, 39 and 100. The capacity retention obtained with different upper voltage limits (UL) and sintering temperatures T_s can be compared in the last column.

| | | **NAFMO** | | | |
| | | Cycle 1 (C/20) | Cycle 39 (1C) | Cycle 100 (1C) | |
UL	T_s in °C		Q_{spec} in mAh/g		Retention in %
4.6V	850	212	121	80	66
	900	208	141	103	73
	950	217	120	85	71
	1000	212	124	92	74
4.3V	850	170	120	102	85
	900	165	115	102	89
	950	171	121	102	84
	1000	180	119	108	91
4.0V	850	160	116	105	91
	900	148	98	91	93
	950	160	108	94	87
	1000	164	103	95	92

| | | **NMFO** | | | |
| | | Cycle 1 (C/20) | Cycle 39 (1C) | Cycle 100 (1C) | |
UL	T_s in °C		Q_{spec} in mAh/g		Retention in %
4.6V	850	217	118	69	58
	900	202	127	88 [05]	69 [05]
	950	190	110	79	72
	1000	190	101	46	46
4.3V	850	202	119	87	73
	900	191	107	80	75
	950	191	117	84	72
	1000	181	103	52	50
4.0V	850	164	120	112	93
	900	156	97	85	88
	950	154	102	93	91
	1000	151	114	106	93

[05] Only until cycle 84

5.4.5 Long term stability

To demonstrate the long term stability a comparison of the materials can be seen in Figure 5.29. There is a test with a lower C-rate of C/2 for the long-time cycling after two cycles with C/20. In this case only one sintering temperature was tested ($T_s = 1000\,°C$). (a) shows the ECW $1.5\,V$ to $4.3\,V$ as a compromise of high voltage and better stability. With the C-rate cut in half, the stability has already been improved in this window.

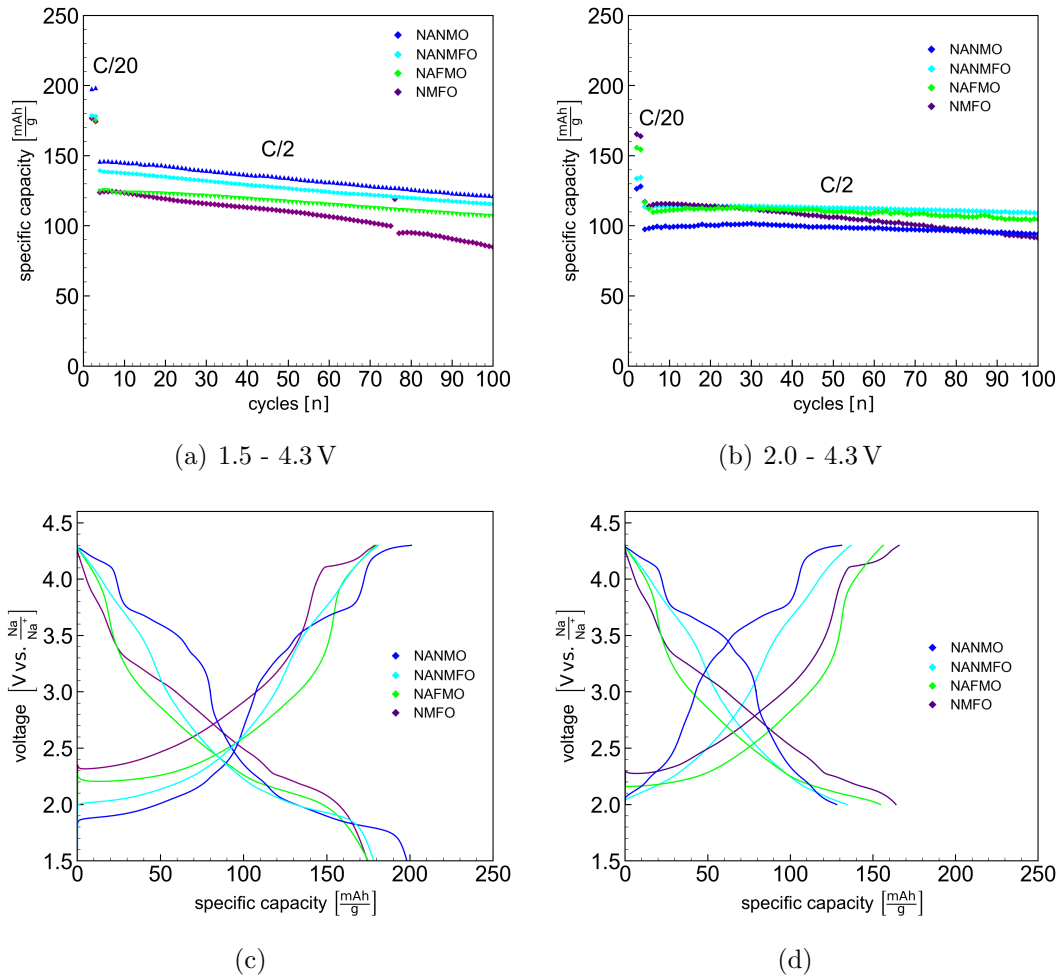(a) 1.5 - 4.3 V   (b) 2.0 - 4.3 V

(c)   (d)

Figure 5.29: **Long-time stability:** The four layered oxides can be compared directly in terms of their cycling stability in two different voltage windows. In (a), the electrochemical window was $1.5\,V$ to $4.3\,V$. The corresponding voltage profiles of the 3rd cycle (C/2) are shown in (c). In (b), the same long-time test in the smaller window $2.0\,V$ to $4.3\,V$ is shown, with the corresponding voltage profiles in (d).

In the region from 3 to 100 cycles (C/2) the four CAMs still retain the following capacities:

- NANMO: $Q_{spec} = 121\,\mathrm{mA\,h\,g^{-1}} \to 83\,\%$

- NANMFO: $Q_{spec} = 115\,\mathrm{mA\,h\,g^{-1}} \to 83\,\%$

- NAFMO: $Q_{spec} = 107\,\mathrm{mA\,h\,g^{-1}} \to 86\,\%$

- NMFO: $Q_{spec} = 85\,\mathrm{mA\,h\,g^{-1}} \to 68\,\%$

A similar degradation of NANMO and NANMFO can be seen. NAFMO appears to be slightly more stable. In Chapter 5.3 *In situ X-ray diffraction* it was shown that for NAFMO no phase transition at high voltage (beyond 4.3 V) was observed in the conducted experiment, while the other three CAMs displayed a phase transition of the P2 phase into OP4. It can be assumed that this is reason for the improved stability when cycling in the window 1.5 V to 4.6 V with small currents (Fig. 5.29 (a)). However with bigger currents (e.g. long term cycling with 1C in Fig. 5.22) this assumed advantage appears not to be significant anymore. Shorter charge-time in general results in a not complete phase transition, due to slow kinetics and porosity plays an important role. Since NANMO and NANMFO display higher porosities than NAFMO the absence of a phase transition brings NAFMO to the same level of stability when cycling with 1C.

Due to the low porosity and absence of Al, the degradation is still visibly stronger for NMFO than for the other CAMs. The misplaced data point in cycle 76 of NMFO arose during a malfunction of the potentiostat. This created a small rift in the continuity, but the degradation still continues with a similar slope.
To avoid the Jahn-Teller-distortion around 2.0 V to some exten, the lower limit was set to 2.0 V. 4.3 V was kept as upper limit. The data for that is shown in Figure 5.29 (b) and (d). In the voltage profiles (c) and (d) it can be seen why a cut off at 2.0 V benefits higher capacity for NMFO and is a disadvantage for NANMO. The overall stability was improved for all materials. As before, the strongest degradation can still be seen for NMFO. The following capacities could be retained after 98 cycles with C/2:

- NANMO: $Q_{spec} = 94\,\mathrm{mA\,h\,g^{-1}} \to 97\,\%$

- NANMFO: $Q_{spec} = 109\,\mathrm{mA\,h\,g^{-1}} \to 96\,\%$

- NAFMO: $Q_{spec} = 104\,\mathrm{mA\,h\,g^{-1}} \to 88\,\%$

- NMFO: $Q_{spec} = 91\,\mathrm{mA\,h\,g^{-1}} \to 78\,\%$

Again, an optimized (nano-)structuring with high porosity and small primary particles seems to improve stability. Also the absence of inactive Al in case of NMFO appears to be a disadvantage for the stability. The highest average potential can be found in both windows for NANMO, followed by NANMFO, NMFO and NAFMO (voltage profiles in Fig. 5.29).

For even more stable long-term cycling, the ECW could be narrowed down even further to $2.0 - 4.0\,\text{V}$, which is considered to be a region in which the P2-type structure of sodium layered oxides is completely stable [88]. This however would reduce the specific capacity even further. A lower level of $2.0\,\text{V}$ is closer to the open circuit voltage of the layered oxides, which can be found around $2.7\,\text{V}$. Cycling below the OCV results in intercalation of additional sodium from the metal anode into the layered structure. This was discussed in Chapter 5.4.1. One possible step for further investigations of the presented materials would be full-cells. Without e.g. pre-sodiation of the anode, additional sodium cannot add up to higher capacity [27]. A lower voltage limit closer to OCV is therefore a step into the direction of full-cells. A comparison of NANMFO long-term tests with various voltage windows is presented in the appendix in chapter 7.4.3.

6 Conclusion and outlook

In conclusion it can be summarized, that different P2-type layered oxides were synthesized and investigated and proofed to be suitable as sodium-ion cathode active materials (CAM).

With the spray drying method hierarchically structured, porous particles can be synthesized. 600 g of precursor powder and 110 g of cathode active material were synthesized in one batch, demonstrating the potential of upscaling the process. Typical particle sizes were ranging from 2 µm to 32 µm with an average size of approx. 10 µm. Depending on the sintering temperature $T_s = 850 - 1000\,°C$ different particle porosities in the range of 12- 52 % were obtained.

To reduce the amount of the last critical element in this chemical composition, Ni was subsequently replaced with Fe. With the control over every aspect from synthesis to battery tests it was investigated how the material properties were influenced by this:
Changing the chemical composition influences several material properties: Particle porosity Φ, particles specific surface area A_{BET} (particle morphology), the conductivity (both electronic and ionic), lattice parameters and their change, phase-transformation and sodium vacancy ordering during cycling, average cell potential, specific capacity and capacity retention.

A brief comparison of material properties of the four P2-type layered oxides is summarized in the following:
The cathode material $Na_{0.6}Al_{0.11}Ni_{0.22}Mn_{0.66}O_2$ (NANMO) exhibits a high particle porosity, high ionic and electronic conductivity. Problematic for this material is the distinctive sodium vacancy ordering, a Z-phase developement which leads to the biggest loss of P2-structure (as compared to the other CAMs) and its high nickel content. All in all, these properties result in high capacity and good stability.
$Na_{0.6}Al_{0.11}Ni_{0.11}Fe_{0.11}Mn_{0.66}O_2$ (NANMFO) shows the same particle porosity like NANMO but less ionic and electronic conductivity. However, this disadvantage seems to be balanced with less sodium vacancy ordering and less Z-phase development (more of P2 remains) in the high voltage region. These properties lead to high capacity and good stability as well. The performance of NANMFO is equivalent to NANMO, even with half of nickel replaced with iron.
The nickel-free synthesis of $Na_{0.6}Al_{0.11}Fe_{0.22}Mn_{0.66}O_2$ (NAFMO) results in lower particle porosity but again high ionic and electronic conductivity. No Z-phase development and less sodium vacancy ordering can be observed. This leads to a reduced, but still high capacity and good cycling stability. In the smallest cycling window the lowest sintering temperature leads to the best performance.
The CAM $Na_{0.6}Fe_{1/3}Mn_{2/3}O_2$ (NMFO) exhibits the lowest particle porosity and lowest conductivity. No electrochemical inactive aluminium is present in its structure. Z-phase development is visible, but the lowest for the compared materials. Vacancy ordering is present, but less than for NANMO. All these properties result in a rather low perfor-

mance. Especially with 4.3 V and 4.6 V as upper cycling limit, NMFO shows an inferior performance and quick capacity fading. However, a decent capacity and very good cycling stability can still be achieved with 4.0 V as upper limit. Noteworthy in context with the lower cut off voltage is, that in this window the lowest sintering temperature leads to the best results and a capacity retention higher than for the other CAM.

A recommendation for further investigation can be made for the cathode materials were Ni was reduced or replaced with Fe, like NANMFO and NAFMO. They showed initial capacities of $232 \, \text{mA} \, \text{h} \, \text{g}^{-1}$ and $208 \, \text{mA} \, \text{h} \, \text{g}^{-1}$ in the broadest voltage window of 1.5 V to 4.6 V. Rate-capability and cycling stability can be individually optimized by sintering temperature T_s and the upper voltage limit. NMFO can be taken into account due to the remarkable high capacity retention in the window 1.5 V to 4.0 V.

Further optimization of the synthesis process can be potentially found in synthesis steps I to IV (see Chap. 4). For the synthesis different educts could be used in step I. The use of acetates and nitrates proved to be successful but approximately half of the precursors mass decompose and evaporate during the first heat treatment (step III). TG measurements showed that this process takes place in a window of 230 °C to 257 °C. This was a constant challenge during the synthesis. Different edcuts might help to reduce this abrupt reaction to a less severe decomposition. Spray drying as step II is not necessarily needed for the preparation of the precursor powders (only for step V). Also a lower temperature for the first heat treatment (step III) could be sufficient for the calcination process, while higher temperatures are only needed for step VI (sintering). The milling (step IV) was performed in a planetary ball mill. First attempts to synthesize NANMO with an agitated media mill were successfully performed but not completely analysed. This has lead to smaller primary particles and more dense secondary particles. While high porosity usually leads to a good cycling performance, as it was demonstrated in the presented work, for an industrial application high porosity is counterproductive for a high volumetric capacity. For further steps to the application a compromise for decent porosity and high volumetric capacity needs to be evaluated. The sodium deficiency could be overcome with pre-sodiation methods to facilitate high capacities for SIB full cells [27]. With the objective of full cells it would be of interest to repeat the measurements of Chapter 5.4.4 *Optimization* (summarized in Tab. 5.12 & 5.13) with 2.0 V or the open circuit voltage as lower limit for the cycling window.

References

[1] Manuel Baumann, Marcel Häringer, Marius Schmidt, Luca Schneider, Jens F. Peters, Werner Bauer, Joachim R. Binder, and Marcel Weil. Prospective Sustainability Screening of Sodium-Ion Battery Cathode Materials. *Advanced Energy Materials*, page 2202636, October 2022.

[2] Robert C Massé, Evan Uchaker, and Guozhong Cao. Beyond Li-ion: electrode materials for sodium-and magnesium-ion batteries. *Science China Materials*, 58(9):715–766, 2015.

[3] Christoph Vaalma, Daniel Buchholz, Marcel Weil, and Stefano Passerini. A cost and resource analysis of sodium-ion batteries. *Nature reviews materials*, 3(4):1–11, 2018.

[4] Wei Zheng, Xiaobing Huang, Yurong Ren, Haiyan Wang, Shibiao Zhou, Yuandao Chen, Xiang Ding, and Tao Zhou. Porous spherical $Na_3V_2(PO_4)_3$/C composites synthesized via a spray drying-assisted process with high-rate performance as cathode materials for sodium-ion batteries. *Solid State Ionics*, 308:161–166, 2017.

[5] Amalia Christina Wagner, Nicole Bohn, Holger Geßwein, Matthias Neumann, Markus Osenberg, André Hilger, Ingo Manke, Volker Schmidt, and Joachim R Binder. Hierarchical Structuring of NMC111-Cathode Materials in Lithium-Ion Batteries: An In-Depth Study on the Influence of Primary and Secondary Particle Sizes on Electrochemical Performance. *ACS Applied Energy Materials*, 3(12):12565–12574, 2020.

[6] James W Somerville, Adam Sobkowiak, Nuria Tapia-Ruiz, Juliette Billaud, Juan G Lozano, Robert A House, Leighanne C Gallington, Tore Ericsson, Lennart Häggström, Matthew R Roberts, et al. Nature of the "Z"-phase in layered Na-ion battery cathodes. *Energy & Environmental Science*, 12(7):2223–2232, 2019.

[7] R Cecchini and G Pelosi. Alessandro Volta and his battery. *IEEE Antennas and Propagation Magazine*, 34(2):30–37, 1992.

[8] K. J. P. C. Mizushima, P. C. Jones, P. J. Wiseman, and John B. Goodenough. Li_xCoO_2 $(0 < x \leq 1)$: A new cathode material for batteries of high energy density. *Materials Research Bulletin*, 15(6):783–789, 1980.

[9] M Stanley Whittingham. Electrical energy storage and intercalation chemistry. *Science*, 192(4244):1126–1127, 1976.

[10] Akira Yoshino. The birth of the lithium-ion battery. *Angewandte Chemie International Edition*, 51(24):5798–5800, 2012.

[11] Fran Hoffart. Proper care extends Li-ion battery life. *Power Electron*, 34:24–28, 2008.

[12] Safat Bin Wali, MA Hannan, MS Reza, Pin Jern Ker, RA Begum, MS Abd Rahman, and M Mansor. Battery storage systems integrated renewable energy sources: A biblio metric analysis towards future directions. *Journal of Energy Storage*, 35:102296, 2021.

[13] Gordon Haxel. *Rare earth elements: critical resources for high technology*, volume 87. US Department of the Interior, US Geological Survey, 2002.

[14] Toshinari Koketsu, Jiwei Ma, Benjamin J Morgan, Monique Body, Christophe Legein, Walid Dachraoui, Mattia Giannini, Arnaud Demortiere, Mathieu Salanne, François Dardoize, et al. Reversible magnesium and aluminium ions insertion in cation-deficient anatase TiO_2. *Nature materials*, 16(11):1142–1148, 2017.

[15] Christian Julien, Alain Mauger, Ashok Vijh, and Karim Zaghib. Lithium batteries. In *Lithium batteries*, pages 29–68. Springer, 2016.

[16] Julian Zahnow, Tim Bernges, Amalia Wagner, Nicole Bohn, Joachim R. Binder, Wolfgang G. Zeier, Matthias T. Elm, and Jürgen Janek. Impedance Analysis of NCM Cathode Materials: Electronic and Ionic Partial Conductivities and the Influence of Microstructure. *ACS Applied Energy Materials*, 4(2):1335–1345, January 2021.

[17] Giuseppe Antonio Elia, Krystan Marquardt, Katrin Hoeppner, Sebastien Fantini, Rongying Lin, Etienne Knipping, Willi Peters, Jean-Francois Drillet, Stefano Passerini, and Robert Hahn. An overview and future perspectives of aluminum batteries. *Advanced Materials*, 28(35):7564–7579, 2016.

[18] Ashish Rudola, Anthony JR Rennie, Richard Heap, Seyyed Shayan Meysami, Alex Lowbridge, Francesco Mazzali, Ruth Sayers, Christopher J Wright, and Jerry Barker. Commercialisation of high energy density sodium-ion batteries: Faradion's journey and outlook. *Journal of Materials Chemistry A*, 9(13):8279–8302, 2021.

[19] Amrtha Bhide, Jonas Hofmann, Anna Katharina Dürr, Jürgen Janek, and Philipp Adelhelm. Electrochemical stability of non-aqueous electrolytes for sodium-ion batteries and their compatibility with $Na_{0.7}CoO_2$. *Physical Chemistry Chemical Physics*, 16(5):1987–1998, 2014.

[20] Kei Kubota, Mouad Dahbi, Tomooki Hosaka, Shinichi Kumakura, and Shinichi Komaba. Towards K-ion and Na-ion batteries as "beyond Li-ion". *The chemical record*, 18(4):459–479, 2018.

[21] Yu Xia, Jianming Zheng, Chongmin Wang, and Meng Gu. Designing principle for Ni-rich cathode materials with high energy density for practical applications. *Nano Energy*, 49:434–452, 2018.

[22] Harsha Walvekar, Hector Beltran, Shashank Sripad, and Michael Pecht. Implications of the Electric Vehicle Manufacturers' Decision to Mass Adopt Lithium-Iron Phosphate Batteries. *IEEE Access*, 10:63834–63843, 2022.

[23] Ana-Irina Stan, Maciej Świerczyński, Daniel-Ioan Stroe, Remus Teodorescu, and Søren Juhl Andreasen. Lithium ion battery chemistries from renewable energy storage to automotive and back-up power applications—An overview. In *2014 International Conference on Optimization of Electrical and Electronic Equipment (OPTIM)*, pages 713–720. IEEE, 2014.

[24] Jens F Peters, Alexandra Peña Cruz, and Marcel Weil. Exploring the economic potential of sodium-ion batteries. *Batteries*, 5(1):10, 2019.

[25] Rui-Min Gao, Zi-Jian Zheng, Peng-Fei Wang, Cao-Yu Wang, Huan Ye, and Fei-Fei Cao. Recent advances and prospects of layered transition metal oxide cathodes for sodium-ion batteries. *Energy Storage Materials*, 30:9–26, September 2020.

[26] Mingzhe Chen, Qiannan Liu, Shi-Wen Wang, Enhui Wang, Xiaodong Guo, and Shu-Lei Chou. High-Abundance and Low-Cost Metal-Based Cathode Materials for Sodium-Ion Batteries: Problems, Progress, and Key Technologies. *Advanced Energy Materials*, 9(14):1803609, February 2019.

[27] Daniel Dewar and Alexey M Glushenkov. Optimisation of sodium-based energy storage cells using pre-sodiation: a perspective on the emerging field. *Energy & Environmental Science*, 14(3):1380–1401, 2021.

[28] Yalan Liu, Dong Wang, Haoyu Li, Ping Li, Yan Sun, Yang Liu, Yuxia Liu, Benhe Zhong, Zhenguo Wu, and Xiaodong Guo. Research progress in O3-type phase Fe/Mn/Cu-based layered cathode materials for sodium ion batteries. *Journal of Materials Chemistry A*, 10(8):3869–3888, 2022.

[29] Peng-Fei Wang, Ya You, Ya-Xia Yin, and Yu-Guo Guo. Layered oxide cathodes for sodium-ion batteries: phase transition, air stability, and performance. *Advanced Energy Materials*, 8(8):1701912, 2018.

[30] Yuechuan Lei, Xin Li, Lei Liu, and Gerbrand Ceder. Synthesis and stoichiometry of different layered sodium cobalt oxides. *Chemistry of Materials*, 26(18):5288–5296, 2014.

[31] Na Wang, Hu-Rong Yao, Xin-Yu Liu, Ya-Xia Yin, Jie-Nan Zhang, Yuren Wen, Xiqian Yu, Lin Gu, and Yu-Guo Guo. Vacancy disordering promises high-rate Na-ion batteries. *Sci. Adv*, (4), 2018.

[32] Xuehang Wu, Jianghuai Guo, Dawei Wang, Guiming Zhong, Matthew J McDonald, and Yong Yang. P2-type $Na_{0.66}Ni_{0.\,33-x}Zn_xMn_{0.67}O_2$ as new high-voltage cathode materials for sodium-ion batteries. *Journal of Power Sources*, 281:18–26, 2015.

[33] Peng-Fei Wang, Ya You, Ya-Xia Yin, Yue-Sheng Wang, Li-Jun Wan, Lin Gu, and Yu-Guo Guo. Suppressing the P2-O2 phase transition of $Na_{0.67}Mn_{0.67}Ni_{0.33}O_2$ by magnesium substitution for improved sodium-ion batteries. *Angewandte Chemie*, 128(26):7571–7575, 2016.

[34] Dingding Yuan, Xiaohong Hu, Jiangfeng Qian, Feng Pei, Fayuan Wu, Rongjun Mao, Xinping Ai, Hanxi Yang, and Yuliang Cao. P2-type $Na_{0.67}Mn_{0.65}Fe_{0.2}Ni_{0.15}O_2$ cathode material with high-capacity for sodium-ion battery. *Electrochimica Acta*, 116:300–305, 2014.

[35] Ivana Hasa, Daniel Buchholz, Stefano Passerini, Bruno Scrosati, and Jusef Hassoun. High Performance $Na_{0.5}[Ni_{0.23}Fe_{0.13}Mn_{0.63}]O_2$ Cathode for Sodium-Ion Batteries. *Advanced Energy Materials*, 4(15):1400083, 2014.

[36] Ivana Hasa, Stefano Passerini, and Jusef Hassoun. Toward high energy density cathode materials for sodium-ion batteries: investigating the beneficial effect of aluminum doping on the P2-type structure. *Journal of Materials Chemistry A*, 5(9):4467–4477, 2017.

[37] Naoki Nitta, Feixiang Wu, Jung Tae Lee, and Gleb Yushin. Li-ion battery materials: present and future. *Materials today*, 18(5):252–264, 2015.

[38] Hermann Arthur Jahn and Edward Teller. Stability of polyatomic molecules in degenerate electronic states-I—Orbital degeneracy. *Proceedings of the Royal Society of London. Series A-Mathematical and Physical Sciences*, 161(905):220–235, 1937.

[39] Lin Zhang, Chenchen Wang, Yanchen Liu, Meng Ren, Juan Du, Aibing Chen, and Fujun Li. Suppressing interlayer-gliding and Jahn-Teller effect in P2-type layered manganese oxide cathode via Mo doping for sodium-ion batteries. *Chemical Engineering Journal*, 426:130813, 2021.

[40] Shinichi Kumakura, Yoshiyuki Tahara, Kei Kubota, Kuniko Chihara, and Shinichi Komaba. Sodium and manganese stoichiometry of P2-type $Na_{2/3}MnO_2$. *Angewandte Chemie*, 128(41):12952–12955, 2016.

[41] Pengfei Yan, Jianming Zheng, Meng Gu, Jie Xiao, Ji-Guang Zhang, and Chong-Min Wang. Intragranular cracking as a critical barrier for high-voltage usage of layer-structured cathode for lithium-ion batteries. *Nature communications*, 8(1):1–9, 2017.

[42] Xinyin Cai, Yanan Xu, Lei Meng, Xiujuan Wei, Fangyu Xiong, Tengfei Xiong, and Qinyou An. Insight into the capacity decay of layered sodium nickel manganese oxide cathodes in sodium ion batteries. *Journal of Alloys and Compounds*, 820:153093, April 2020.

[43] Mengya Li, Charl J Jafta, Linxiao Geng, Jue Liu, Yaocai Bai, Jianlin Li, Rachid Essehli, and Ilias Belharouak. Correlation of Oxygen Anion Redox Activity to In-Plane Honeycomb Cation Ordering in $Na_xNi_yMn_{1-y}O_2$ Cathodes. *Advanced Energy and Sustainability Research*, page 2200027, 2022.

[44] Sunwook Kim, Kyoungmin Min, and Kwangjin Park. Y-doped P2-type $Na_{0.67}Ni_{0.33}Mn_{0.67}O_2$: A sodium-ion battery cathode with fast charging and enhanced cyclic performance. *Journal of Alloys and Compounds*, 874:160027, 2021.

97

[45] Xiaoli Chen, Zebi Zhao, Kai Huang, and Haolin Tang. Al-substituted stable-layered P2-$Na_{0.6}Li_{0.15}Al_{0.15}Mn_{0.7}O_2$ cathode for sodium ion batteries. *International Journal of Energy Research*, 45(7):11338–11345, 2021.

[46] Hari Vignesh Ramasamy, Karthikeyan Kaliyappan, Ranjith Thangavel, Won Mo Seong, Kisuk Kang, Zhongwei Chen, and Yun-Sung Lee. Efficient method of designing stable layered cathode material for sodium ion batteries using aluminum doping. *The journal of physical chemistry letters*, 8(20):5021–5030, 2017.

[47] Raphaële J. Clément, Juliette Billaud, A. Robert Armstrong, Gurpreet Singh, Teófilo Rojo, Peter G. Bruce, and Clare P. Grey. Structurally stable Mg-doped P2-$Na_{2/3}Mn_{1-y}Mg_yO_2$ sodium-ion battery cathodes with high rate performance: insights from electrochemical, NMR and diffraction studies. *Energy & Environmental Science*, 9(10):3240–3251, 2016.

[48] Debasis Nayak, Pawan Kumar Jha, Sudipto Ghosh, and Venimadhav Adyam. Aluminium substituted β-type $NaMn_{1-x}Al_xO_2$: A stable and enhanced electrochemical kinetic sodium-ion battery cathode. *Journal of Power Sources*, 438:227025, 2019.

[49] Tim Risthaus, Dong Zhou, Xia Cao, Xin He, Bao Qiu, Jun Wang, Li Zhang, Zhaoping Liu, Elie Paillard, Gerhard Schumacher, et al. A high-capacity P2-$Na_{2/3}Ni_{1/3}Mn_{2/3}O_2$ cathode material for sodium ion batteries with oxygen activity. *Journal of power sources*, 395:16–24, 2018.

[50] Irwin C. Jacobs. Atomization and Spray-Drying Processes. In *Microencapsulation in the Food Industry*, pages 47–56. Elsevier, 2014.

[51] Benedicte Vertruyen, Nicolas Eshraghi, Caroline Piffet, Jerome Bodart, Abdelfattah Mahmoud, and Frederic Boschini. Spray-Drying of Electrode Materials for Lithium- and Sodium-Ion Batteries. *Materials*, 11(7):1076, June 2018.

[52] Marcus Müller, Luca Schneider, Nicole Bohn, Joachim R. Binder, and Werner Bauer. Effect of Nanostructured and Open-Porous Particle Morphology on Electrode Processing and Electrochemical Performance of Li-Ion Batteries. *ACS Applied Energy Materials*, 4(2):1993–2003, February 2021.

[53] Kusal K. Das, R. Chandramouli Reddy, Ishwar B. Bagoji, Swastika Das, Shrilaxmi Bagali, Lata Mullur, Jyoti P. Khodnapur, and M.S. Biradar. Primary concept of nickel toxicity – an overview. *Journal of Basic and Clinical Physiology and Pharmacology*, 30(2):141–152, September 2018.

[54] Zhonghua Lu and JR Dahn. The Effect of Co Substitution for Ni on the Structure and Electrochemical Behavior of T2 and O2 Structure $Li_{2/3}[Co_x Ni_{1/3-x} Mn_{2/3}]O_2$. *Journal of the Electrochemical Society*, 148(3):A237, 2001.

[55] BU Köhler and M Jansen. Darstellung und Strukturdaten von "Delafossiten" $CuMO_2$ (M= Al, Ga, Sc, Y). *Zeitschrift für anorganische und allgemeine Chemie*, 543(12):73–80, 1986.

[56] Jinsen Jiang, Hung-Chieh He, Chen Cheng, Tianran Yan, Xiao Xia, Manling Ding, Le He, Ting-Shan Chan, and Liang Zhang. Improving structural and moisture stability of P2-layered cathode materials for sodium-ion batteries. *ACS Applied Energy Materials*, 5(1):1252–1261, 2022.

[57] Yongxin Huang, Luzi Zhao, Li Li, Man Xie, Feng Wu, and Renjie Chen. Electrolytes and Electrolyte/Electrode Interfaces in Sodium-Ion Batteries: From Scientific Research to Practical Application. *Advanced Materials*, 31(21):1808393, March 2019.

[58] K Saitou. Microwave sintering of iron, cobalt, nickel, copper and stainless steel powders. *Scripta Materialia*, 54(5):875–879, 2006.

[59] Silje Nornes Bryntesen, Anders Hammer Strømman, Ignat Tolstorebrov, Paul R Shearing, Jacob J Lamb, and Odne Stokke Burheim. Opportunities for the state-of-the-art production of LiB electrodes—a review. *Energies*, 14(5):1406, 2021.

[60] Honghe Zheng, Li Tan, Gao Liu, Xiangyun Song, and Vincent S Battaglia. Calendering effects on the physical and electrochemical properties of $\mathrm{Li}\left[\mathrm{Ni}_{1/3}\mathrm{Mn}_{1/3}\mathrm{Co}_{1/3}\right]\mathrm{O}_2$ cathode. *Journal of Power Sources*, 208:52–57, 2012.

[61] Luca Schneider, Julian Klemens, Eike Christian Herbst, Marcus Muller, Philip Scharfer, Wilhelm Schabel, Werner Bauer, and Helmut Ehrenberg. Transport Properties in Electrodes for Lithium-Ion Batteries: Comparison of Compact versus Porous NCM Particles. *Journal of The Electrochemical Society*, 2022.

[62] Melissa A Denecke, W Gunsser, G Buxbaum, and P Kuske. Manganese valence in precipitated manganese ferrite. *Materials research bulletin*, 27(4):507–514, 1992.

[63] Benoit Mortemard de Boisse, Dany Carlier, Marie Guignard, Elodie Guerin, Mathieu Duttine, Alain Wattiaux, and Claude Delmas. Influence of Mn/Fe Ratio on Electrochemical and Structural Properties of P2-$\mathrm{Na}_x\mathrm{Mn}_{1-y}\mathrm{Fe}_y\mathrm{O}_2$ Phases as Positive Electrode Material for Na-Ion Batteries. *Chemistry of Materials*, 30(21):7672–7681, 2018.

[64] Jie Zhao, Jing Xu, Dae Hoe Lee, Nikolay Dimov, Ying Shirley Meng, and Shigeto Okada. Electrochemical and thermal properties of P2-type $\mathrm{Na}_{2/3}\mathrm{Fe}_{1/3}\mathrm{Mn}_{2/3}\mathrm{O}_2$ for Na-ion batteries. *Journal of Power Sources*, 264:235–239, 2014.

[65] Yusuke Nanba, Tatsumi Iwao, Benoit Mortemard de Boisse, Wenwen Zhao, Eiji Hosono, Daisuke Asakura, Hideharu Niwa, Hisao Kiuchi, Jun Miyawaki, Yoshihisa Harada, et al. Redox Potential Paradox in $\mathrm{Na}_x\mathrm{MO}_2$ for Sodium-Ion Battery Cathodes. *Chemistry of Materials*, 28(4):1058–1065, 2016.

[66] Yao Xiao, Yan-Fang Zhu, Hu-Rong Yao, Peng-Fei Wang, Xu-Dong Zhang, Hongliang Li, Xinan Yang, Lin Gu, Yong-Chun Li, Tao Wang, et al. A stable layered oxide cathode material for high-performance sodium-ion battery. *Advanced Energy Materials*, 9(19):1803978, 2019.

[67] Nam Pham Phuong Le, Nguyen Le Thanh Huynh, An Le Bao Phan, Dieu Thi Ngoc Nguyen, Trang Thi Thu Nguyen, Hoang Van Nguyen, Xujian Cui, Akhil Garg, Phung My Loan Le, and Man Van Tran. Effect of 3D Metal on Electrochemical Properties of Sodium Intercalation Cathode P2-$Na_xMe_{1/3}Mn_{2/3}O_2$ (M= Co, Ni, or Fe). *Journal of Chemistry*, 2021, 2021.

[68] Lei Wang, Yong-Gang Sun, Lin-Lin Hu, Jun-Yu Piao, Jing Guo, Arumugam Manthiram, Jianmin Ma, and An-Min Cao. Copper-substituted $Na_{0.67}Ni_{0.3-x}Cu_xMn_{0.7}O_2$ cathode materials for sodium-ion batteries with suppressed P2–O2 phase transition. *Journal of Materials Chemistry A*, 5(18):8752–8761, 2017.

[69] Christoph Dräger, Florian Sigel, Ralf Witte, Robert Kruk, Lukas Pfaffmann, Stefan Mangold, Valeriu Mereacre, Michael Knapp, Helmut Ehrenberg, and Sylvio Indris. Observation of electrochemically active Fe^{3+}/Fe^{4+} in $LiCo_{0.8}Fe_{0.2}MnO_4$ by in situ Mössbauer spectroscopy and X-ray absorption spectroscopy. *Physical Chemistry Chemical Physics*, 21(1):89–95, 2019.

[70] Murat Yavuz, Nilüfer Kiziltas-Yavuz, Aiswarya Bhaskar, Marco Scheuermann, Sylvio Indris, Francois Fauth, Michael Knapp, and Helmut Ehrenberg. Influence of iron on the structural evolution of $LiNi_{0.4}Fe_{0.2}Mn_{1.4}O_4$ during electrochemical cycling investigated by in situ powder diffraction and spectroscopic methods. *Zeitschrift für anorganische und allgemeine Chemie*, 640(15):3118–3126, 2014.

[71] Nilüfer Kiziltas-Yavuz, Murat Yavuz, Sylvio Indris, Natalia N Bramnik, Michael Knapp, Oleksandr Dolotko, Bijoy Das, Helmut Ehrenberg, and Aiswarya Bhaskar. Enhancement of electrochemical performance by simultaneous substitution of Ni and Mn with Fe in Ni-Mn spinel cathodes for Li-ion batteries. *Journal of power sources*, 327:507–518, 2016.

[72] Oleg Birkholz and Marc Kamlah. Electrochemical Modeling of Hierarchically Structured Lithium-Ion Battery Electrodes. *Energy Technology*, 9(6):2000910, 2021.

[73] Katarzyna Walczak, Katarzyna Redel, Rafal Idczak, Robert Konieczny, Karolina Idczak, Vinh Hung Tran, Anna Plewa, Magdalena Zikabka, Michal Rybski, Janusz Tobola, et al. Transport and Electrochemical Properties of $Na_xFe_{1-y}Mn_yO_2$-Cathode Materials for Na-Ion batteries. Experimental and Theoretical Studies. *Energy Technology*, 10(4):2101105, 2022.

[74] Miran Gaberscek, Joze Moskon, Bostjan Erjavec, Robert Dominko, and Janez Jamnik. The importance of interphase contacts in Li ion electrodes: the meaning of the high-frequency impedance arc. *Electrochemical and Solid-State Letters*, 11(10):A170, 2008.

[75] J Ross Macdonald and Evgenij Barsoukov. *Impedance spectroscopy: theory, experiment, and applications.* John Wiley & Sons, 2018.

[76] Zhenya Wang, Wenyun Yang, Jinbo Yang, Lirong Zheng, Kai Sun, Dongfeng Chen, Limei Sun, and Xiangfeng Liu. Tuning the crystal and electronic structure of $Li_4Ti_5O_{12}$ via Mg/La Co-doping for fast and stable lithium storage. *Ceramics International*, 46(9):12965–12974, June 2020.

[77] Katarzyna Walczak, Bartlomiej Geedziorowski, Andrzej Kulka, Wojciech Zajac, Magdalena Ziabka, Rafal Idczak, Vinh Hung Tran, and Janina Molenda. Exploring the Role of Manganese on Structural, Transport, and Electrochemical Properties of NASICON-$Na_3Fe_{2-y}Mn_y(PO_4)_3$-Cathode Materials for Na-Ion Batteries. *ACS Applied Materials & Interfaces*, 11(46):43046–43055, 2019.

[78] Qiu He, Bin Yu, Zhaohuai Li, and Yan Zhao. Density functional theory for battery materials. *Energy & Environmental Materials*, 2(4):264–279, 2019.

[79] Xuehang Wu, Gui-Liang Xu, Guiming Zhong, Zhengliang Gong, Matthew J. McDonald, Shiyao Zheng, Riqiang Fu, Zonghai Chen, Khalil Amine, and Yong Yang. Insights into the Effects of Zinc Doping on Structural Phase Transition of P2-Type Sodium Nickel Manganese Oxide Cathodes for High-Energy Sodium Ion Batteries. *ACS Applied Materials, Interfaces*, 8(34):22227–22237, August 2016.

[80] Yao Xiao, Nasir Mahmood Abbasi, Yan-Fang Zhu, Shi Li, Shuang-Jie Tan, Wei Ling, Ling Peng, Tingqiang Yang, Lude Wang, Xiao-Dong Guo, et al. Layered oxide cathodes promoted by structure modulation technology for sodium-ion batteries. *Advanced Functional Materials*, 30(30):2001334, 2020.

[81] Debasish Mohanty, Sergiy Kalnaus, Roberta A Meisner, Kevin J Rhodes, Jianlin Li, E Andrew Payzant, David L Wood III, and Claus Daniel. Structural transformation of a lithium-rich $Li_{1.2}Co_{0.1}Mn_{0.55}Ni_{0.15}O_2$ cathode during high voltage cycling resolved by in situ X-ray diffraction. *Journal of Power Sources*, 229:239–248, 2013.

[82] Aleksandr O Kondrakov, Holger Geßwein, Kristina Galdina, Lea De Biasi, Velimir Meded, Elena O Filatova, Gerhard Schumacher, Wolfgang Wenzel, Pascal Hartmann, Torsten Brezesinski, et al. Charge-transfer-induced lattice collapse in Ni-rich NCM cathode materials during delithiation. *The journal of physical chemistry C*, 121(44):24381–24388, 2017.

[83] Clement Bommier and Xiulei Ji. Electrolytes, SEI Formation, and Binders: A Review of Nonelectrode Factors for Sodium-Ion Battery Anodes. *Small*, 14(16):1703576, January 2018.

[84] Yanchen Liu, Chenchen Wang, Shuo Zhao, Lin Zhang, Kai Zhang, Fujun Li, and Jun Chen. Mitigation of Jahn–Teller distortion and Na^+/vacancy ordering in a distorted manganese oxide cathode material by Li substitution. *Chemical science*, 12(3):1062–1067, 2021.

[85] Daniel Miranda, A Gören, CM Costa, Maria Manuela Silva, AM Almeida, and S Lanceros-Méndez. Theoretical simulation of the optimal relation between active

material, binder and conductive additive for lithium-ion battery cathodes. *Energy*, 172:68–78, 2019.

[86] Matthias Haarmann, Desiree Grießl, and Arno Kwade. Continuous processing of cathode slurry by extrusion for lithium-ion batteries. *Energy Technology*, 9(10):2100250, 2021.

[87] Yan Jin, Phung ML Le, Peiyuan Gao, Yaobin Xu, Biwei Xiao, Mark H Engelhard, Xia Cao, Thanh D Vo, Jiangtao Hu, Lirong Zhong, et al. Low-solvation electrolytes for high-voltage sodium-ion batteries. *Nature Energy*, 7(8):718–725, 2022.

[88] Xiao-Zhen Liao Jing Xu Dezhi Yang Yu-Shi He Zi-Feng Ma Hong Wang, Bingjian Yang. Electrochemical properties of P2-Na$_{2/3}$[Ni$_{1/3}$Mn$_{2/3}$]O$_2$ cathodematerial for sodium ion batteries when cycled in differentvoltage ranges, 2013.

7 Appendix

7.1 Particle size distribution

7.1.1 Primary particle size

(a)

(b)

(c)

(d)

(e)
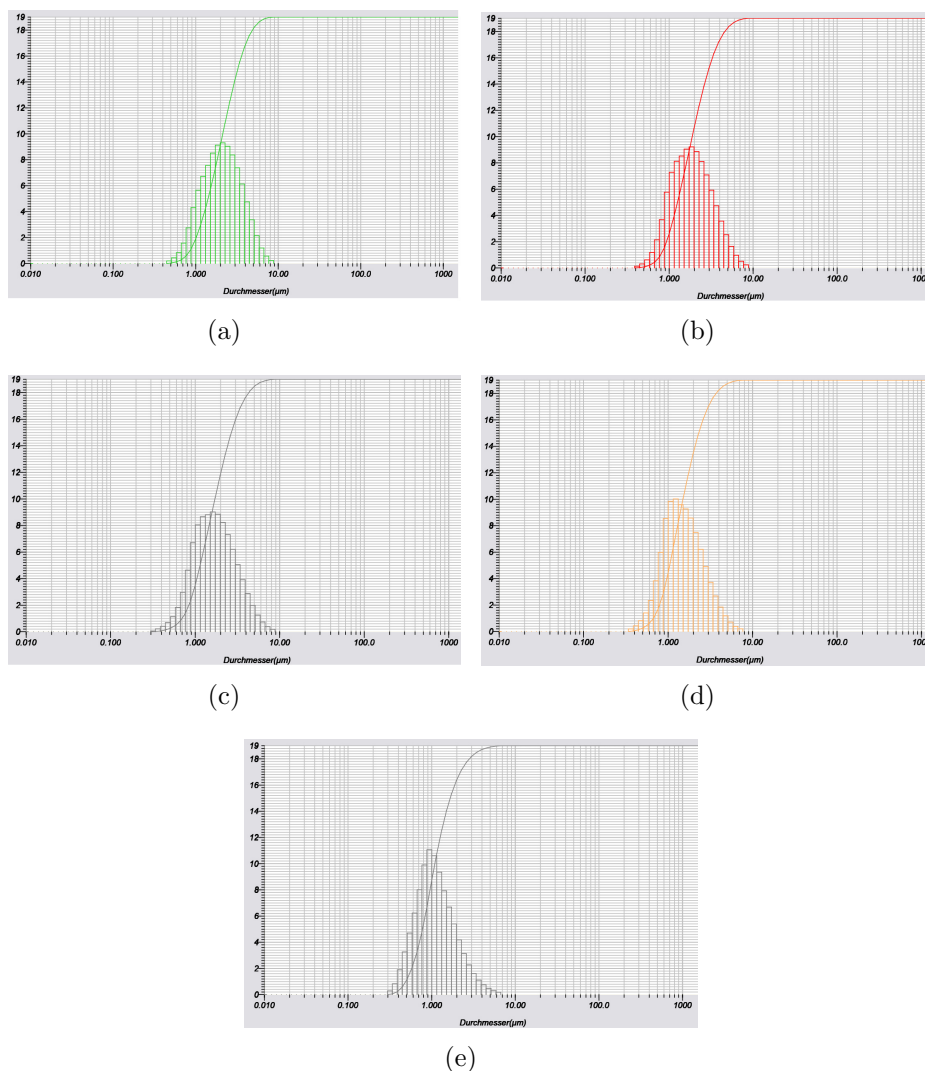
Figure 7.1: **Milling of primary particles:** Primary particle sizes, measured with laser scattering. Intensity in arbitrary units is displayed on the y-axis and particle size in logarithmic scale on the x-axis. Size distributions were measured after 4h (a), 6h (b), 8h (c), 12h (d) and 24h (e) of milling NMFO with a planetary mill (step IV of the synthesis).

The images of particle size distributions in this subsection were all created with the software of the mentioned device *LA-950 Laser Particle Size Analyzer* (Horiba, Retsch Technology).

7.1.2 Secondary particle size

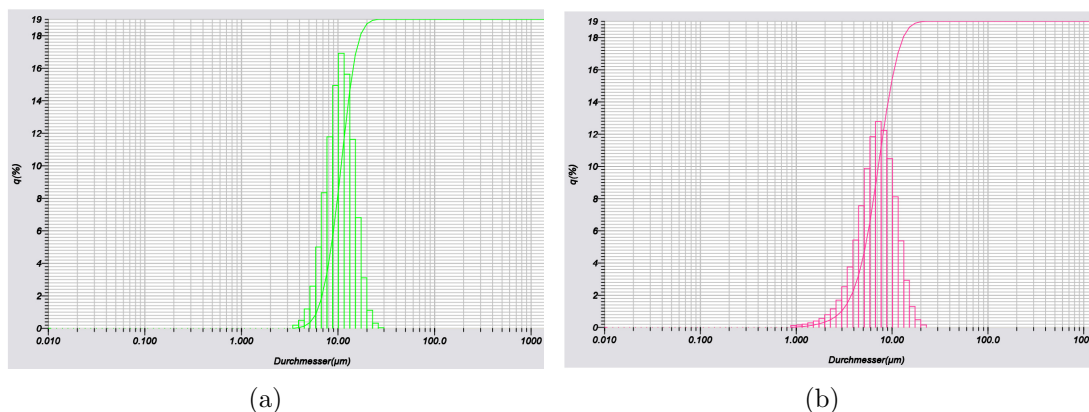|	
(a)	(b)
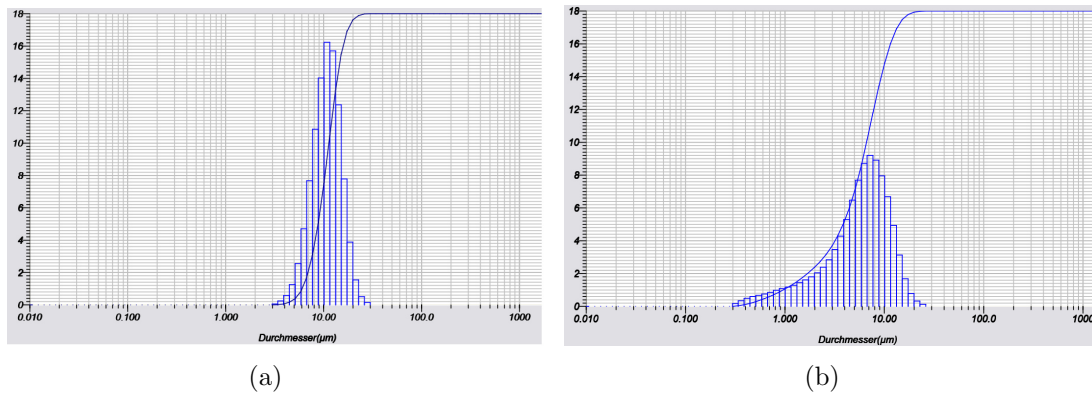
Figure 7.2: **NANMO secondary particle size distribution:** Laser scattering of NANMO after the final synthesis step VI, with $T_s = 950\,°C$. The powder was sieved with $32\,\mu m$ mesh size. The size distributions were measured with laser scattering. Intensity in arbitrary units is displayed on the y-axis and particle size in logarithmic scale on the x-axis. (a) shows the distribution of the powder after sieving. For (b) the sample was treated with ultrasound and the measurement was repeated. With the ultrasound was agglomeration removed and/or the secondary particles were broken. Corresponding data is found in Table 7.1
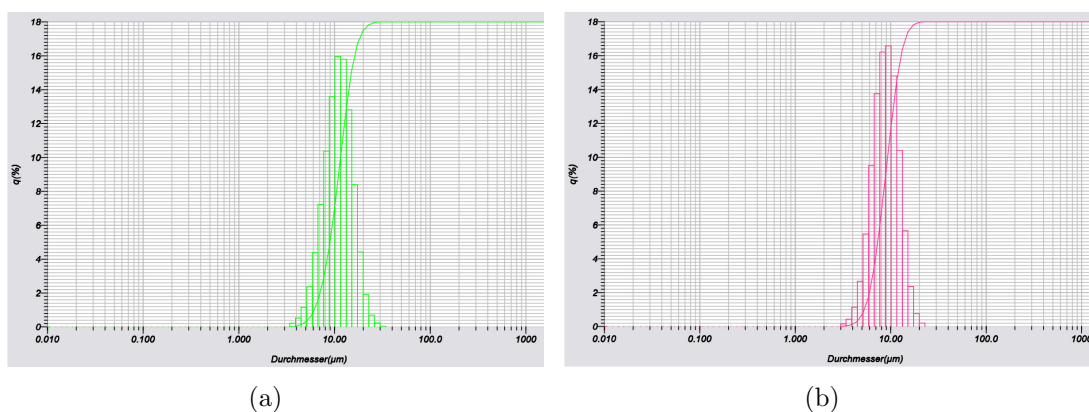
(a)   (b)

Figure 7.3: **NANMFO secondary particle size distribution:** Laser scattering of NAN-
MFO after the final synthesis step VI, with $T_s = 950\,°C$. The powder was
sieved with $32\,\mu m$ mesh size. The size distributions were measured with laser
scattering. Intensity in arbitrary units is displayed on the y-axis and par-
ticle size in logarithmic scale on the x-axis. (a) shows the distribution of
the powder after sieving. For (b) the sample was treated with ultrasound
and the measurement was repeated. With the ultrasound was agglomeration
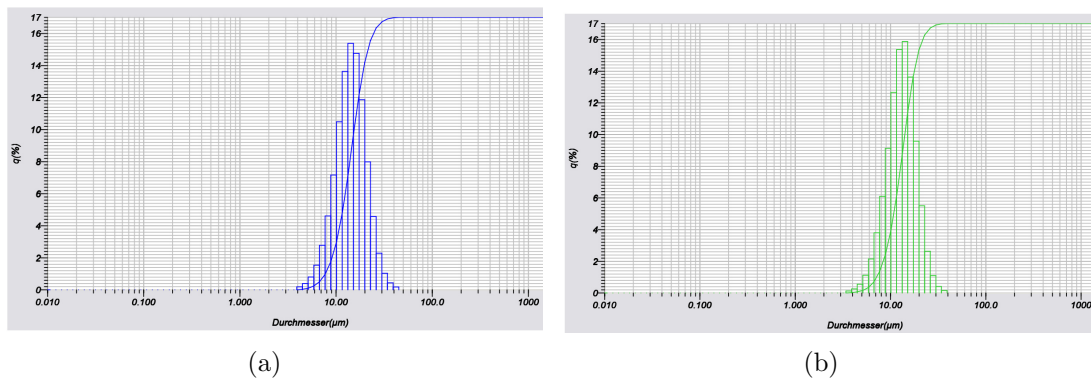removed and/or the secondary particles were broken. Corresponding data is
found in Table 7.2

(a)   (b)

Figure 7.4: **NAFMO secondary particle size distribution:** Laser scattering of NAFMO
after the final synthesis step VI, with $T_s = 950\,°C$. The powder was sieved
with $32\,\mu m$ mesh size. The size distributions were measured with laser scat-
tering. Intensity in arbitrary units is displayed on the y-axis and particle size
in logarithmic scale on the x-axis. (a) shows the distribution of the powder
after sieving. For (b) the sample was treated with ultrasound and the mea-
surement was repeated. With the ultrasound was agglomeration removed
and/or the secondary particles were broken. Corresponding data is found in
Table 7.3

(a)   (b)

Figure 7.5: **NMFO secondary particle size distribution:** Laser scattering of NMFO after
the final synthesis step VI, with $T_s = 950\,°C$. The powder was sieved with
$32\,\mu m$ mesh size. The size distributions were measured with laser scattering.
Intensity in arbitrary units is displayed on the y-axis and particle size in
logarithmic scale on the x-axis. (a) shows the distribution of the powder after
sieving. For (b) the sample was treated with ultrasound and the measurement
was repeated. With the ultrasound was agglomeration removed and/or the
secondary particles were broken. Corresponding data is found in Table 7.4

Table 7.1: **Particle size distribution of NANMO:** Corresponding data of Fig. 7.2.

NANMO			
Without ultrasound		With ultrasound	
Diameter in µm	Intensity q(%) (a.u.)	Diameter in µm	Intensity q(%) (a.u.)
3.4	0.07	0.8	0.12
3.9	0.28	0.9	0.17
4.5	0.67	1.0	0.21
5.1	1.52	1.2	0.26
5.9	3.12	1.3	0.32
6.7	5.70	1.5	0.40
7.7	9.06	1.7	0.52
8.8	12.28	2.0	0.66
10.1	15.03	2.3	0.86
11.6	16.37	2.6	1.15
13.2	14.72	3.0	1.57
15.2	10.68	3.4	2.18
17.4	6.18	3.9	3.06
19.9	2.86	4.5	4.27
22.8	1.07	5.1	5.85
26.1	0.34	5.9	7.72
29.9	0.03	6.7	9.61
		7.7	11.06
		8.8	11.57
		10.1	11.17
		11.6	9.89
		13.2	7.68
		15.2	5.02
		17.4	2.74
		19.9	1.26
		22.8	0.50
		26.1	0.18

Table 7.2: **Particle size distribution of NANMFO:** Corresponding data of Fig. 7.3.

NANMFO			
Without ultrasound		With ultrasound	
Diameter in µm	Intensity q(%)	Diameter in µm	Intensity q(%)
3.9	0.19	1.0	0.11
4.5	0.49	1.2	0.15
5.1	1.19	1.3	0.20
5.9	2.59	1.5	0.28
6.7	5.00	1.7	0.39
7.7	8.34	2.0	0.55
8.8	11.77	2.3	0.78
10.1	14.93	2.6	1.14
11.6	16.91	3.0	1.69
13.2	15.63	3.4	2.52
15.2	11.62	3.9	3.74
17.4	6.80	4.5	5.43
19.9	3.10	5.1	7.55
22.8	1.11	5.9	9.86
26.1	0.31	6.7	11.84
29.9	0.03	7.7	12.78
		8.8	12.23
		10.1	10.47
		11.6	8.10
		13.2	5.37
		15.2	2.92
		17.4	1.29
		19.9	0.47
		22.8	0.15

Table 7.3: **Particle size distribution of NAFMO:** Corresponding data of Fig. 7.4.

| **NAFMO** | | | |
| Without ultrasound | | With ultrasound | |
Diameter in µm	Intensity q(%)	Diameter in µm	Intensity q(%)
3.9	0.22	3.4	0.15
4.5	0.51	3.9	0.43
5.1	1.15	4.5	1.13
5.9	2.36	5.1	2.66
6.7	4.39	5.9	5.46
7.7	7.23	6.7	9.51
8.8	10.37	7.7	13.74
10.1	13.58	8.8	16.21
11.6	15.95	10.1	16.57
13.2	15.79	11.6	14.80
15.2	12.81	13.2	10.39
17.4	8.39	15.2	5.65
19.9	4.42	17.4	2.35
22.8	1.90	19.9	0.76
26.1	0.69	22.8	0.19
29.9	0.23		
34.3	0.03		

Table 7.4: **Particle size distribution of NMFO:** Corresponding data of Fig. 7.5.

NMFO			
Without ultrasound		With ultrasound	
Diameter in μm	Intensity q(%)	Diameter in μm	Intensity q(%)
4.5	0.19	3.9	0.12
5.1	0.39	4.5	0.26
5.9	0.79	5.1	0.55
6.7	1.53	5.9	1.11
7.7	2.77	6.7	2.14
8.8	4.61	7.7	3.80
10.1	7.16	8.8	6.09
11.6	10.48	10.1	9.12
13.2	13.62	11.6	12.65
15.2	15.38	13.2	15.36
17.4	14.75	15.2	15.86
19.9	11.86	17.4	13.62
22.8	7.98	19.9	9.57
26.1	4.57	22.8	5.50
29.9	2.29	26.1	2.63
34.3	1.03	29.9	1.09
39.2	0.43	34.3	0.41
44.9	0.17	39.2	0.14

7.2 Rietveld refinement

7.2.1 Ex situ XRD for $T_s = 950\,°\text{C}$

In the following are the XRD patterns of the four layered oxides presented. The diffractograms were measured after $T_s = 950\,°\text{C}$. The green *hkl*-ticks indicate the Bragg positions of the reflections. The refinement of the structure parameters was carried out with different software. In Figure 7.6 the software Fullprof was used and the *hkl*-ticks in the upper row indicate the P2-phase, the lower row indicates an impurity phase of NaMO_2 (M = Ni, Mn) with the space group *R-3mH*, which was considered in the refinement procedure. The observed (red) and calculated (black) XRD patterns show good overlapping.

Figures 7.7, 7.8, 7.9 and 7.10 shows the results of the refinement with the software jEdit and Topas. In this case the impurity phase was not refined and will not be considered any further.
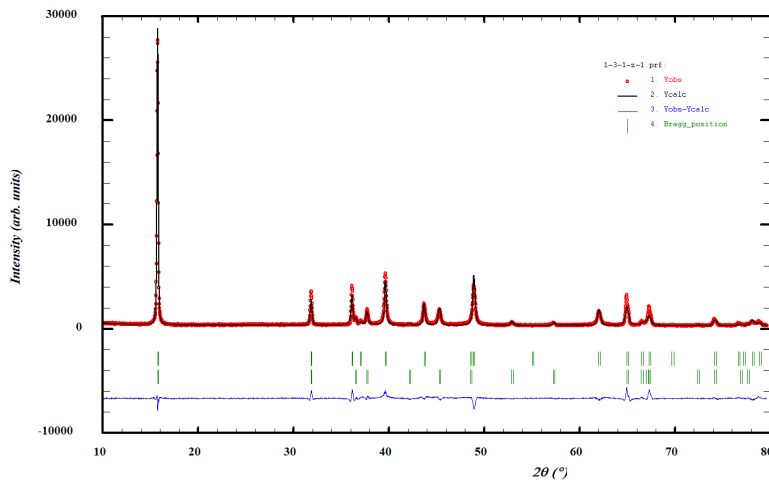
Figure 7.6: **Refinement of the NANMO structure with Fullprof:** XRD pattern of P2-type NANMO, measured after $T_s = 950\,°\text{C}$. Refined parameters were calculated with the software Fullprof.
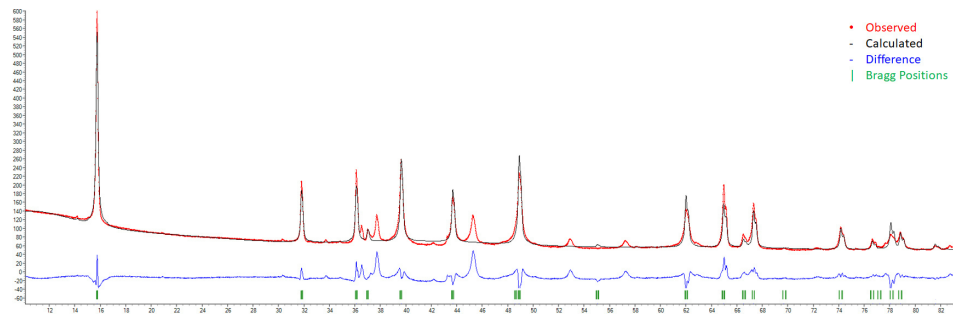
Figure 7.7: **Refinement of the NANMO structure parameters with Topas:**   Impurity
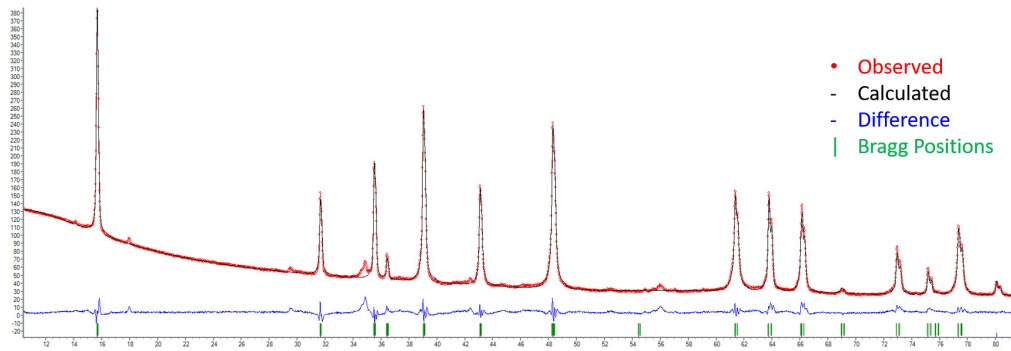reflections are visible at approx. 38° and 45°
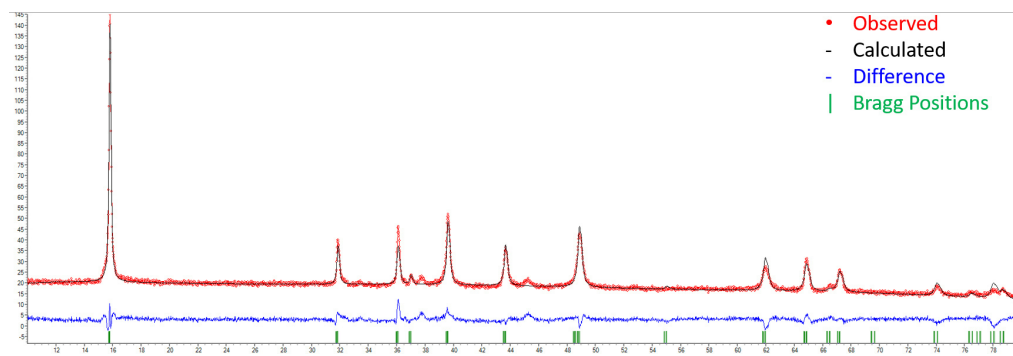
Figure 7.8: **Refinement of the NANMFO structure parameters:** XRD pattern of P2-
type NANMFO measured after $T_s = 950\,°C$. The green *hkl*-ticks indicate
the P2-phase. Created with the software jEdit Topas. The impurity phase
visible in case of NANMO (see Fig. 7.7) has almost vanished.
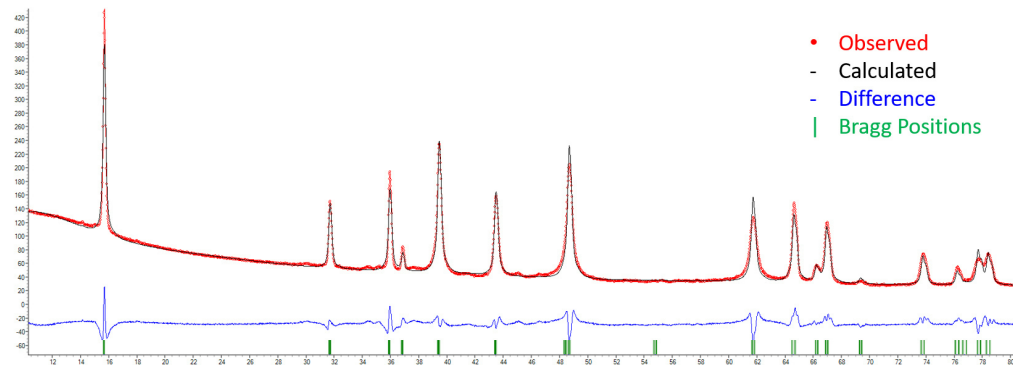
Figure 7.9: **Refinement of the NAFMO structure parameters:**   XRD pattern of P2-
type NAFMO, measured after $T_s = 950\,°C$. The green *hkl*-ticks indicate the
P2-phase. Created with the software jEdit and Topas. No impurity phase
was visible.

Figure 7.10: **Refinement of the NMFO structure parameters:**   XRD pattern of P2-type NMFO, measured after $T_s = 950\,°C$. The green *hkl*-ticks indicate the P2-phase. Created with the software jEdit and Topas. The small impurity phase was not part of the refinement calculation.

7.2.2 Ex situ XRD: Temperature series

XRD patterns of the four P2-type materials after $T_s = 850\,°C$, $T_s = 900\,°C$ and $T_s = 1000\,°C$ are presented in the figures 7.11, 7.12, 7.13 and 7.14. The *hkl*-ticks indicate the P2-phase. The structure parameters were refined and resulted in the calculated XRD pattern. The impurity phase was not considered. Created with the software jEdit and Topas.
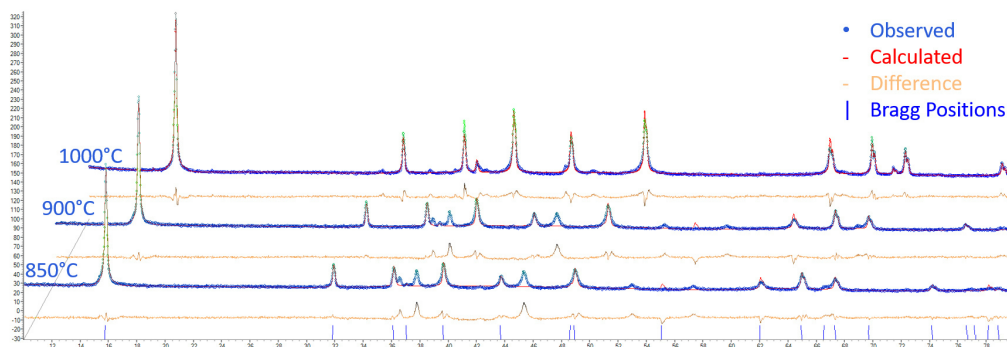
Figure 7.11: **Temperature series of NANMO**
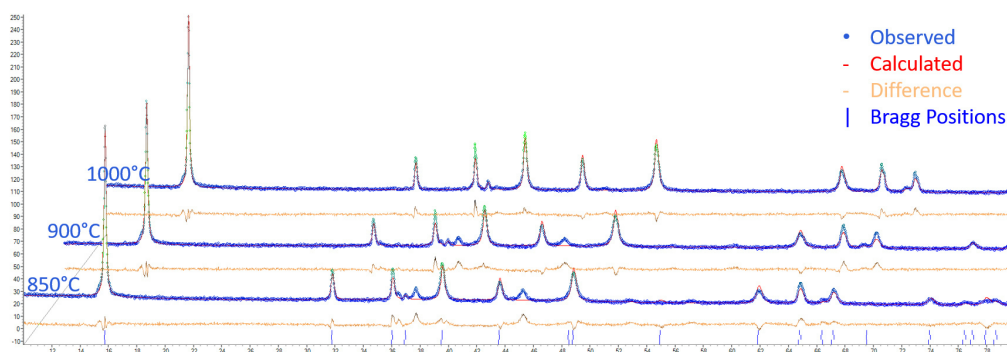
Figure 7.12: **Temperature series NANMFO**
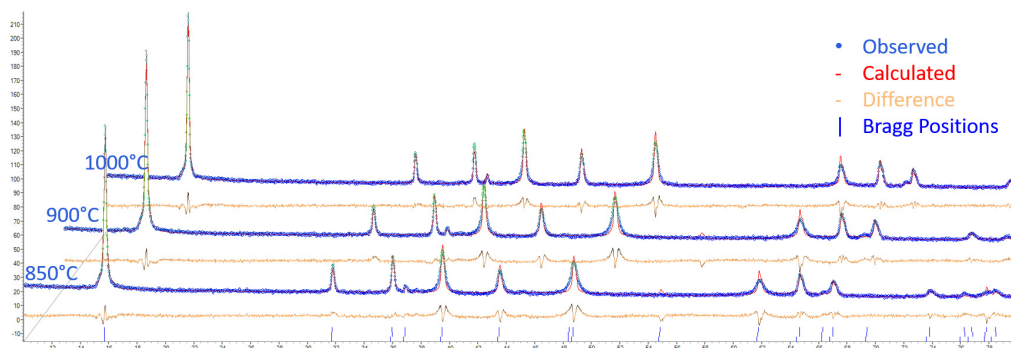
Figure 7.13: **Temperature series NAFMO**
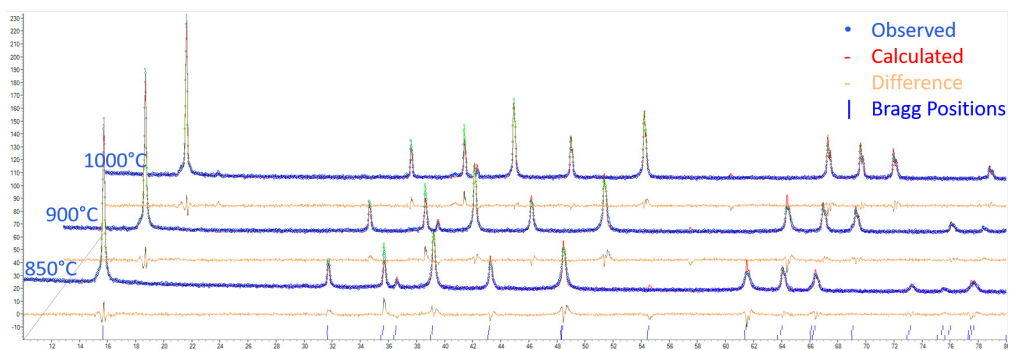
Figure 7.14: **Temperature series NMFO**

115

7.2.3 In situ XRD

The following figures 7.15, 7.16, 7.17 and 7.18 show XRD patterns and the calculated patterns from the rietveld refinement.
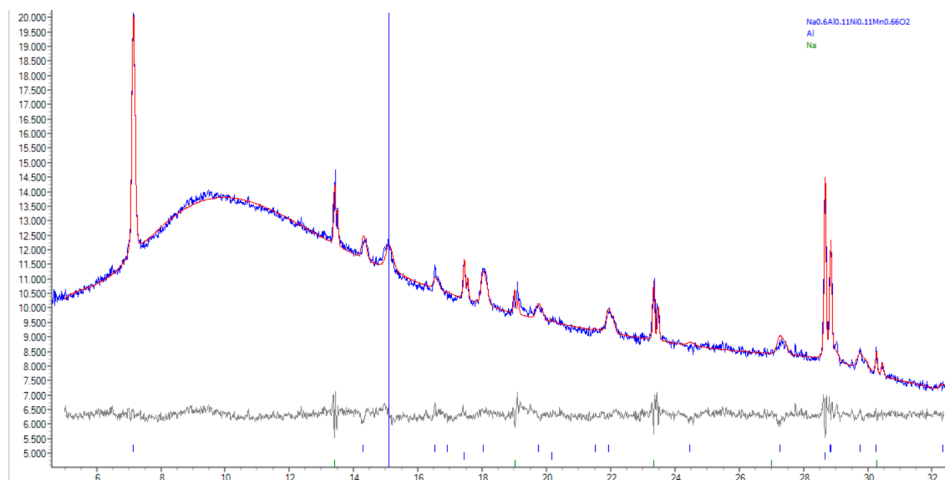
Figure 7.15: **Observed and calculated XRD pattern at OCV:** XRD pattern of a half cell with NANMO at the beginning with the OCV = 2.75 V. The *hkl*-ticks refer from top to bottom to: P2-structure, aluminium (current collector) and sodium (anode). The vertical line represents a reflection from the XRD device. Created with the software jEdit and Topas.
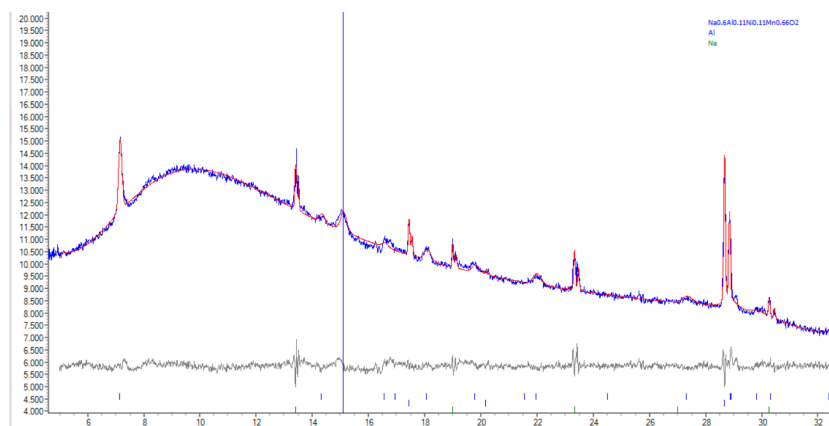
Figure 7.16: **Observed and calculated XRD pattern during charging:** XRD pattern of a half cell with NANMO with U = 4.4 V. The *hkl*-ticks refer from top to bottom to: P2-structure, aluminium (current collector) and sodium (anode). The intensity of the P2-phase has significantly decreased. Created with the software jEdit and Topas.
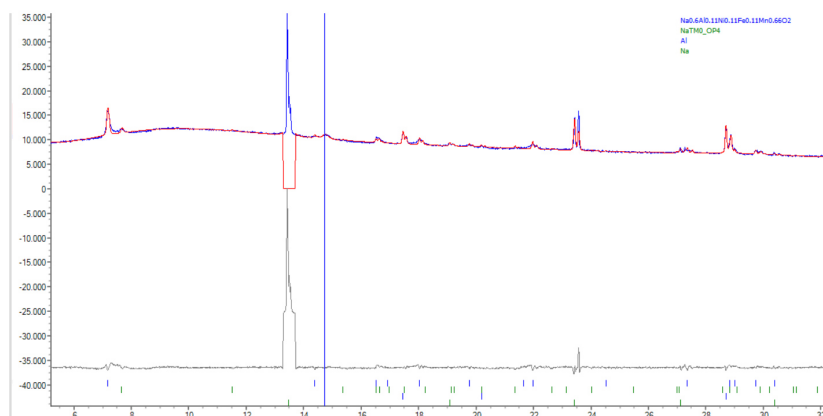
Figure 7.17: **Observed and calculated XRD pattern of fully charged cell:** XRD pattern of a half cell with NANMO with U = 4.6 V. The *hkl*-ticks refer from top to bottom to: P2-structure, OP4-structure, aluminium (current collector) and sodium (anode). The intensity of the P2-phase has significantly decreased and a weak intensity of the OP4-phase has become visible. Created with the software jEdit and Topas.
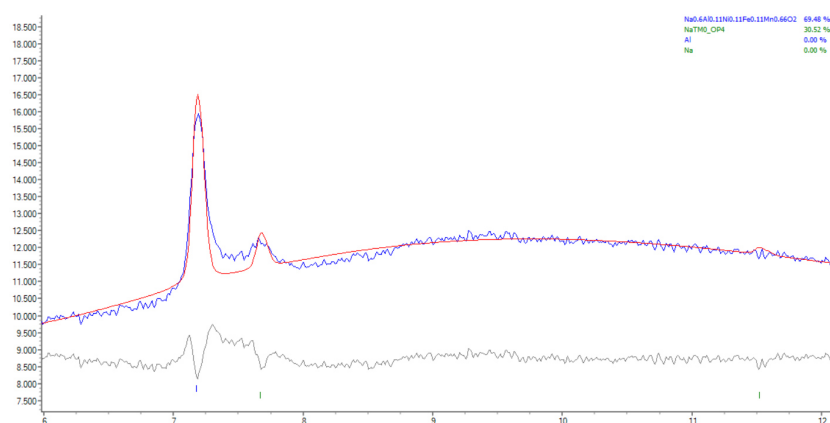

Figure 7.18: **Close-up of the 002 reflection at full charge:** XRD pattern of a half cell with NANMO with U = 4.6 V. The *hkl*-ticks refer from top to bottom to: P2-structure, OP4-structure, aluminium (current collector) and sodium (anode). The intensity of the P2-phase has significantly decreased and a weak intensity of the OP4-phase has become visible (zoomed in). Created with the software jEdit and Topas.

7.3 Degree of grinding for NANMO

In order to receive smaller primary particles different grinding processes were tested in the early phase of the work. Three degrees of grinding (coarse, medium and fine) were tested for NANMO. This was achieved with different diameters of ZrO_2 grinding spheres (see Tab. 7.5). For the a degree of coarse and medium the planetary ball mill
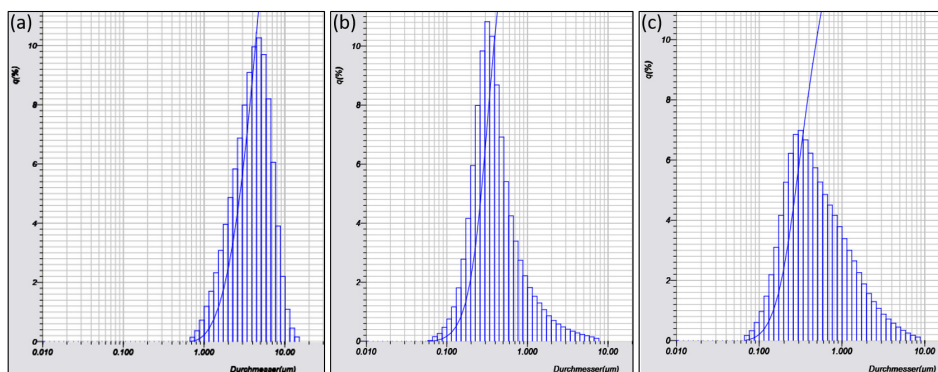
Figure 7.19: **Milling with the agitator bead mill:** Size distribution of NANMO primary particles after (a) 15 min, (b) 30 min and (c) after 60 min of milling with the agitator bead mill. Measured mean sizes were 15 μm, 0.3 μm and 0.4 μm, respectively.

Degree of grinding	Grinding media diameter in mm	2nd spray drying		Sintering at 950 °C	
		Φ in %	A_{BET} in m^2/g	Φ in %	A_{BET} in m^2/g
Coarse (planetary)	3	55	14,96	47	3,89
Medium (planetary)	1.75	59	13,68	50	4,3
Fine (agitator)	0.2	39	23	26	3,6

Table 7.5: **Different degrees of grinding:** For each grinding process the secondary particle morphology after second spray drying and second heat treatment was investigated (see Chap. 4 *Experimental*). Porosity Φ and specific surface area (A_{BET}) of the secondary particles is changing due to different milling of primary particles.

Pulverisette 5 (Fritsch) was used. For the planetary ball mill were the same grinding parameters used as described in Chapter 4. Grinding time was always 24 h until the no significant change in the primary particles size was observed (see Fig. 7.1).

To receive degree which is described here as "fine" an agitator bead mill *LabStar LS1* (Netzsch) was utilized. In that case 200 μm ZrO_2 beads were used at 3000 rpm and the milling was performed for 60 min. The evolution of primary particle sizes during the milling can be seen in Figure 7.19.

After already 30 min (b) the mean particle size reached its minimum and additional 30 min lead not to smaller particles but rather some agglomeration, suggesting for future experiments that 30 min milling time is sufficient.

Table 7.5 shows an overview of the porosity Φ and the specific surface area A_{BET} of

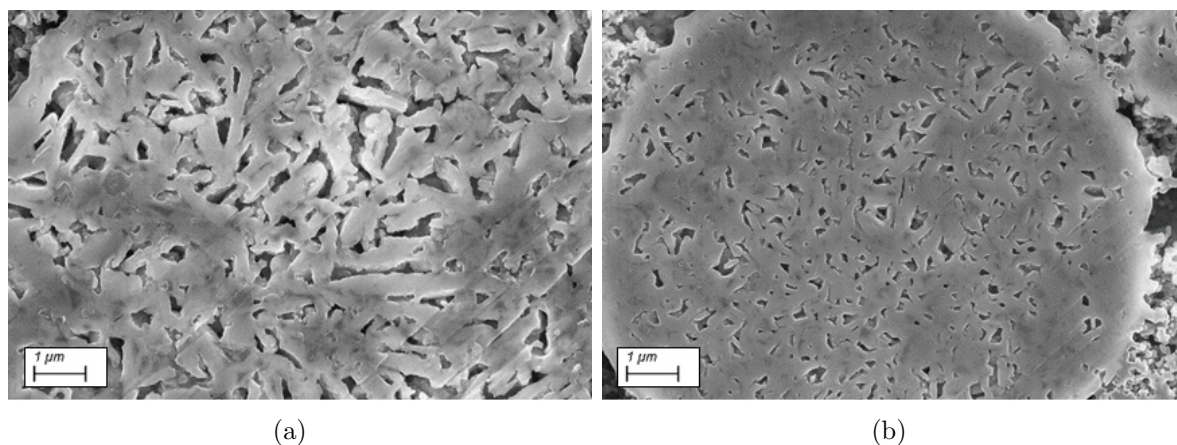(a)   (b)

Figure 7.20: **Different cross-sections:** SEM images of cathode cross-sections reveal the porosity of the secondary particles when different grinding methods were used. Presented is a cross-section with (a) coarse ground and (b) fine ground primary particles.

the sprayed and sintered secondary particles when different grinding methods were applied. Both parameters decrease during sintering, as described before. However it is noteworthy that with "fine" grinding the porosity after spray drying is already rather low and decreases then even further with the sinter process. In case of fine grinding A_{BET} after spraying is higher as compared to the other two powders but gets reduced to a similar value after sintering. The significant difference seems to be the porosity, which has an important influence on the electrochemical performance as cathode material. These differences in porosity are supported by SEM images of cross-sections of cathode sheets made from these materials. Figure 7.20 (a) shows the cross-section of a secondary particle which was prepared with coarse milling. The primary particles have a flake-like appearance. In case of fine milling (b) the primary particles are so small heavily sintered to each other that it is difficult to distinguish them. In Chapter 7.4.1 the electrochemical performance of the different grinding degrees will be presented.
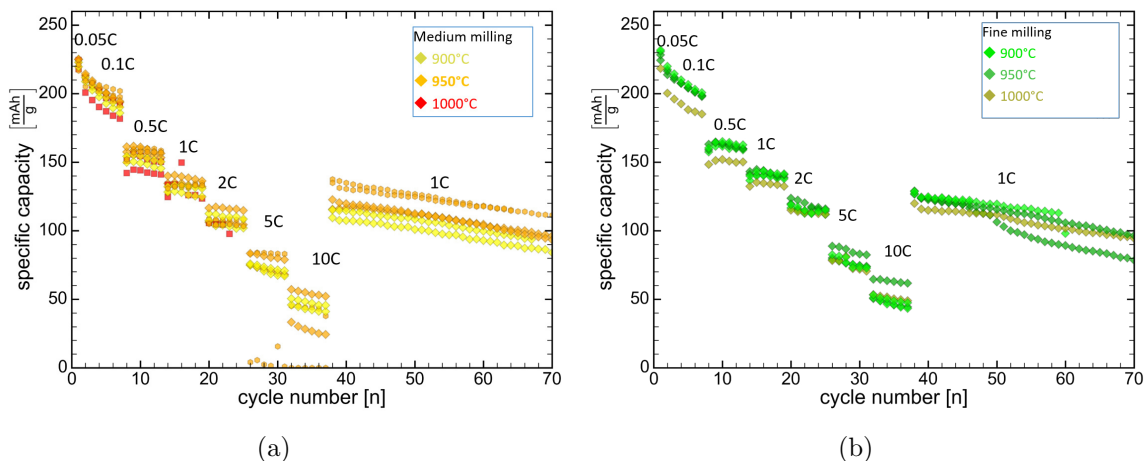
Figure 7.21: **C-rate test for powders with different degree of grinding:** Cycling of
NANMO with (a) medium and (b) fine grinding process after different sin-
tering temperatures. Please note that the colour code for NANMO, NAN-
MFO, NAFMO and NMFO, which was used everywhere else in this work
could not be used consequently in this case: All data in this Figure was
obtained from NANMO materials.

7.4 Electrochemistry

7.4.1 Degree of grinding

Figure 7.21 shows the cycling data of medium (a) and fine (b) grinding. Also different
sintering temperatures were tested. In figure 7.22 (a) the cycling of coarse ground
material after the same temperatures is shown. (b) shows an overlay of data from the
three different grinding processes, sintered all at 950 °C. The coarse ground material lead
to higher specific capacity and better rate capability in comparison to the other grinding
processes. The stability however was found to be better with medium or fine grinding for
this sintering temperature. On the other hand an improvement of stability could also be
achieved for with the coarse ground NANMO with different sintering temperatures (see
Fig. 7.22 (a)). For that reason it was decided to use the coarse milling for the research
presented in all the other chapters of this work and to test it also for NANMFO, NAFMO
and NMFO.

7.4.2 Precycling with 1C

Figure 7.23 shows materials sintered with $T_S = 1000$ °C and cycled in the voltage window
1.5 V to 4.6 V. Different C-rates result in different performances. For all materials in
the first charging cycle (1C) the reached capacity is well below the theoretical value but
roughly in close range. Using a smaller current for the first charge did result in an even
higher value, closer to the theoretical capacity (not displayed here). The first charge
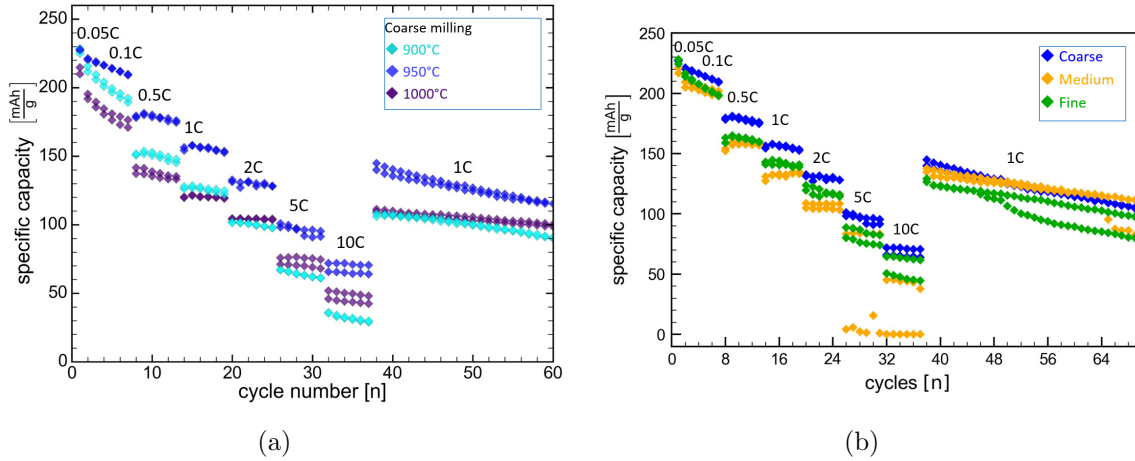
(a)   (b)

Figure 7.22: **Comparison of different ground NANMO:** (a) Shows NANMO after coarse grinding and different sintering temperatures. (b) Shows how the different grinding processes affect the cycling when the sintering temperature is 950 °C.

capacity (1C) is clearly exceeded by the first discharge (1C), then by the second charge (C/20) and once more exceeded by the second discharge (C/20).

During the first discharge a small bump is visible in the profiles, indicating that during the first cycle not just the active material is involved but perhaps side reactions occur when passivation layers form on the electrodes interface. For all materials in the first charging cycle (1C) the reached capacity is well below the theoretical value but roughly in close range. Using a smaller current for the first charge did result in an even higher value, closer to the theoretical capacity (not displayed here). The first charge capacity (1C) is clearly exceeded by the first discharge (1C), then by the second charge (C/20) and once more exceeded by the second discharge (C/20).

The interpretation is similar to the one presented in Chapter 5.4.1. During the first charge cycle with 1C the sodium amount available is $z = 0.6$ given from the chemical formula of the pristine materials. During the first discharge, additional sodium from the anode is inserted into the cathode, due to the lower cut off voltage $1.5\,\text{V} < \text{OCV}$. This results in higher capacity above the theoretical value. However, this first cycle was performed with 1C, a more moderate than small current, so the sodium ion kinetics could not completely keep up in the short amount of time. In other words not all sodium ions could be removed from the cathode in this short time. In the next cycle with C/20 there is much more time for the slow kinetic reactions to take part to a more complete extent. This is the reason why the second charge and discharge deliver more capacity. Also, during the discharge with C/20 additional sodium can be inserted into the cathode, this time more due to the lower C-rate, but the difference between charge and discharge capacity has already shrunken, since additional sodium has already been inserted in the first discharge. The following cycles with C/10 can be understood analogue to the description from Chapter 5.4.1.
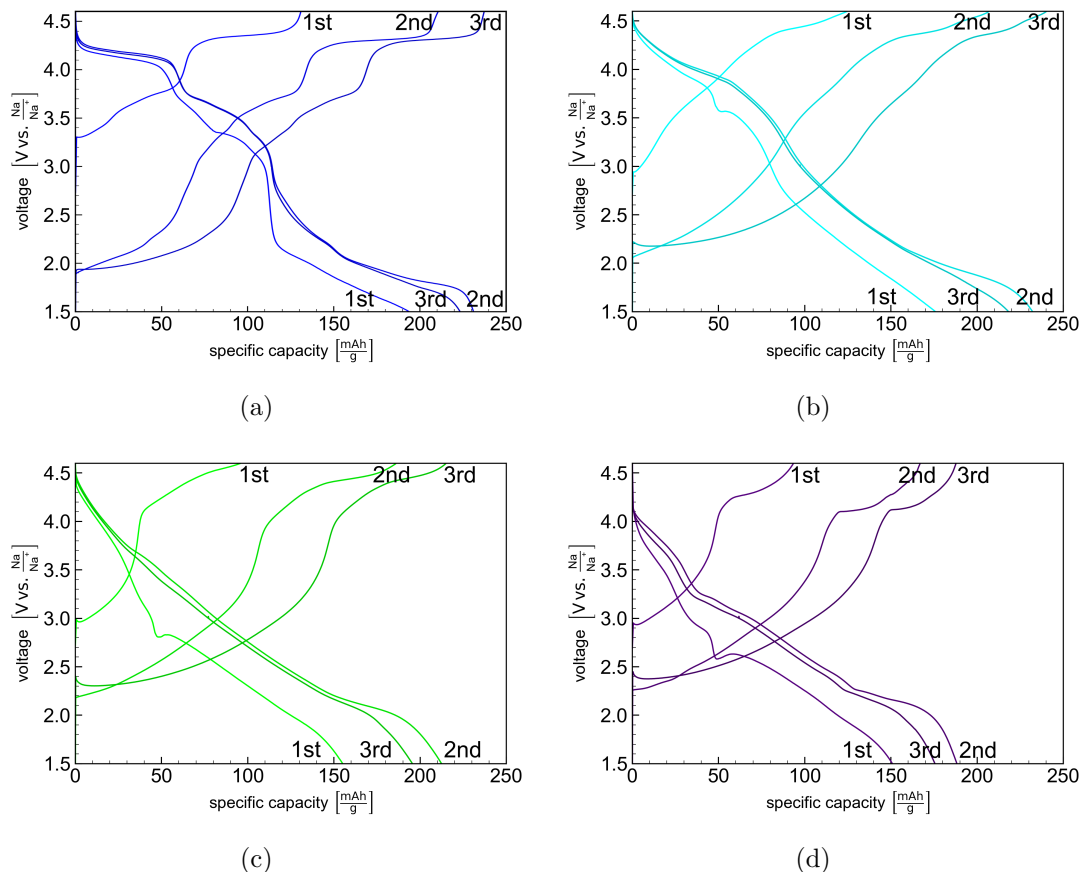
(a)

(b)

(c)

(d)

Figure 7.23: **Charge-Discharge-Curves:** The first three cycles of NANMO (blue), NAN-MFO (cyan), NAFMO (green) and NMFO (purple). Different C-rates were used as follows: 1C, C/20 and C/10.

The approach of precycling with 1C was chosen at some point of the presented work as pragmatic solution to increase the success rate of cells, when charging to 4.6 V and was then kept mandatory for all cells. A long-term cycling showed no disadvantageous behaviour in half-cells when precycled with 1C.

7.4.3 Variations of long-term tests of NANMFO

In order to receive some improved long-term stability the electrochemical window was changed even further. Lowering the upper and lower potential limit both increases the stability. This was tested for NANMFO. Figure 7.24 shows four different windows for NANMFO after sintering with 950 °C. After ca. 100 cycles the specific capacities, which were quite different in the beginning seem to have reached a similar level. Therefore the advantage of additional capacity in the larger electrochemical windows becomes obsolete in the long-term cycling.
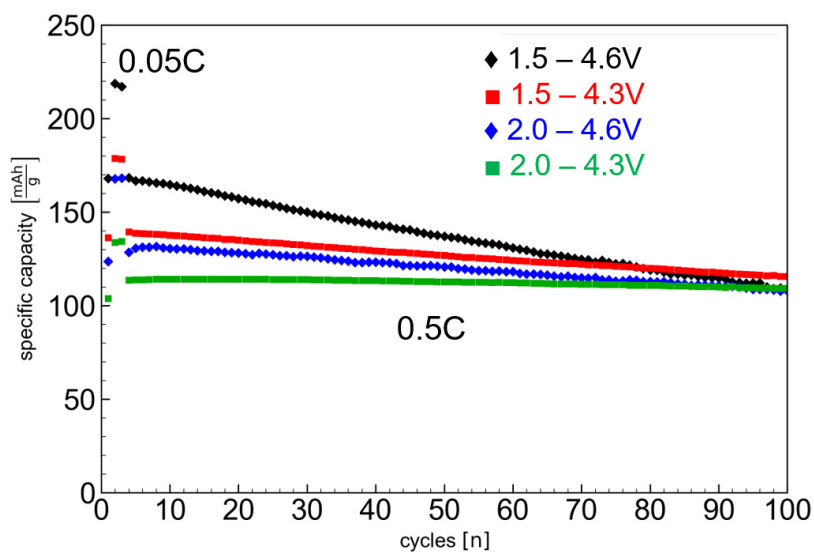
122

Figure 7.24: **Variation of long-term cycling of NANMFO:** NANMFO after sintering with 950 °C. In the larger windows more specific capacity is obtained. This is however accompanied by stronger degradation and therefore capacity loss.